A33
11/14/77

Ah. 1577

LA-6763

UC-11

Issued: September 1977

MASTER

Rainout Assessment: The ACRA System and Summaries of Simulation Results

Clayton W. Watson
Sumner Barr
Ray E. Allenson

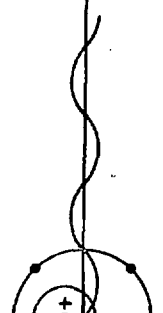

los alamos
scientific laboratory
of the University of California
LOS ALAMOS, NEW MEXICO 87545

An Affirmative Action/Equal Opportunity Employer

UNITED STATES
ENERGY RESEARCH AND DEVELOPMENT ADMINISTRATION
CONTRACT W-7405-ENG. 36

DISTRIBUTION

Printed in the United States of America. Available from
National Technical Information Service
U.S. Department of Commerce
5285 Port Royal Road
Springfield, VA 22161
Price: Printed Copy ~~$5.50~~ $6.50 Microfiche $3.00

This report was prepared as an account of work sponsored by the United States Government. Neither the United States nor the United States Energy Research and Development Administration, nor any of their employees, nor any of their contractors, subcontractors, or their employees, makes any warranty, express or implied, or assumes any legal liability or responsibility for the accuracy, completeness, or usefulness of any information, apparatus, product, or process disclosed, or represents that its use would not infringe privately owned rights.

CONTENTS

NOTICE

This report was prepared as an account of work sponsored by the United States Government. Neither the United States nor the United States Department of Energy, nor any of their employees, nor any of their contractors, subcontractors, or their employees, makes any warranty, express or implied, or assumes any legal liability or responsibility for the accuracy, completeness or usefulness of any information, apparatus, product or process disclosed, or represents that its use would not infringe privately owned rights.

(I,J) = National Meteorological Center octagonal-grid coordinate system.

(x,y) = rectilinear coordinate system for SPOOR, SCAWUEN, RAIN, SHASTA, and SHASTAX (km).

(X,Y) = rectilinear coordinate system for TEMPEST (km).

z = altitude (km).

j = time-step index.

$\omega_j = (I_j, J_j, Z_j, t_j)$ = phase-space point in SPOOR at time step j.

$\beta_{j,i}$ = velocity recursion-relationship correlation parameter between time steps j and i.

r = distance (km).

Y = total fission-equivalent yield of a SPOOR source cloud (kt).

t_j = time at step j measured from the SPOOR particle's birth (h).

Δt = time-mesh width (h).

T = total simulation time in a SPOOR calculation; or observation time; or maximum threat-time (h).

N = total number of time steps in a SPOOR-particle trajectory; or total population with $1WBD \geq D$; or overall radial-binning parameter for the effects-tallying grid in SCAWUEN.

M = total number of source particles in a SPOOR calculation.

$\overline{v}$ = average debris-cloud centroid velocity (km/h).

$(\overline{u},\overline{v})$ = orthogonal wind components in the NCAR wind data base (km/h).

RAF = rain area fraction.

$\overline{RAF}$ = average rain area fraction.

σ_m^2, m = precipitation-cell area distribution parameters for TEMPEST.

A_m = maximum precipitation-cell area (km^2).

a = semimajor axis of a precipitation cell (km).

b = semiminor axis of a precipitation cell (km).

a_{max} = maximum value of a during cell's lifetime (km).

T_{max} = total lifetime of a cell (h).

β = precipitation-cell aspect ratio = b/a.

(X_c, Y_c) = location of a precipitation-cell center in TEMPEST.

$\vec{V} = (V_X, V_Y)$ = precipitation-cell velocity in TEMPEST (km/h).

ϕ = angle between Y-axis and $\vec{V}$.

θ = angle between cell minor axis and $\vec{V}$.

$\psi = \phi + \theta$.

$\vec{\Omega}_j = (x_j, y_j, z_j, t_j)$ = phase-space point in SCAWUEN.

(x_c, y_c) = location of a precipitation-cell center in SCAWUEN.

(x_s, y_s, z_s) = location of a SPOOR particle within a cell in SCAWUEN.

R_o = maximum rain intensity at the center of a precipitation cell (mm/h).

$\gamma, \gamma_X, \gamma_Y$ = within-cell intensity distribution parameters.

$\sigma_a = \gamma_X a$.

$\sigma_b = \gamma_Y b$.

$\alpha(Z)$ = vertical-intensity distribution.

R = local precipitation rate (mm/h).

λ = scavenging coefficient (h^{-1}).

W_t = total debris-particle weight scavenged during time Δt from a given SPOOR particle at $\vec{\Omega}_j$.

w_s = unscavenged weight of a SPOOR particle at $\vec{\Omega}_j$.

$\vec{v}_z \equiv \vec{v}(Z)$ = horizontal transport velocity at altitude Z for a scavenged debris particle (km/h).

t_f = time for a scavenged particle to reach the ground (h).

ΔW_{jm} = ground-deposited weight during time step j from SPOOR particle m.

(x_{jm}, y_{jm}) = ground location of ΔW_{jm}.

(x_{jc}, y_{jc}) = location of the centroid of ground-deposited particles during time step j.

r_{jm} = radial distance from the centroid of ground-deposited particle m at time step j (km).

$\bar{r}_j$ = first moment about the centroid of the radial distribution of ground-deposited particles at time step j (km).

$\sigma^2_{r_j}$ = second moment about the centroid of the radial distribution of ground-deposited particles at time step j (km^2).

K = number of angular divisions for the effects-tallying grid in SCAWUEN; or the amplitude of the scavenging-coefficient function.

F = outer radial-binning parameter for the effects-tallying grid in SCAWUEN.

r_n = radius of the n^{th} annular ring in the effects-tallying grid in SCAWUEN (km).

r_N = largest of the r_{jm} (km).

A_{jk} = area of tally-bin k at time step j (km^2).

I_{jk} = deposited-debris intensity for a tally-bin within which point k is located at time step j (particles/km^2).

IWBD = free-field infinite whole-body dose (rem).

d_t = dose rate at time t after detonation from deposited debris (rem/h).

t_d = time after detonation that deposition occurs (h).

d_{jk} = IWBD at point k from deposition during time step j (rem).

D_k = total IWBD at point k for all time steps (rem).

R_T = average precipitation rate for observation time T (mm/h).

P_1 = probability that $\overline{RAF} \geq RAF_o$, given that $\overline{RAF} \neq 0$.

P_2 = probability that observable precipitation occurs during observation time T.

P_T = probability that $\overline{RAF} \neq 0$ during observation time T and that $\overline{RAF} \geq RAF_o$.

P = occurrence probability.

N_{max} = maximum population with IWBD $\geq D_c$.

r_{max} = maximum threat-distance (km).

RAINOUT ASSESSMENT: THE ACRA SYSTEM AND SUMMARIES OF SIMULATION RESULTS

by

Clayton W. Watson, Sumner Barr, and Ray E. Allenson

ABSTRACT

We developed a generalized, three-dimensional, integrated computer code system to estimate collateral-damage threats from precipitation-scavenging ("rainout") of airborne debris-clouds from defensive tactical nuclear engagements. This code system, called ACRA for Atmospheric-Contaminant Rainout Assessment, is based on Monte Carlo statistical simulation methods that allow realistic, unbiased simulations of probabilistic storm, wind, and precipitation fields that determine actual magnitudes and probabilities of rainout threats. Detailed models (or data bases) are included for synoptic-scale storm and wind fields; debris transport and dispersal (with the roles of complex flow fields, time-dependent diffusion, and multidimensional shear effects accounted for automatically); microscopic debris-precipitation interactions and scavenging probabilities; air-to-ground debris transport; local demographic features, for assessing actual threats to populations; and nonlinear effects accumulations from multishot scenarios. We simulated several hundred representative shots for West European scenarios and climates to study single-shot and multishot sensitivities of rainout effects to variations in pertinent physical variables. One interesting result was the consistent behavior of rainout effects versus scavenging efficiency λ, rain rate R, and shot yield Y: effects dropped off rapidly at $\lambda \lesssim 0.1\ h^{-1}$, $R \lesssim 0.1$ mm/h, or $Y \lesssim 0.1$-0.4 kt. More important, we demonstrated broad, shallow, maximum-threat regimes for $\lambda \gtrsim 0.5\ h^{-1}$, $0.1 \lesssim R \lesssim 1$ mm/h, and $0.4 \lesssim Y \lesssim 5$ kt. Other inherent features of rainout determined for a spectrum of scenarios were maximum threat-times and distances, occurrence probabilities in the West German climate, and comparisons between rainout effects and fallout or prompt collateral-damage effects.

I. INTRODUCTION

Defensive tactical nuclear engagements in adverse weather involve the possibility that precipitation scavenging ("rainout"*) of airborne nuclear weapon debris could deposit highly radioactive material on the ground. If such deposition occurs before dispersal in the atmosphere can dilute the debris cloud, this "wet fallout" could pose a delayed collateral-damage threat to downwind populations.

Depending on their likelihood and magnitude, these threats may have important implications for future US nuclear-weapon design and employment doctrine. Rainout effects, for example, could be of particular significance when weapons of <10-kt fission yield are used in an airburst mode. In this mode, a device is detonated at an altitude that precludes direct interaction of the fireball with the ground surface, and little or no surface material mixes with the weapon debris. In this case, the radioactive debris is attached to aerosol-like particles so small that they remain aloft, and conventional, gravity-driven, "dry" fallout is essentially eliminated. Thus, for a weapon that is airburst to maximize useful military effects and eliminate dry fallout, rainout becomes the only remaining source of delayed collateral damage. The question is then whether, or under what circumstances, rainout effects might negate the collateral-damage advantage of airbursts and how the problem, if it exists, can be minimized.

The Los Alamos Scientific Laboratory (LASL) has an ongoing study program to assess rainout effects and implications. We have developed a generalized, three-dimensional, integrated, computer code system for this purpose and have used this system to estimate rainout effects for several hundred representative nuclear shots in West European scenarios and climates. In this report, we describe our rainout assessment system and its underlying physical bases, and present numerical results. Our calculations have given us considerable insight into the character and magnitude of rainout threats.

II. BACKGROUND

Rainout has posed a persistent and controversial problem in the US

---

*In this report, we will use the term "rainout" both in a generic sense to imply any and all precipitation-scavenging events and in the more conventional way to specifically denote in-cloud scavenging events. The work reported here deals primarily with this latter phenomenon, which is generally recognized as the dominant source of potential collateral-damage threats.[1,2]

nuclear-weapon community for several years. Historically, some confusion seems to have developed as to what the relative roles and importance of the many physical elements involved are and what we should calculate, and why.

We believe that uncertainties as to what the roles of the driving elements are can be traced to overall modeling approaches that have been too narrow in outlook and to the resulting, often subtle, rigidities built into the assessment codes. It is reasonable, for example, to make conservative estimates for the elements of a problem and then combine them into upper-limit estimates of effects, provided the measures of conservatism are adequately understood and the results are truly bounding; then, if the results are within acceptable limits, the problem goes away. On the other hand, if such estimates show that a potential problem still exists (as with rainout), the assessment procedures and tools must be upgraded until uncertainties diminish enough for decision makers to understand and use the model results with confidence.

Rainout assessment is an especially insidious task. Fundamental complexities in the atmospheric transport of debris clouds, in the driving meteorological phenomena, and in the precipitation processes themselves make the analytical problems difficult, involving space and time scales that span many orders of magnitude. Moreover, rainout threat levels and damage probabilities are determined by intricate interactions and tradeoffs among several physical, logistic, and demographic factors; the problem is thus intractable in broad terms. Intuition is also often misleading, and generalized conclusions usually are too easily begged somewhere in the analytical process.

We recognized in mid-1973 that rainout assessment had reached an impasse because of the above difficulties and because we lacked a sufficiently general and flexible modeling framework for systematically examining the physical elements of the problem to place them in proper perspective. A totally new approach was needed that emphasized pragmatic goals while still recognizing and effectively modeling the relevant physical phenomena. The approach also had to be directed explicitly to acquiring sensitivity information needed to estimate actual rainout effects for realistic scenarios, and it had to establish confidence bounds within which these estimates could be used.

A major goal of our work has been to develop such an approach and the analytical tools to implement it. The basis of our scheme is an overall

modeling framework designed to be general and flexible enough to accommodate continual upgrading of model components to facilitate a progression through a hierarchy of increasingly sophisticated analyses, as required, to achieve acceptable accuracy in the results. This approach depends on continual information feedback between model development and technical analysis (Fig. 1) to identify and evaluate relevant factors, avoid irrelevant or secondary issues, and avoid the "intuition" and "generalization" pitfalls mentioned earlier.

III. PROBABILISTIC NATURE OF RAINOUT

Rainout is inherently stochastic--a direct result of the capricious nature of local wind, storm, and precipitation patterns. The most important stochastic variables relate to the time and space structure of precipitation cells and to turbulent air motions that determine diffusion and meander of debris clouds and entrainment of debris into precipitating systems. This character of rainout means that rainout collateral-damage effects are fundamentally unpredictable except in probabilistic terms. Upper-limit estimates thus do not provide adequate insight into rainout threats. Because rainout damage is a relatively unlikely event, we are interested in unlikely combinations of the relevant individual physical events. Practical cases of interest lie in the "tails" of the governing probability density functions (PDFs), and this fact, plus the fact that the analytical problems are complex, forces us so far out on the PDF tails in attempts to be "conservative" that the resultant overall rainout situations are hardly credible. In other words, to impose extreme or bounding conditions on these probabilistic variables without begging the question becomes impossible, particularly since it is often difficult even to know what constitutes a conservative assumption.

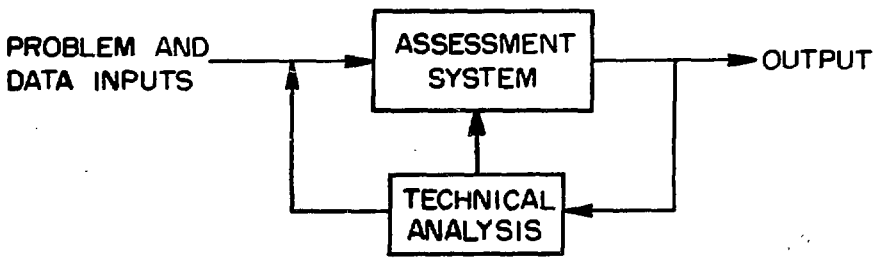

Fig. 1.
Dynamic information feedback.

Unfortunately, "average" or "typical" estimates of rainout effects are not very informative either, because rainout is itself atypical.* Real rainout-threat situations are never average, nor are any resulting rainout effects, and the less likely events are of greater interest. For example, the consequences of a low-probability rainout event that happens to occur over a large city can be more significant than a high-probability event where no significant population centers lie downwind from the shot. In a given instance, furthermore, the total hazard represented by the combined probabilities of several unlikely events may pose a problem even though each individual threat is innocuous.

The key point here is that not only must we estimate hazards and consequences for representative specific cases, but, more important, we must also estimate the associated probabilities. In this process, it is also essential that we be mathematically correct in combining the probabilities of the pertinent individual elements so that we obtain meaningful overall rainout assessments. For these reasons, we have based our analytical approach on Monte Carlo statistical simulation techniques that allow us to combine the physical elements of the problem relatively easily in a statistically unbiased, multidimensional fashion; because individual elements are combined probabilistically, essential stochastic variabilities are accounted for naturally.

The logical core of our simulation system is a three-dimensional, Monte Carlo, debris-transport model; other elements are modeled in a similar fashion based on integral inputs in the form of PDFs extracted from the literature and from available data bases. Collateral-damage estimates for specific battlefield scenarios depend on the collocation of debris, storm systems, precipitation, and populations and are available through straightforward, linear, statistical tallies.

IV. REQUIREMENTS FOR A RAINOUT COLLATERAL-DAMAGE EVENT

The stochastic features of rainout mean that several events must occur at the same time and place before significant rainout collateral-damage effects can result. These events, along with the principal physical factors that determine their distributions in time and space, are listed below.

---

*The most frequently occurring rainout-threat level is zero.

- Debris must be concentrated enough to pose a threat. Generally, for the low-yield devices pertinent to rainout, this condition is met only for a few hours and within several tens of kilometers downwind from the shot. Driving factors: scenario (particularly yields and number of shots), local winds, and atmospheric diffusion rates.

- A precipitating storm system must be in the area. Even in the relatively wet climate of Western Europe, most days throughout a year are free of large-scale storm systems that can offer substantial rainout possibilities in a given area. Driving factors: local climate and storm-system synoptic characteristics.

- Precipitation cells must exist in the area and must be intercepted by the debris. Even in very "rainy" parts of a storm, the precipitation patterns are cellular in structure; and a specific debris cloud will encounter important precipitation cells relatively infrequently. This point requires special attention because previous work in rainout has essentially overlooked the variability of precipitation on scales comparable to the dimensions of the debris clouds and to the separation distances between population centers. This precipitation variability is important in determining actual rainout effects. Driving factors: mesoscale precipitation morphology, debris and precipitation-cell interaction dynamics, and local winds.

- Ground-deposition rates must be substantial. Both the precipitation rate and the scavenging probability per unit precipitation rate must exceed certain levels to produce ground doses above a damage threshold. Considerable controversy exists regarding scavenging mechanisms and probabilities pertinent to airburst debris. Indeed, there is disagreement as to whether real scavenging rates permit rainout collateral damage to occur at all. Even if the most "dangerous" scavenging mechanisms dominate, however, that in itself does not necessarily imply large rainout casualties. Driving factors: scavenging mechanisms, debris particle sizes, debris physical-chemical characteristics, and precipitation-intensity distributions.

- Debris deposition must be over people. We disagree on this point with other rainout investigators who use rainout "area" as a measure of rainout effects. The concept of area as a measure of collateral damage from delayed radiation sources transported through the atmosphere is useful only in certain special contexts. For example, it can be useful for conventional fallout

because the "deposition" function (gravity) is constant and we can, at least in principle, predict where a given dose-rate contour will lie. It is then reasonable to introduce separately a "damage" function (distribution of people) to estimate effects. No such direct relationship is possible for rainout, however, because both the deposition function (precipitation cells) and damage function (people) are distributed discretely and heterogeneously.

One must therefore distinguish clearly and carefully among concepts such as (1) people at risk (because the debris cloud passes overhead and could deposit material), (2) "average" number of people under "average" rainout deposition contours, and (3) expected-value probabilities for numbers of people exposed to different hazard levels in representative military and meteorological situations. The first two items can be compared with prompt- and dry-fallout collateral-damage areas, but they are not measures of expected rainout damage for a specific situation as is the third item;* nor are they related in a useful way to actual rainout effects (except, of course, for the special case where the rainout-threatened area is so small that quantitative estimates of actual casualty expectations are unnecessary). Driving factor: local demography.

The combined probabilities for coincidence in time and space of the above five events (debris, storm system, precipitation, scavenging, and population) determine rainout hazards. This combination is a complex mathematical problem that cannot be handled by intuition or by multiplying averages together. However, when the probability of any one of these events is small for a given scenario or if a combination of any subset of these probabilities is small, the corresponding overall probability of rainout hazard is small. This point is important in gaining perspective on the seriousness of the rainout problem for specific contexts.

V. PHYSICAL ELEMENTS THAT DETERMINE RAINOUT EFFECTS

In this section, we identify the principal physical elements that determine rainout hazards and probabilities, doing so more or less chronologically in terms of the debris-cloud history from formation through transport, scavenging, and deposition processes to assessment of on-the-ground effects.

---

*In contrast to gravity-driven fallout, for example, the usual rainout hazard is zero.

A. Scenario. Included here are those parameters that define the configuration of the debris clouds at stabilization time (generally a few minutes after shot time). These parameters establish the initial conditions or "source" for the rest of the problem.

The most important factors are number of shots, shot yields, number of fissions, and shot locations with respect to each other and to downwind populations. Yield directly affects the dimensions of the debris cloud, the intensity of radioactivity that may later be rained out, and the vertical location of the stabilized debris in the atmosphere. Debris altitude is important because the pertinent wind fields and precipitation probabilities vary with altitude. (Because precipitation systems are limited to altitudes below ~10 km, our rainout interest is restricted to devices with yields less than a few tens of kilotons.) Number of shots, shot locations, and total fissions determine total dose levels and the number of people threatened at various dose levels.

B. Debris Transport and Dispersal. Debris transport and dispersal establish where individual debris clouds will go, how they will grow, and how multiple clouds will separate or converge. These are key factors in rainout-effects assessment. Debris dispersal (incoherent transport) limits the lifetime of rainout threats to one to a few hours for a given shot, depending on the yield and the damage threshold considered, and determines the width of the threatened area on the ground. Debris transport (coherent transport) determines how far the cloud will travel during its threat lifetime and, hence, the downwind length of the threat area.

(We emphasize again, however, that the size of this threat area and the number of people within it are not measures of collateral damage; they only establish bounds. People within this contour are people at risk, i.e., they are potential candidates for a rainout event because of the cloud's passing overhead, not casualties. Rainout effects can occur only where precipitation cells (1) intercept the debris cloud and (2) deposit the debris over people. The number of people at risk will usually be large, whereas the number of actual casualties will usually be zero and will never be more than a small fraction of the people at risk because of the heterogeneous distributions of precipitation and population and because depletion of the cloud by a rainout event in one part of the threat area reduces the threat elsewhere.)

The roles of debris transport and dispersal are subtle, and one often cannot know in advance what condition is or is not conservative because complex tradeoffs determine rainout effects. For example, higher wind speeds drive the debris cloud over more people, but the hazard to each is less because of the reduced cloud residence time overhead. Lower wind speeds, on the other hand, imply that the cloud will threaten fewer people but will present a greater hazard to those people threatened before it is dispersed. Some certain wind speed will pose a maximum danger, but what that speed is depends on other driving factors (yield, dispersal rate, and population distribution) and can be determined for a specific scenario only by sensitivity and tradeoff studies. Similar comments apply to dispersal rates: the more rapidly a cloud grows, the more area it will cover, but the more rapidly it will be diluted, and vice versa. Dispersal rate itself also depends on the prevailing wind field because of shear effects.

The meteorological factors that determine debris dispersal and transport are, respectively, small- to mesoscale atmospheric turbulence and meso- to large-scale wind fields, the latter representing a modeling area where appropriate climatic data can and should be introduced.

C. Time and Space Distributions of Debris-Precipitation Interactions. These topics include most of the meteorological aspects of the rainout problem. We can further separate the physical elements most important to rainout into two interrelated but distinctively different groups: (1) factors that determine the frequency, location, and extent of interception regimes between debris clouds and relevant precipitation cells, and (2) influences of local circulation features in the vicinity of debris-cell encounters (for example, entrainment or detrainment). Group 1 dominates because it directly determines the likelihood, location, and overall coverage of rainout events. Group 2 affects the intensity of a rainout event and, to a lesser degree than group 1, the extent and location of ground deposition.

Coincidence probabilities and intersection regimes for debris and scavenging-cell encounters depend on the mesoscale time and space structure of precipitation cells. This structure depends in turn on position within a synoptic-scale disturbance (Appendix A) and ultimately, therefore, on regional climate. Knowledge of the time-space trace of a debris cloud and of the stochastic extent and behavior of precipitation cells (from precipitation-

morphology data and modeling studies) allows statistical assessment of the pertinent intersections. (The situation is not generally one where a small debris cloud is embedded in continuous or constant precipitation, but rather one where a chance encounter occurs between two widely varying but comparable volumes in space. The complete superposition and mixing of these volumes is an improbable special case, so we must consider the extent of such intersections as well as their associated probabilities.)

Given an intersection between debris and a precipitating system, it is generally also necessary to evaluate other aspects of the encounter. Air movements within and near the precipitation system will alter the local distribution of affected debris and should be accounted for in establishing the extent and intensity of resulting ground deposition. Changes in the precipitation system caused by the presence of the debris particulates, however, are not expected to be important.

D. Scavenging Rates. Many microscopic physical processes exist by which precipitation scavenging could remove debris particles from air, and their relative magnitudes and roles are still poorly understood; nor are the pertinent properties of debris particles well established. These uncertainties translate directly into fundamental uncertainties in removal rates for the practical problem.

Experimental work relies heavily on ground observations through broad hypotheses concerning how various removal mechanisms combine and how they vary with altitude, and how scavenging data for one particle species can be extrapolated to other, grossly different species. Unequivocal data are unlikely because airburst tests with nuclear devices are by treaty impossible.

The existing literature indicates that the gap between theory and experiment also has not been bridged. The large variety of possible scavenging mechanisms and their dependence on medium- and small-scale variations in moisture, particle size, particle physical-chemical characteristics, temperature, airflow, and storm-cloud life cycle probably mean that theory is many years away from providing a definitive substitute for real airburst data. Indeed, theory is probably several years away from synthesizing the separate mechanisms into a form we can directly compare with present field observations.

Detailed studies by other rainout investigators[3] imply that debris scavenging will occur with efficiencies that are in the range of maximum

rainout danger, with an uncertainty factor of ~10 in absolute scavenging efficiency. The rainout problem therefore cannot be dismissed solely on the basis of arguments that scavenging rates are too low for airburst debris to pose a problem, at least until a more complete and convincing synthesis of the whole scavenging-rate problem becomes available.

We can bound rainout effects, however, through sensitivity studies made with our assessment system; and our results show that collateral-damage effects are relatively insensitive to overall scavenging efficiency over the "dangerous" range. The whole problem can then be put in proper perspective with respect to the other driving elements.

E. Population Distribution. The importance of local population density and distribution was pointed out earlier. We need a detailed, realistic, population data base to estimate rainout collateral-damage effects rather than threat areas.

F. Postdeposition Factors. Even if we know the amount and distribution of debris deposited at the earth's surface, we still do not have a direct measure of real doses that resident populations would receive. We should account for several other phenomena, most of which would be protective in character.

For example, runoff and washoff from hard surfaces would transport debris-laden precipitation to storm sewers and rivers, thereby reducing casualties in just those areas with the most concentrated populations, the cities. Similar comments apply to shielding by structures. Ground absorption would be effective in reducing dose rates in other areas, as would shielding by local terrain features.

Another broad area of importance is protective response by threatened people. For example, the potentially longer delay times inherent with rainout, as compared with those for prompt effects or dry fallout, mean that significant time (perhaps many hours) would often be available for protective measures before large doses were accumulated.*

Proper assessment of relevant postdeposition factors is a major task that is beyond the scope of our present rainout study. We can make such assessments later, however, because they are essentially independent of the other elements in our system; and, because the overall effect would be to reduce rainout collateral-damage estimates, we have thus far viewed the whole area of

*This time factor is another reason why rainout effects are comparable with prompt effects and dry-fallout effects only on a qualified basis.

postdeposition effects as a built-in conservatism ("safety" factor) in our results and have used the same conventional, unshielded measure that other investigators use in determining effects, the "infinite whole-body dose" (IWBD) (Appendix B).

VI. THE ACRA SYSTEM

The analytical tools we have developed to address rainout problems are embodied in a computer system we call ACRA, for "Atmospheric-Contaminant Rainout Assessment." The basic criteria for ACRA are as follows.

Modeling Objectives:

- Emphasize pragmatic goals and solutions.
- Develop a broad, flexible, overall modeling and computational framework.
- Accommodate requirements for in-depth treatment of many difficult, interacting, physical elements.
- Eliminate as many irrelevant elements as possible by scoping their influences to make the problem tractable.

Ground Rules:

- Carefully define collateral-damage measures.
- Make conservative, practical, state-of-the-art evaluations of driving elements.
- Rely on detailed work of others where possible.
- Use adequate and appropriate data bases (recognizing especially that time and space resolution of data must match the scales of pertinent physical events).
- Emphasize actual effects assessments and the implications of realistic operational contexts.

Operational Approach:

- Use scoping and bounding calculations to identify potential collateral-damage situations.
- Make finer-cut sensitivity studies to discriminate and evaluate systematically the roles of individual driving elements.
- Use information feedback to upgrade model components systematically as necessary to improve the quality of assessment results.
- Iterate until the "problem" goes away or the results become definitive.

The ACRA system (Fig. 2) consists of eight computer codes, each composed of easily replaced modules. These eight codes are independent but communicate with each other (Sec. VII) to give an integrated overall system. The eight codes and their functions are as follows.

GEBESO: Prepares input-data libraries for SPOOR.

SPOOR: Debris transport and dispersal simulator.

RESPOOR: Reprocesses SPOOR output for input to SCAWUEN.

TEMPEST: Storm and precipitation-cell simulator.

SCAWUEN: Scavenging simulator.

SHASTA: Tallies rainout effects from a single shot.*

SHASTAX: Tallies rainout effects from multiple shots.

RAIN: Tallies rain amounts at fixed ground points.

---

*The codes GEBESO through SHASTA calculate a single input source configuration. Normally, we use a source representing the stabilized cloud from a single shot.

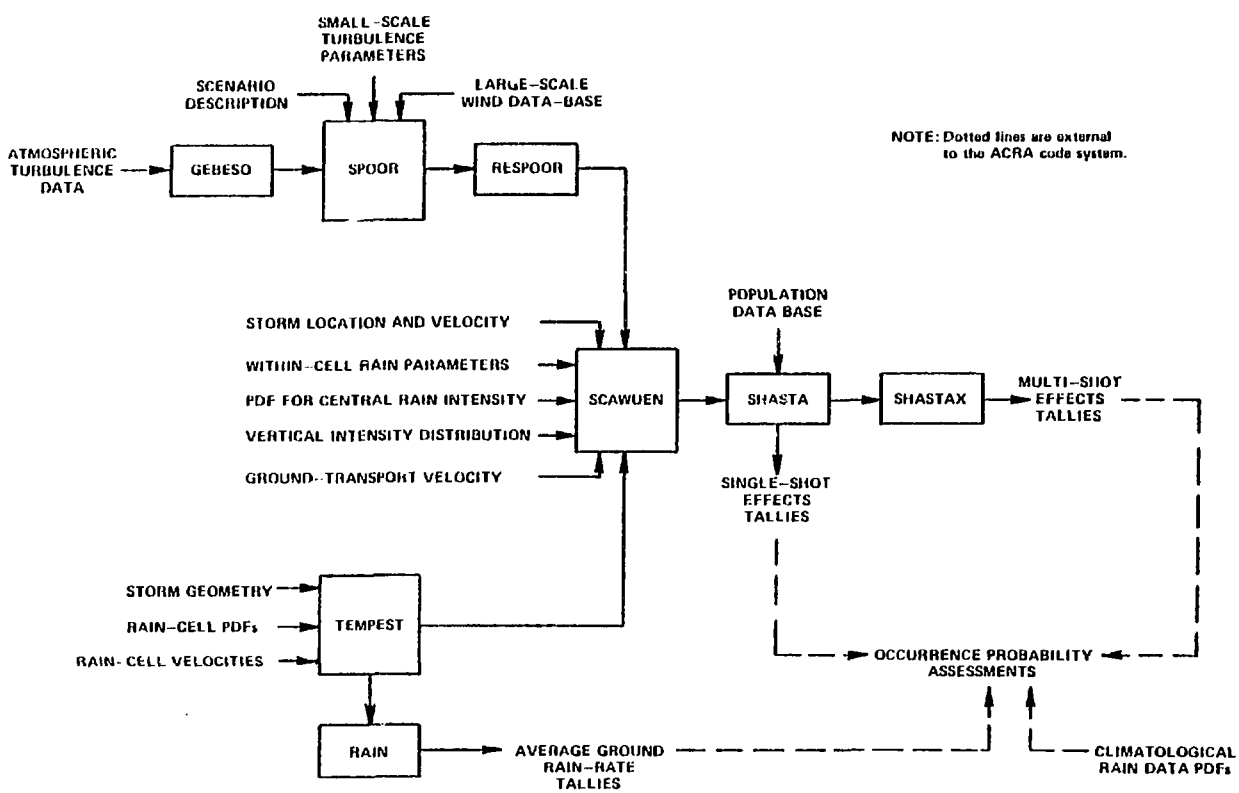

Fig. 2.
The ACRA system.

A. GEBESO. GEBESO uses input atmospheric-turbulence spectral data to prepare autocovariance functions and corresponding $\beta_{j,i}$ parameters for the debris-particle random-walk recursion relationships in SPOOR. These parameters have been described elsewhere.[4]

GEBESO extends the original SPOOR code to permit an arbitary number of up to 100 correlated velocity terms in the recursion relationships.* It also provides an automatic capability for building libraries of $\beta_{j,i}$ sets (for different input spectra and various numbers of correlation terms) that can be selected by SPOOR.

The input to GEBESO is an atmospheric turbulence-energy spectrum, and its output is a set of $\beta_{j,i}$ values for SPOOR.

B. SPOOR. This code is described in Ref. 4; only an outline will be given here. SPOOR represents an initial source cloud with a large number of individual particles. Each particle is "tracked" by simulating its wind-driven trajectory through a series of small time steps to produce a set of independent random-walk trajectories in three-dimensional time and space. This tracking is done by statistically sampling simulated local wind and turbulence fields as each particle advances in time. These fields are based on generalized wind data for large-scale flow and on turbulent-energy spectra for micro- and mesoscale flow. To include effects from a broad spectrum of turbulent-energy scales, input for the large-scale field is derived from a climatological data base for Western Europe (Appendix C), and micro- and mesoscale wind fluctuations are introduced through a power spectral density. We thus simulate the role of turbulence in both meander and dispersal, naturally account for complex flow fields and time-dependent diffusion rates, and automatically simulate three-dimensional shear effects in the ensemble of particle trajectories.

This model forms the core of the ACRA modeling approach. Not only is it inherently realistic, but, more important, it also makes tractable the mathematical problems of effecting the probability combinations (Secs. III and IV). The model generates independent random-walk trajectories for the

---

*Only three terms were allowed in the original SPOOR code.

simulated debris particles and implicit statistical properties of the ensemble of trajectories thus replace the explicit "cloud" properties of other formulations. Because each particle traces out a well-defined, pointwise, history in time and space it has a straightforward relationship to other variable fields defined in the same phase space, such as precipitation-cell morophology, precipitation intensity, scavenging probability, and population. There is no need to resort to convenient but artificial debris-geometry representations as a basis for estimating interactions. This is in contrast with the more conventional deterministic modeling frameworks, where simulation of stochastic interactions between a "cloud" and the other problem variables becomes difficult and somewhat arbitrary.

In simulating material transport in any domain that is subject to a series of interdependent random processes, the tracking, interaction, and tallying techniques must also account for the essential stochastic variabilities without biasing the result by intermediate integrations, such as defining a "cloud size" before accounting for precipitation intercepts. It is intrinsically realistic to generate a particle trajectory along which one or more of these processes can occur and then impose the proper phase-space-dependent process simulations and build up the "cloud" effects as an ensemble of these individual elements.

The input to SPOOR consists of a set of $\beta_{j,i}$ values from GEBESO, a set of small-scale wind-fluctuation variances, a large-scale wind data base, and the scenario data: yield, stabilized source-cloud dimensions, source-cloud altitude, initial debris distribution, shot time, and shot geographical location. Outputs from SPOOR consist of state variables (time, position, velocity) for all particle trajectories at all time steps, for input to RESPOOR, and a summary printout of the first and second moments of the state variables at each time step.

C. RESPOOR. RESPOOR is a data-handling and processing code. Its function is to reorder and sort the SPOOR output data to permit more efficient processing by SCAWDEN.

D. TEMPEST. TEMPEST is a dynamic, Monte Carlo, storm- and rain-cell morphology simulator. It sets up a fixed, user-specified storm geometry

composed of any number of separate "zones"* and then generates a characteristic set of moving, elliptical rain cells within each. These cells are transported with input-specified velocities within each zone, and they start, grow, and die out according to input PDFs for initial cell size, cell aspect ratio, cell orientation, maximum cell size during its lifetime, and starting life-cycle status of the cell. Appendix D gives specifics of the TEMPEST model.

1. Coordinate Systems. Because different parts of our code system came from different sources, we have used three coordinate systems to avoid major recoding efforts.

The basic geographic (I,J) coordinate system and a corresponding rectilinear system (x,y) are shown in Fig. 3; the (I,J) coordinate system and the (I,J)-to-(x,y) transformations are described in Appendix C.

The SPOOR, SCAWUEN, RAIN, SHASTA, and SHASTAX codes use (I,J) and (x,y) coordinates.** TEMPEST, on the other hand, uses its own rectilinear coordinates (X,Y), also shown in Fig. 3; all TEMPEST calculations are performed with respect to that system. The system origin is defined by the storm-geometry inputs. The transformation between (x,y) and (X,Y) coordinates is X = -y, Y = x.

---

*We have incorporated the geometry package from the MCN[5] family of LASL Monte Carlo codes into TEMPEST. This sophisticated geometry system allows us to define any configuration of storm zones described by quadratic surfaces.

**Transformations from (LAT, LONG) geographic coordinates to (I,J) are also included in some instances, such as for SPOOR scenario inputs.

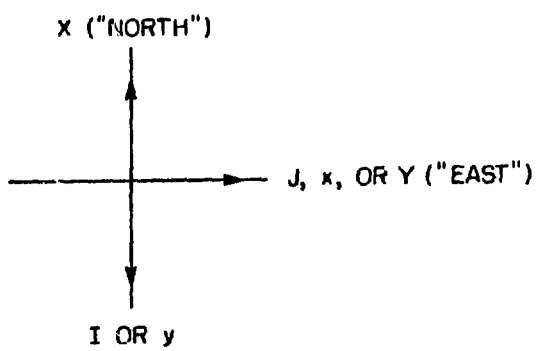

Fig. 3.
The (I,J), (x,y), and (X,Y) coordinate systems.

2. Storm Geometry Example. Figure 4 shows a storm-system geometry that characterizes the important features of the composite storm structure of Fig. A-1. We used a simple four-ellipse configuration to construct the storm zones in Fig. 4, although, for general purposes, the geometry package in ACRA offers much more flexibility.

The synoptic storm center is as indicated near the intersection of zones 1, 3, 4. Zone 1 represents the ragged stratiform precipitation region, whereas Zone 2 includes the area of light, continuous precipitation discussed in Appendix A. Zones 3 and 4 respectively depict the cold frontal band and the postfrontal shower region.

Figure 5 shows the same storm with an overlaid set of representative rain-cell centers and typical cell velocities. Note the characteristic zone-to-zone variations in rain-cell density. The number of cells is determined by using the methods described in Appendix D and the concepts outlined in Appendix A. Zone 1, the ragged stratiform region close to the storm center, has the most dense precipitation and is where the heaviest "continuous" rains usually fall. Zone 4, the postfrontal region, typically has the least rainfall coverage. The coverage in this region (as in the other regions) varies greatly from storm to storm but is perhaps more dependent on local geographic and seasonal conditions than is coverage in the other regions. Cold air flowing over relatively warm, moist regions will often cause more extensive precipitation coverage in Zone 4, both in area and density. Northern Germany, with winds fetching moisture off the North Sea, may have relatively high winter precipitation coverage under northwest flow (Zone 4).

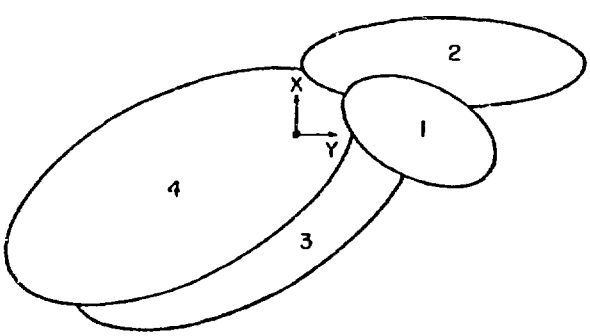

Fig. 4.
Illustrative storm geometry.

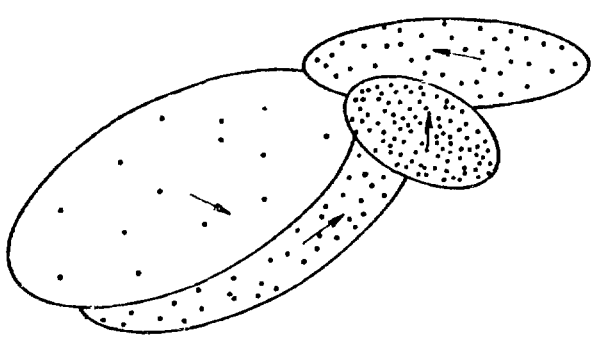

Fig. 5.
Representative rain-cell centers and zonal cell velocities.

A storm structure such as that shown in Fig. 5 can be used to demonstrate the role of climatic storm tracks in determining precipitation behavior at a particular site. For instance, Woronicz[6] shows primary and secondary storm tracks for Western Europe for each month of the year. All months are characterized by two preferred tracks in the area of Germany. A northern storm track exists from Scotland through southern Scandinavia, and a southern track runs across France and Italy. The northern track would subject German stations to a preponderance of transections across Zones 3 and 4. The southern track might put German sites in Zone 2, but more often they would be in the far regions of perhaps a more extensive Zone 4, where onshore northwest winds might bring weak, shallow showers.

The cell movement reflects a circulation about the storm center representative of middle tropospheric winds. Appendix A suggests that this relationship between cell movement and mean airflow is simple and useful.

3. Mesoscale Rain-Cell Structure. Our goal with the TEMPEST simulator is to provide a dynamic structure of rain-cells that debris particles must traverse, a structure whose statistical properties match what we know about such structures in nature and whose basic parameters we can adjust to allow normalization of the overall ACRA system to pertinent integral data, such as average rain-area fractions, rainfall frequency distributions, and average rain rates.

A main problem, therefore, is to specify statistically the time-dependent geometric properties of this structure (cell position, size, number density, and shape with respect to the mean flow). A concomitant problem is to specify how the properties of the precipitation field depend on position in the large-scale synoptic storm pattern. These topics, discussed in Appendix A, form the bases of the TEMPEST model.

TEMPEST provides a field of statistically generated precipitation cells in the same phase-space domain as that traversed by the SPOOR trajectories. These two fields can be combined to establish locations and frequencies for debris-particle encounters with precipitation cells of appropriately varying size, density, and intensity.

4. TEMPEST Inputs and Outputs. The input for TEMPEST consists of the following.

- Storm-geometry specifications.
- Rain-cell velocity for each storm zone.
- PDFs for rain-cell aspect ratios, maximum cell size, and cell orientation with respect to cell velocity.

TEMPEST output consists of the state variables (position, size, orientation, and life-cycle status) of all rain cells at all time steps for input to SCAWUEN, plus printouts of selected cell summaries for monitoring purposes.

D. SCAWUEN

This code transforms all the TEMPEST cell data into a moving storm system in geographic (SPOOK) coordinates (Fig. C-2, for example) and then assimilates the RESPOOK particle data, identifies resultant interaction sites for debris particles in precipitation cells, calculates local within-cell scavenging probabilities, produces a corresponding set of scavenged-particle weights, transports these scavenged particles to the ground, tabulates their statistical properties, sets up a Lagrangian tally grid based on these properties, and, finally, tallies the intensity of ground-deposited debris on this grid. These functions of Scawuen are more clearly understood in terms of the logic-flow diagram of Fig. 6 and the specific SCAWUEN models described in Appendix E.

Input for SCAWUEN consists of the shot-time location on the TEMPEST time axis, the starting position and velocity of the TEMPEST storm in SCAWUEN coordinates, rain-intensity parameters γ_x and γ_y, vertical-intensity tables $\alpha(z)$, a horizontal velocity $\vec{v}_{r_0}$ for transport of scavenged particles, PDF tables for the maximum cell-intensity parameters R_0, and the tally-bin parameters K, N, and F. The output of SCAWUEN is the dimensions, geographic locations, and deposited-debris intensities of a set of ground tally bins for input to SHASTA, plus corresponding printouts of user-selected portions of the intermediate and final SCAWUEN results.

E. SHASTA. SHASTA tallies collateral-damage effects. It uses the output from SCAWUEN and an input population data base to do three things: (1) identify and locate population points within the ground-deposition tally grids, (2) calculate "infinite whole-body dose" (IWBD) contributions for all time steps and each affected town, and (3) find the total IWBD for each town, summed over all time steps.

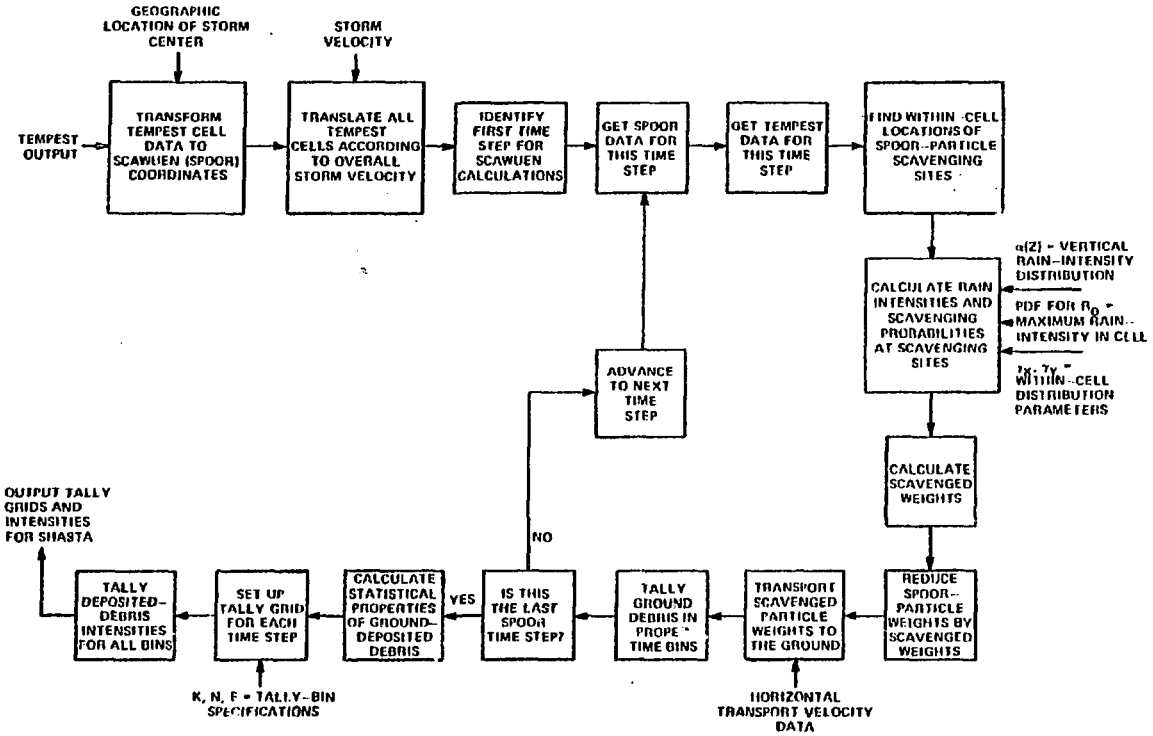

Fig. 6.
Functional flow diagram for SCAWUEN.

The population data we use are taken from RAND's TANDEM data base for Central Europe.[7] These date are incorporated into a specially prepared population data base that we designed specifically to minimize computing time in SHASTA.

SHASTA estimates IWBD (see Appendix B) as

d_{jk} = IWBD at population point k from deposition during time step j

$$= 2.02 \times 10^{4} t_j^{-0.24} \frac{Y}{M} I_{jk} \quad ,$$

where I_{jk} = deposited-debris intensity of the tally cell within which population point k is located at time step j,

Y = total fission-equivalent yield of the source cloud,

M = number of SPOOR particles in the calculation,

t_j = time from fission.

The total IWBD at point k from the source cloud for all time steps is then

$$D_k = \sum_{j=1}^{N} d_{jk} \ ,$$

where N is the total number of time steps in the SPOOR simulation.

Input to SHASTA is the ground-debris information from SCAWUEN and the SHASTA population data base. The SHASTA output is a set of data summaries for each affected population point; these summaries include geographic location, population, and D_k for each town, sorted and listed to facilitate follow-on user analyses. A final tally lists the cumulative rainout-affected population totals within specific D_k contours.

G. SHASTAX. This code combines the output from multiple SHASTA calculations to give total effects tallies for multishot simulations. SHASTAX makes linear superpositions of the individual D_k levels from an arbitrary number of SHASTA runs to tally total multishot IWBD for affected population centers. The output format of SHASTAX is similar to that of SHASTA.

H. RAIN. We designed our storm and rain models to be fundamentally literal and to include certain basic, adjustable parameters so we could use a broad spectrum of meteorological data (1) to verify the models and establish proper operating regimes for our system parameters and (2) to determine the real-world climate-based probabilities we can attach to our simulation and sensitivity studies (see Sec. VIII).

The RAIN code addresses both of these goals. The specific function of RAIN is to extract explicitly the time history of ground rainfall implicit in any TEMPEST-SCAWUEN simulation. Ground-rain data such as frequency distributions and time-averaged rates are implicit statistical properties of an ACRA simulation just as they are in a real-world situation, and these properties must be derived or "measured" by simulating the real-world experiments that are used to generate the meteorological data.*

In the RAIN code, we tally total rain at a fixed ground point ("rain gauge") during each time interval Δt in a TEMPEST-SCAWUEN calculation. RAIN is essentially the SCAWUEN code with modified input and tallying modules; it substitutes the input ground point for the normal RESPOOR output, uses a standard TEMPEST output, and, for each Δt, time-integrates (over Δt) the rain

---

*The same statistical and the same time- and space-resolution considerations also prevail in the ACRA "measurements" as in the real world.

intensity from all cells passing over the point during Δt. Appendix F describes details of these integrations.

The RAIN output is a listing of total rain at the ground point during each Δt. We can bin and average these data as desired to provide frequency and average-rain-rate information with any desired time resolution between the limits Δt and T (total simulation time).*

VII. ACRA OPERATIONAL FEATURES

The eight independent ACRA codes are designed so that communication between appropriate codes is achieved through conjoined input-output designations. Figure 7 shows the ACRA functional flow diagram. In the general case, all codes may be exercised in one action to obtain end results. ACRA does, however, give the user the flexibility to "save" outputs from any code and terminate the execution stream at that point so that he can review computational results before executing the next code in the sequence.

A typical course of action for a user studying rainout effects with ACRA might be first to use the TEMPEST code to generate a number of storms that have precipitation cells of various desired characteristics. After reviewing the results, the user might make several runs with the RAIN code, varying rain-intensity inputs and using any of the storms previously generated. Once the user feels he has properly modeled the storms, he is ready to continue his analysis.

After identifying the appropriate atmospheric-turbulence spectral data to be used as input, the user would make a GEBESO run to generate the $\beta_{j,i}$ parameters needed as inputs to the SPOOR code (debris-cloud simulator). At this point, he might use SPOOR to generate a set of debris clouds and then make a RESPOOR run with the SPOOR outputs to build input files for use with SCAVDEN.

Using any of the debris clouds and any of the storm systems, the user can then execute the SCAVDEN code (scavenging simulator) and the SHASTA code (tallies rainout effects from a single shot). A final user option is to execute the SHASTAX code to tally rainout effects from multiple debris clouds by combining, in any order, the SHASTA results obtained for the single shots.

We have optimized all eight programs to maximize executional efficiency and reduce overall execution time (see Table I).

---

*We typically use Δt = 0.1 h and T = 5-10 h.

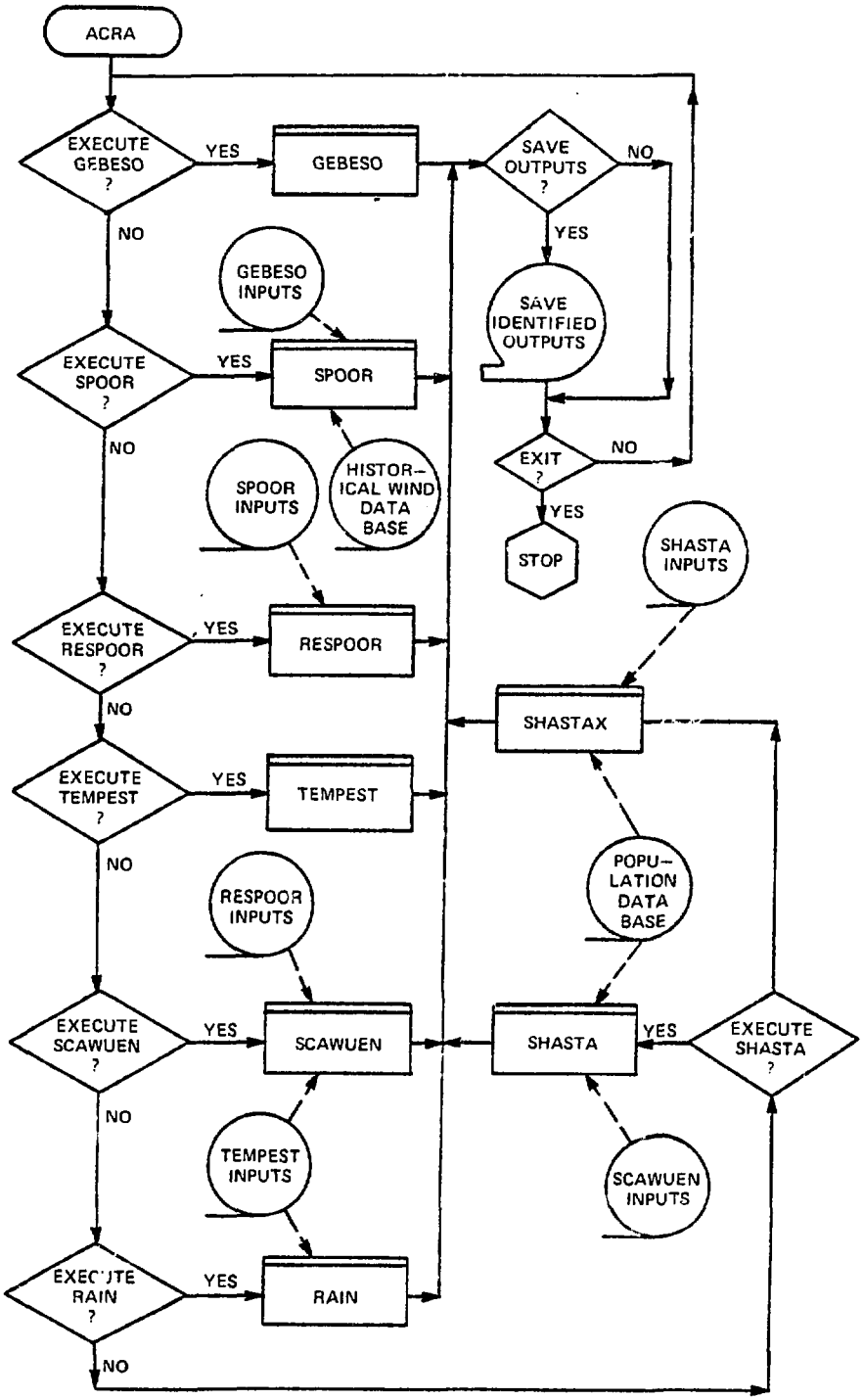

Fig. 7.
ACRA functional flow.

TABLE I

EXPECTED RANGE OF EXECUTION TIMES FOR CODES
IN THE ACRA SYSTEM
(CDC 7600)

Code Name	Range of Execution Time (min)	
	Minimum	Maximum
GEBESO	1.5	5.0
SPOOR	0.9	4.0
RESPOOR	2.0	8.0
TEMPEST	1.0	3.0
RAIN	0.4	1.5
SHAWUEN	0.5	3.0
SHASTA	0.6	2.0
SHASTAX	0.5	3.0

VIII. RAINOUT CALCULATIONS--SCOPING AND SENSITIVITY STUDIES

Because a bewildering number of physical variables influence the real-world collateral-damage effects from rainout, an exhaustive examination to determine the differential roles of all these variables for rainout assessments would be impossible. Fortunately, however, rainout collateral damage is an inherently integral phenomenon and therefore is relatively insensitive to details as to how most of the pertinent physical variables actually vary with time and space, at least over regimes of practical military interest. Moreover, even if we knew the exact sensitivities of rainout effects to these variables, they would generally be masked by uncertainties in the statistical fluctuations introduced by the fundamental meteorological variabilities (Sec. III).

We do not mean to imply that one can simply dismiss such factors from consideration, but rather that most of them will, in fact, be of secondary importance in rainout assessment, provided we properly understand and scope their roles. We believe this scoping to be an important task, as evidenced by the substantial effort we have expanded in scoping studies and by the complexity of the assessment system we evolved.

A major part of our effort has therefore been directed to progressively eliminating as many irrelevant variables as possible and to identifying the driving elements and parametrically evaluating their roles in raincut-effects assessment. Certainly, we have not been totally successful in achieving these somewhat idealistic goals, and several areas may require more work. Nevertheless, we have made major progress toward these objectives in developing and implementing the ACRA modeling concepts, and both the overall character and the details of this comprehensive calculational system reflect a host of insights we have gained during our studies. We have also used the ACRA system in its present form to simulate detailed rainout collateral-damage effects for over 500 representative nuclear shots to examine how these effects depend on a variety of basic physical and modeling variables. We will discuss the results of these simulations in the following sections.

A. Single-shot Studies.

1. A Typical ACRA Calculation. Figure 8 shows the "threatened" population points for a 1-kt fission shot in West Germany (shot No. 2 of the

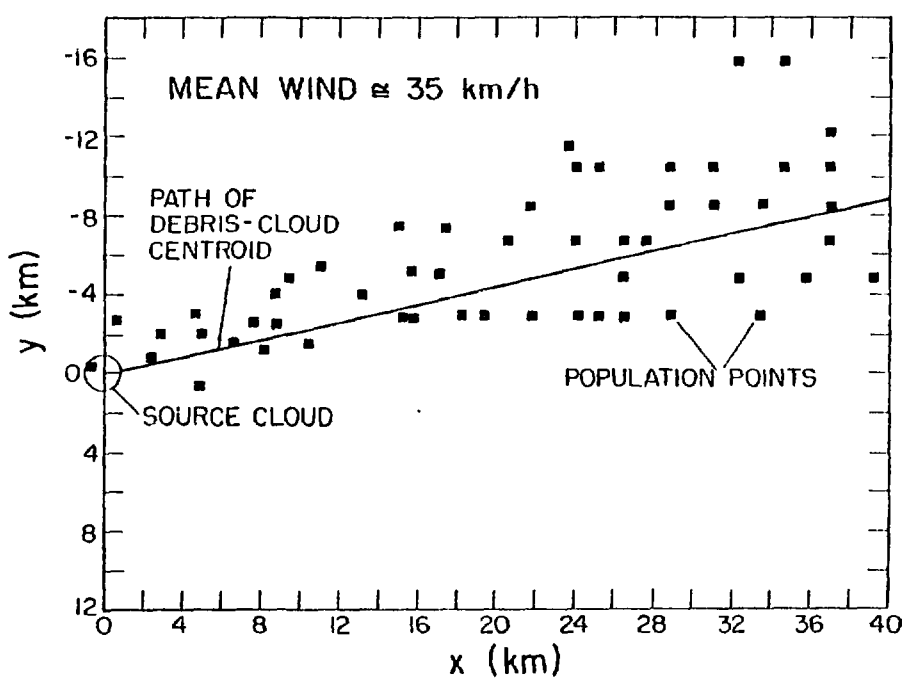

Fig. 8.
Population points within 40 km over which debris passes; single 1-kt shot.

referenced scenario discussed in Sec. VIII-B-1). The figure indicates the initial stabilized source cloud, the path followed by the centroid of the debris cloud, and those population points within 40 km over which some parts of the cloud passes.* The mean wind speed for this case is ~35 km/h, in the direction along the centroid path. Table III (p. 40) gives the source-cloud dimensions. Population levels for the 54 indicated points range from 31 to 4400; the total population for all 54 points is 48 471. (No debris cloud is shown in the figure because our debris clouds consist of three-dimensional time- and space-varying ensembles of individual points.) This tally of "shadowed" population points is effected by bypassing the rain-cell and scavenging simulation parts of TEMPEST and SCAWUEN, through simple adjustments of input parameters.

Figure 9 shows a population-point plot for the same 1-kt shot used in Fig. 8, but now with a typical TEMPEST-SCAWUEN rainout calculation included to simulate a medium-rain situation for west Germany. The designations light, medium, and heavy rain are used to indicate different rain area fractions (and, hence, different average rain rates). Figure 9 shows only those population points that receive rainout deposition, again for only the first 40 km.** The 12 points in Fig. 9 range in population from 156 to 1400; the 12-point total is 6042. Figure 10 plots the number of people affected in the calculation as a function of infinite whole-body dose. A single, "unlucky," high-dose event is indicated at D = 520, N = 700; this event occurred at the point indicated by the arrow in Fig. 9.

Another useful type of plot (Fig. 11) shows dose versus distance from the shot point for the population points affected by rainout.*** This figure illustrates four characteristics of any rainout situation: (1) affected points have a bounding "envelope" that is determined primarily by yield and mean wind field; (2) the envelope is very nonlinear at distances within a few tenths of an hour of cloud-travel time from the shot and has a characteristic range of

---

*For convenience, we limit the plot in Fig. 8 to 40 km. The calculation, of course, extends well beyond that limit.

**Four points in Fig. 9 are different from those of Fig. 8, because the rain-rate-dependent, scavenging-site-to-ground transport included in the rainout calculation causes a small change in the distribution of ground-deposited debris. The population points affected in the two cases are thus not quite identical.

***This is the same calculation as for Figs. 9 and 10.

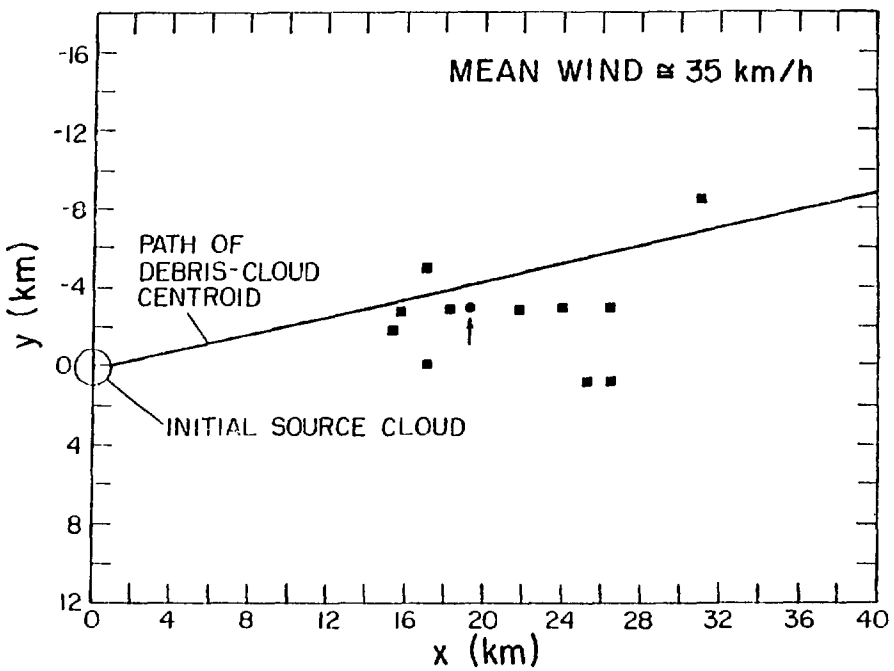

Fig. 9.
Population points within 40 km that receive rainout deposition; single 1-kt shot in medium rain field.

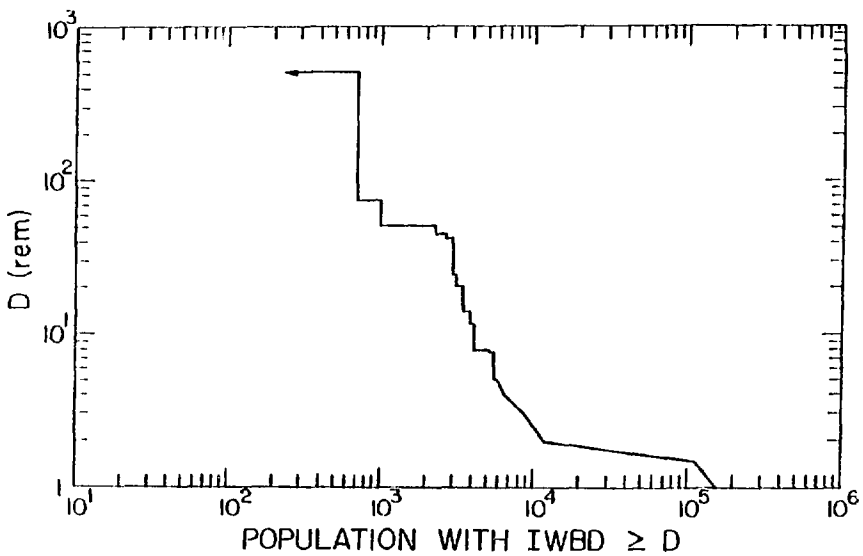

Fig. 10.
Dose-vs-population distribution for illustrative calculation; single 1-kt shot in medium rain field.

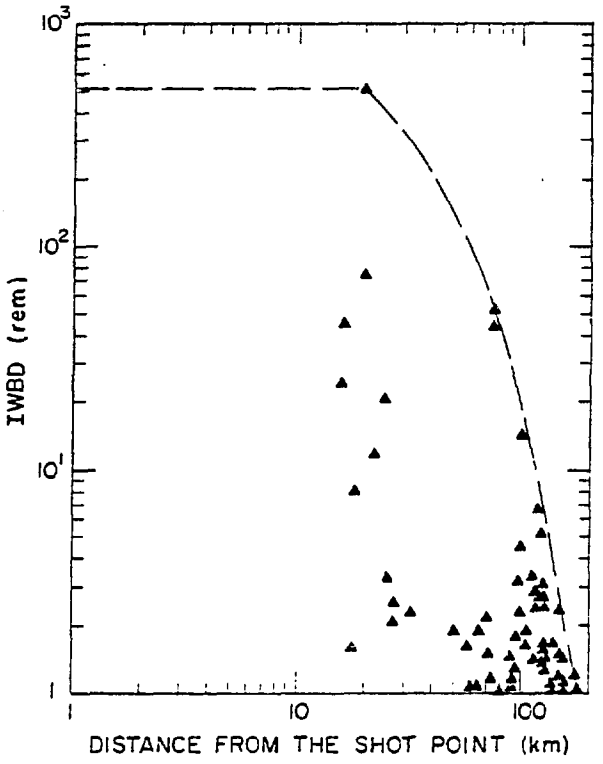

Fig. 11.
Dose vs distance for illustrative calculation; single 1-kt shot in medium rain field.

maximum IWBD threat that is determined primarily by yield and initial cloud size; (3) there is a maximum range beyond which dose falls off very rapidly because of depletion and cloud dispersion; and (4) most population points receiving rainout doses are well within the bounding envelope.

2. Statistical and Numerical-Meshing Studies. Several of our early code-development and single-shot-sensitivity studies concentrated on tradeoffs between computer running time and numerical-meshing and statistical-sampling parameters. This work established meshing schemes and sample sizes required to achieve adequate numerical accuracy within practical computing times. We examined the effects of the following:

- Number of β terms in the SPOOR recursion relationships.
- Number of SPOOR source particles.
- Tally-bin radial-meshing models.
- Tally-bin mesh sizes.
- Time mesh size.

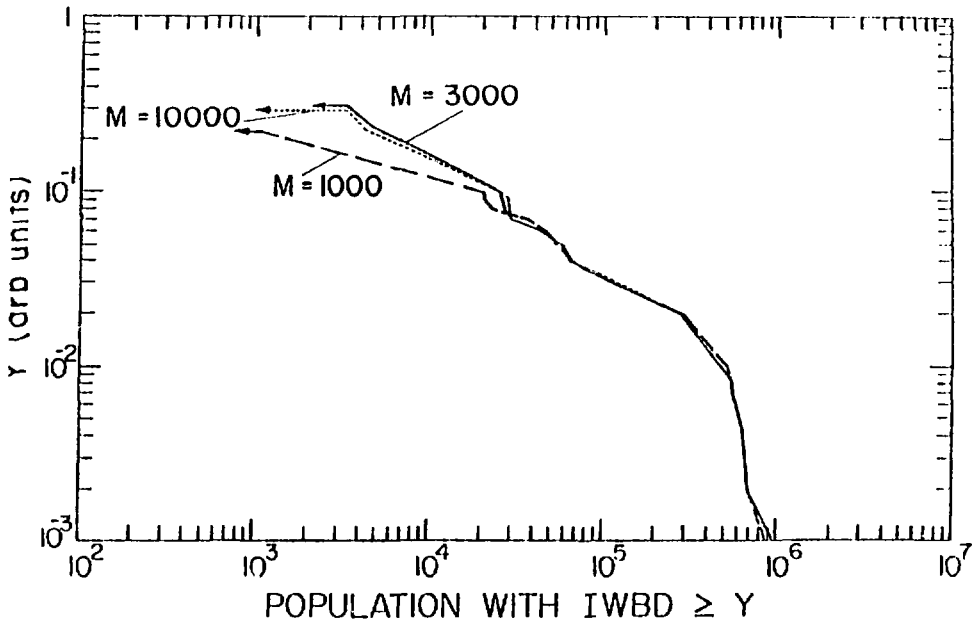

Fig. 12.
Effect on rainout results of varying source sample size.

We found that rainout results and computer running times were insensitive to the number of β terms in SPOOR, for numbers between 3 and 40. We used 10 β's in most of our subsequent work.

Computing times in the ACRA system vary in a roughly linear fashion with the number of source particles M, as we would expect. Figure 12* shows results for a set of point-source calculations designed to study the effect on rainout results of varying M. We found a few thousand particles to be generally adequate; most of our simulations use M = 5000.

Developing an adequate tally-bin scheme is difficult because extreme debris-concentration gradients in both time and space must be treated to achieve adequate resolution in the results, particularly near the origin. A Lagrangian tally grid is a necessity; even then, one is still trying to resolve a very complex gound-deposition field whose spatial distribution is essentially unknown. We found the second moment of ground-deposited debris about the centroid to be useful in characterizing these spatial distributions, and, after experimenting with several semiempirical meshing models, we settled on the one

*Our sensitivity results are often presented only in terms of relative dose effects in arbitrary units, when only relative results are available or pertinent. Absolute rainout effects are presented in terms of tissue doses (rem).

described in Appendix E. With this scheme, rainout results appear to be relatively insensitive to tally-bin size. This insensitivity is shown in Figs. 13, 14, and 15 for 1-, 2-, and 10-kt shots, respectively. An inherent pitfall in using small radial-mesh sizes is shown in the 40x(40+20) curve of Fig. 15. Near the shot point, statistical fluctuations in the rapidly varying spatial gradients of ground-deposited debris can give abnormally small $\sigma^2_{r_j}$ with correspondingly small bin sizes and aberrantly large dose estimates (see Eqs. E-13, E-14, and E-15). This phenomenon is strictly a statistical anomaly and is inherent in the tally-bin meshing scheme. These errors are significant only within the first few tenths of an hour from the origin, but the effect normally causes us to restrict the number of radial bins to no more than 15-30. Empirically, this range gives a good compromise between overmeshing the cloud near the origin and undermeshing it elsewhere.

Another source of uncertainty in our calculations, again within ~0.3 h of cloud-travel time from the shot point, is in the time-mesh size, Δt. We typically use Δt = 0.1 h to avoid the larger computing times required for smaller Δt's. As the calculation cannot give good resolution for the first two

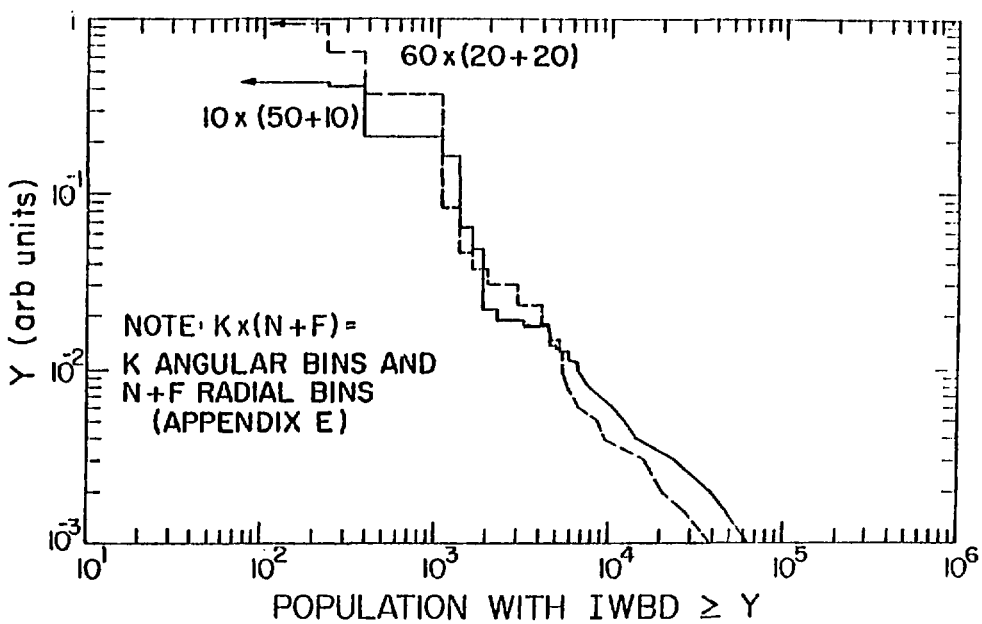

Fig. 13.
Effect on rainout results of varying the tally mesh; single 1-kt shot.

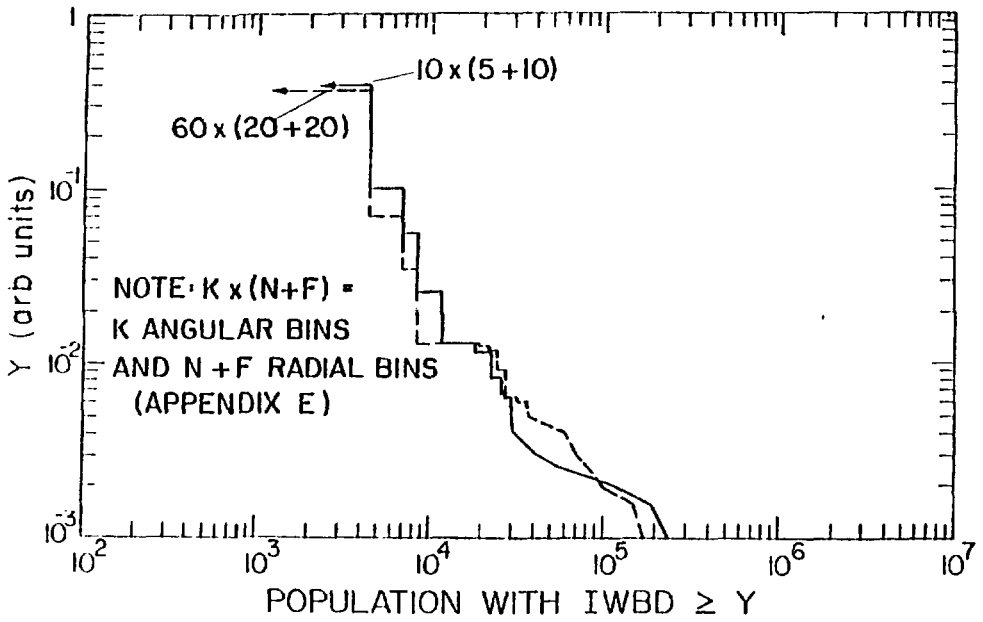

Fig. 14.
Effect on rainout results of varying the tally mesh; single 2-kt shot.

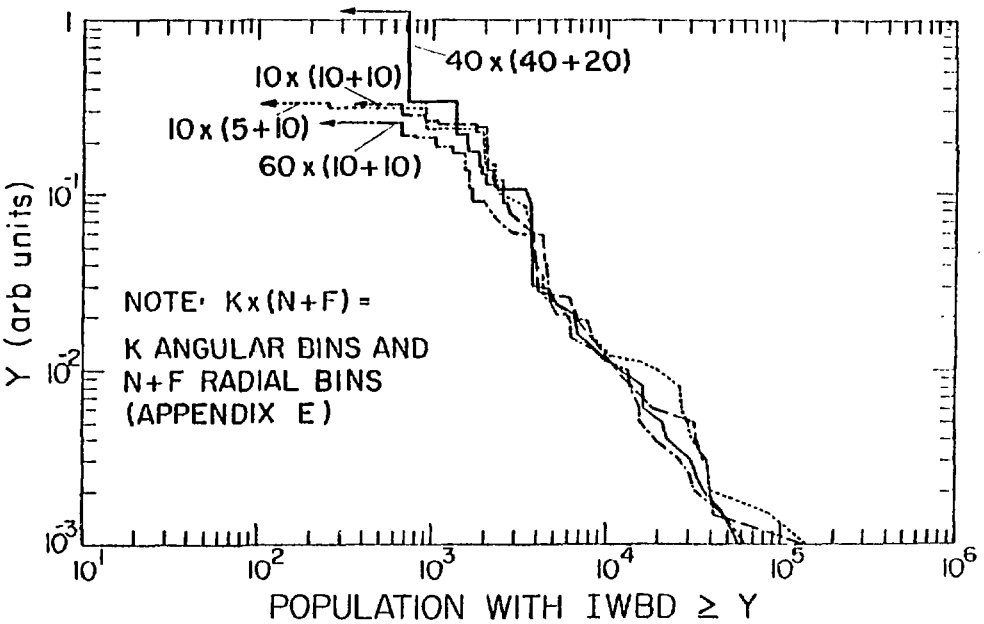

Fig. 15.
Effect on rainout results of varying the tally mesh; single 10-kt shot.

or three Δt's, there is an uncertainty in detailed dose calculations over this range, the same range discussed in the previous paragraph. A solution to this problem, as well as that in the previous paragraph, would be to use a finer Δt near the origin; that is, use a time-varying time mesh. This option is not presently available in ACRA, but it would be a useful extension of the system.

We have made empirical studies of the two uncertainties mentioned in the previous paragraphs by using different Δt's and a variety of tally-bin meshes. These studies have led us to consider our dose results for the first few tenths of an hour from the origin to be uncertain by a factor of up to 2 or 3 (generally on the high side.)

3. Initial Sensitivity Studies. Several of our early single-shot series also examined physical factors that we expected to be of secondary importance for determining rainout effects. These factors included the following:

- Spatial distribution of activity in the source cloud.
- Input turbulence spectrum for SPOOR.
- Velocity of the TEMPEST storm.
- Velocity of TEMPEST rain cells.
- Air-to-ground transport of scavenged debris.

We used various combinations of uniform and Gaussian activity distributions, in both the axial and radial dimensions of representative source clouds, to examine the effects of source internal distribution on ground doses. These effects were small, because the initial activity distributions disappeared so quickly as a result of turbulent diffusion that a debris cloud's "memory" of its initial internal configuration lasted only a small fraction of an hour. Initial cloud size is, of course, more significant.

The role of input turbulence spectrum is less clear-cut. Higher turbulence spreads the debris cloud more quickly over more area than does lower turbulence, but the cloud density is also reduced more quickly. The net effect of these competing factors depends on the local population distribution; however, the differences resulting from different input turbulence spectra usually are not large and are masked by fluctuations in the other variables, notably population distribution. Atmospheric shear from vertical variation in the horizontal wind fields is more important and is automatically included in our calculations (see Ref. 4).

Similar comments apply to the importance of TEMPEST storm and rain-cell velocities. Rainout effects appear to be relatively insensitive to reasonable changes in these variables. This point needs more study but thus far we have found no credible combinations of these variables that produce large sensitivities in the final rainout dose estimates.

Figure 16 illustrates how including the air-to-ground transport of debris-laden precipitation affects rainout doses. Again, this factor seems of secondary importance, but we include it in our rainout calculations (Appendix E).

4. Rain Parameters and Scavenging-Efficiency Studies. Our early studies led us to conclude that rain and scavenging parameters were of more basic importance than those discussed above for determining and characterizing rainout-effects threats. Once again, single-shot parameter studies with ACRA were useful for delineating and scoping the roles of these elements. The elements studied were as follows:

- Probability density function for R_o = maximum rain intensity at the center of a rain cell.
- γ_X, γ_Y = within-cell rain-intensity distribution parameters.
- Scavenging coefficient.
- Yield.

Figure 17 gives the standard R_o distribution we used for most of our calculations. Figure 18 shows the effect of varying R_o for a 0.4-kt shot in medium rain, and Fig. 19 shows results for a 0.4-kt shot in heavy rain. Figures 20 and 21 give analogous results for a 1-kt shot. These figures show several examples of relatively large steps produced by single population points, and such major steps must be considered specifically in making quantitative comparisons. The most notable example is evident at ∿1-3 rem, where a single point has a population of ∿200 000; Table II gives dose data for this point from the calculations in Figs. 18-21. When we examine the results in Figs. 18-21 in detail, we find that threefold variations in R_o generally produce much less than threefold variations in IWBD. We conclude that R_o is not a dominating parameter in determining rainout effects.

Figure 22 shows how varying the rain-intensity distribution parameter affects rainout doses for a 1-kt shot in a heavy-rain field, and Fig. 23 shows analogous results for a medium-rain zone. The parameter γ and the rain-cell

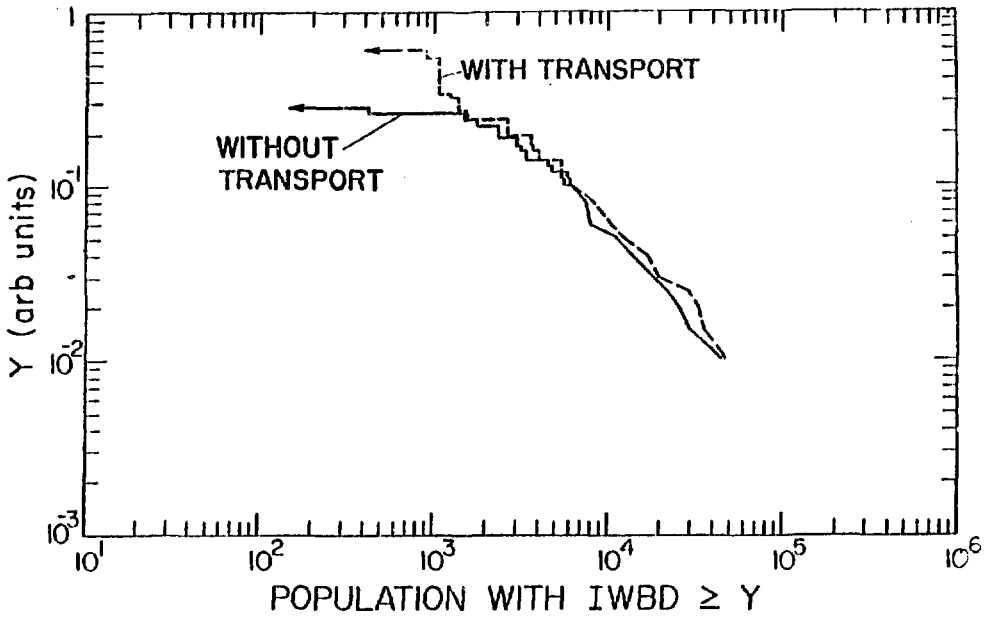

Fig. 16.
Effect on rainout results of air-to-ground transport of debris-laden rain; single 0.4-kt shot.

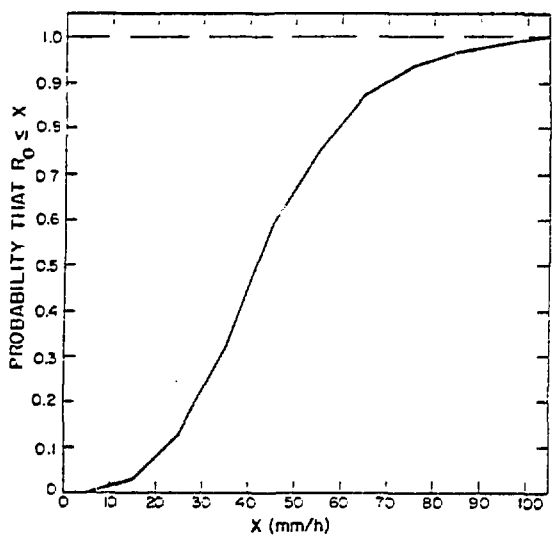

Fig. 17.
Cumulative probability density function for maximum rain intensity R_o at cell center.

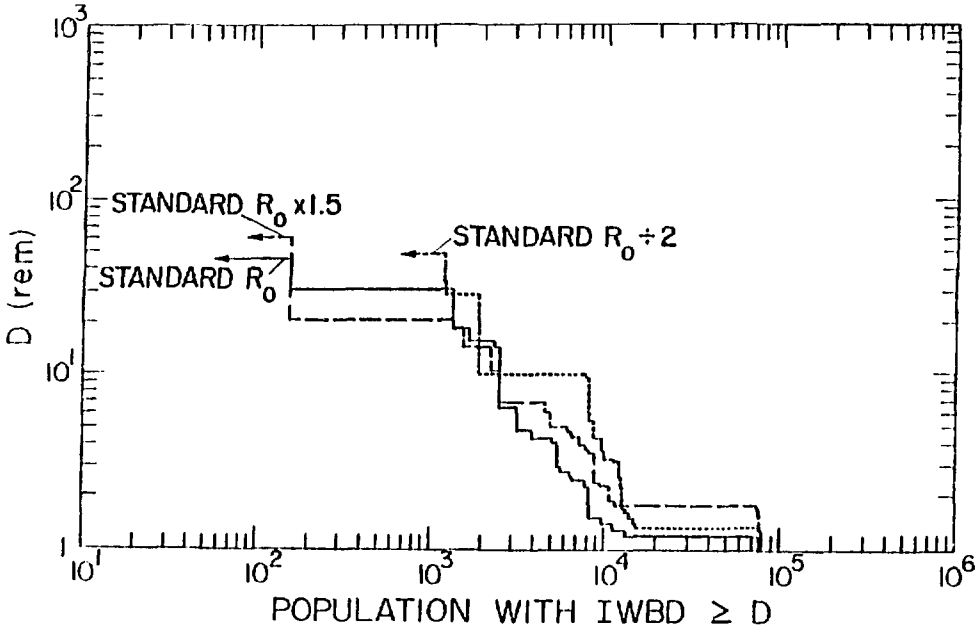

Fig. 18.
Effect on rainout results of varying R_0; single 0.4-kt shot in medium rain field.

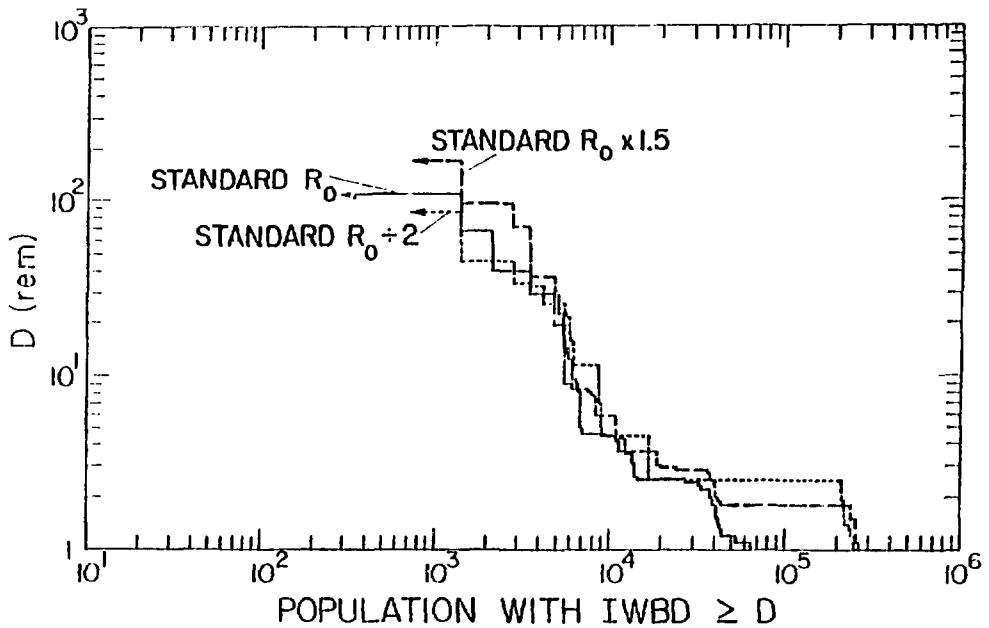

Fig. 19.
Effect on rainout results of varying R_0; single 0.4-kt shot in heavy rain field.

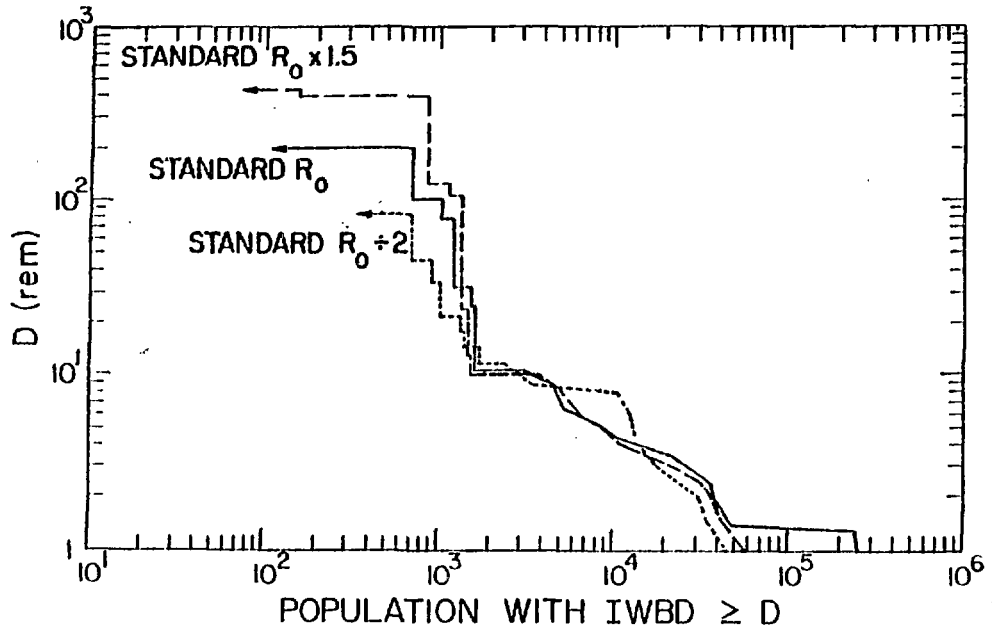

Fig. 20.
Effect on rainout results of varying R_0; single 1-kt shot in medium rain field.

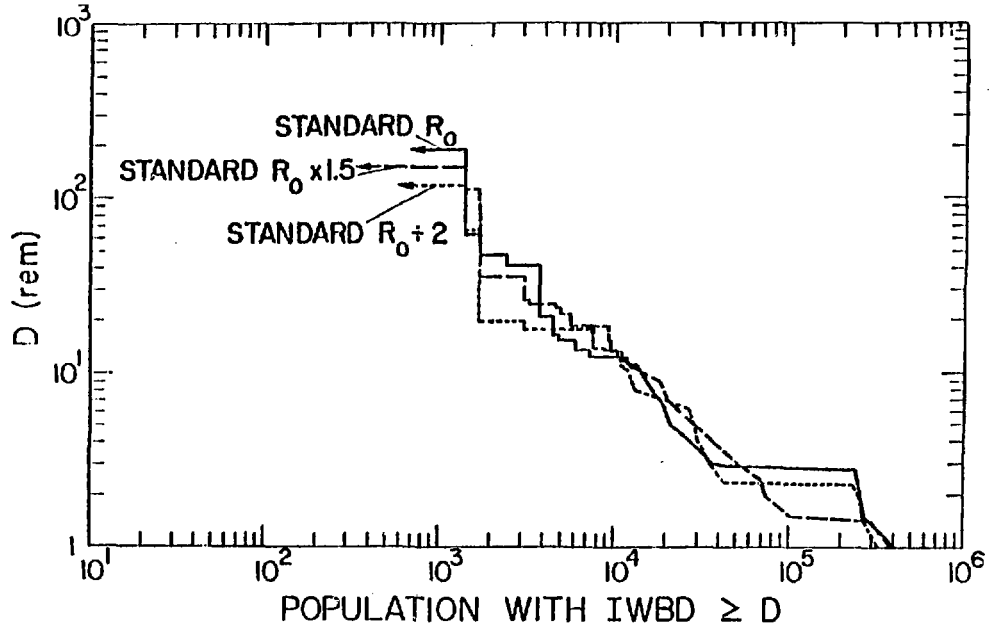

Fig. 21.
Effect on rainout results of varying R_0; single 1-kt shot in heavy rain field.

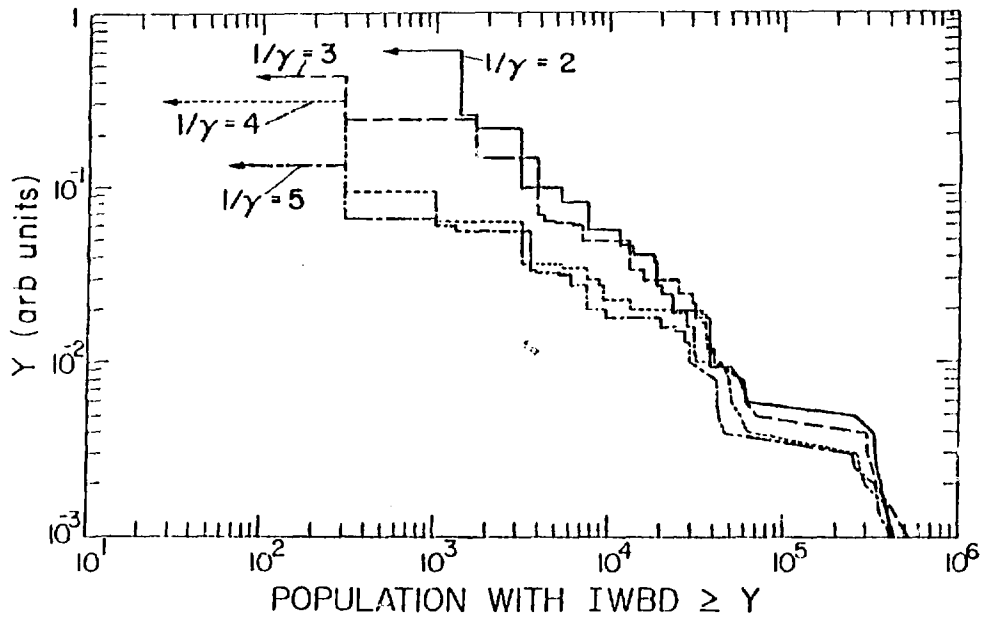

Fig. 22.
Effect on rainout results of varying γ; single 1-kt shot in heavy rain field.

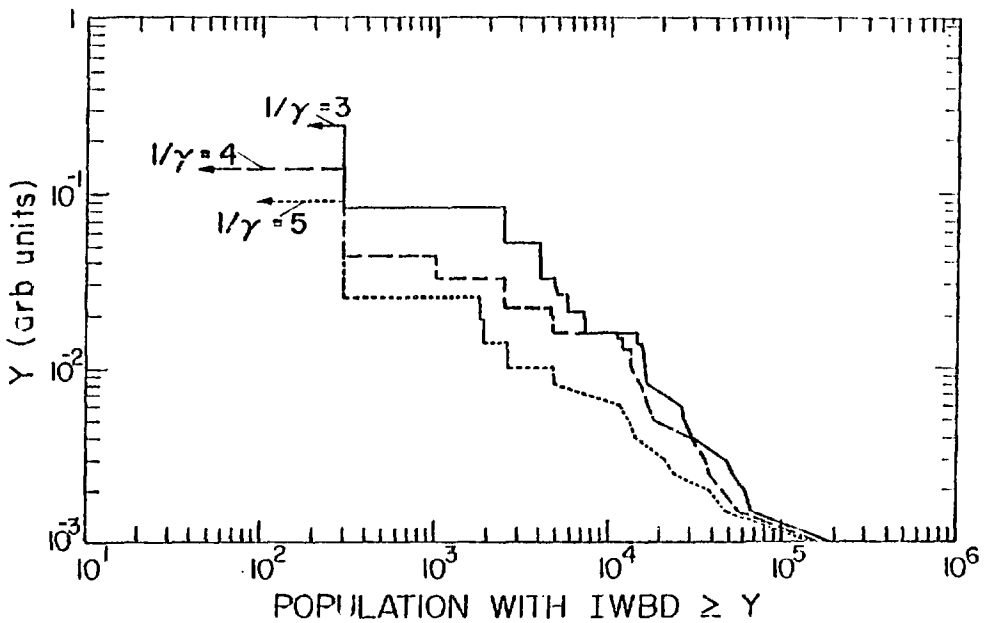

Fig. 23.
Effect on rainout results of varying γ; single 1-kt shot in medium rain field.

TABLE II

IWBD FOR A SINGLE LARGE POINT (POPULATION 200 000)

	IWBD (rem)					
	0.4-kt Shot			1-kt Shot		
	Standard R_o	$R_o \div 2$	$R_o \times 1.5$	Standard R_o	$R_o \div 2$	$R_o \times 1.5$
Medium Rain	<1[a]	<1	<1	1.3	<1	<1
Heavy Rain	<1	2.5	1.8	2.8	2.3	1.4

[a]We arbitrarily eliminate all points from the ACRA printouts whose total IWBD is <1 rem.

size-distribution parameters σ_m^2 and m are of fundamental importance, primarily because of their influence on the small-scale, rain-rate frequency distributions implicit in our model. Rainout effects are relatively insensitive to modest changes in σ_m^2 and m; effects vary with γ as shown in Figs. 22 and 23. Small-scale ($\sim$0.1-h) frequency distributions, on the other hand, are sensitive to all three parameters. These parameters can thus be fixed to an adequate level of uncertainty for rainout calculations by comparing rain frequency distributions from the model with rain data, as outlined in Appendixes A and G. We concluded from these studies that reasonable values for the rain variables were $1/\gamma = 4$, $\sigma_m^2 \doteq 2.5$, and $m \doteq 0.47$. Rainout-effects estimates are insensitive to modest variations of the parameters about these nominal values (see Sec. VIII-B-2).

The scavenging coefficient $\lambda = KR^{0.8}$ is discussed in Appendixes E and H. We examined the sensiti of rainout doses to scavenging efficiency for a 1-kt shot in a moderate-rain field by varying the coefficient K over a range from 0.05 (0.5% probability of being scavenged in 0.1 h by a 1-mm/h rain) to 31.5 (95% probability of being scavenged in 0.1 h by a 1-mm/h rain). Figure 24 shows the results. Rainout effects are insensitive to uncertainties in λ over the most threatening range ($1 < K < 30$) because competing factors tend to cancel one another in determining overall population-versus-dose tallies. A larger λ means that debris concentrations deposited from a cloud before it has been depleted will be larger than when λ is smaller; the concomitant faster

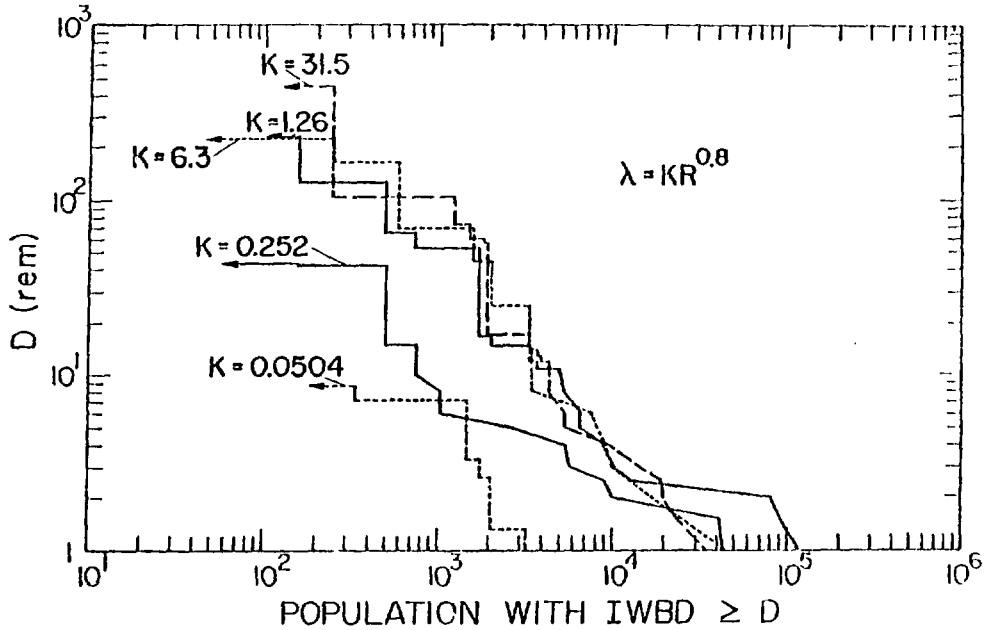

Fig. 24.
Effect on rainout results of varying λ; single 1-kt shot in medium rain field.

depletion, however, means that the threat lifetime and overall threat area are smaller. Also, the probability that debris will be deposited on a population center is smaller when a few intense depositions occur (high λ) than when a larger number of less intense events occur over a wider area (lower λ). Eventually, of course, as λ is decreased, rainout doses begin to fall off because of the reduced deposition rates. The net result of all of these factors is a variation of rainout effects versus λ that tends to have a broad maximum, with modest falloff as scavenging rates become so large that deposition is essentially "instantaneous" and with more rapid falloff as scavenging rates become small. (We also found this same behavior in an early study[8] using a predecessor of ACRA; in that study, all debris clouds were deposited uniformly with a predetermined, constant λ.)

Our rainout calculations to date have concentrated on small fission weapons (≤1 kt and less), but we have also made both single-shot and multishot scoping studies as a function of yield (fission devices only). Table III lists the source-cloud sizes and heights that we used. These dimensions are also shown in Fig. 25, along with a plot of the rain-intensity vertical weighting

TABLE III

ASSUMED SOURCE-CLOUD HEIGHTS AND DIMENSIONS

Yield (kt)	Height of Cloud Center (km)	Cloud Radius (km)	Cloud Thickness (km)
0.4	2.4	0.6	1.4
1.0	2.9	0.9	1.8
2.0	3.5	1.2	2.2
5.0	4.6	1.8	3.0
10.0	6.2	2.4	3.4
20.0	9.1	3.2	4.3

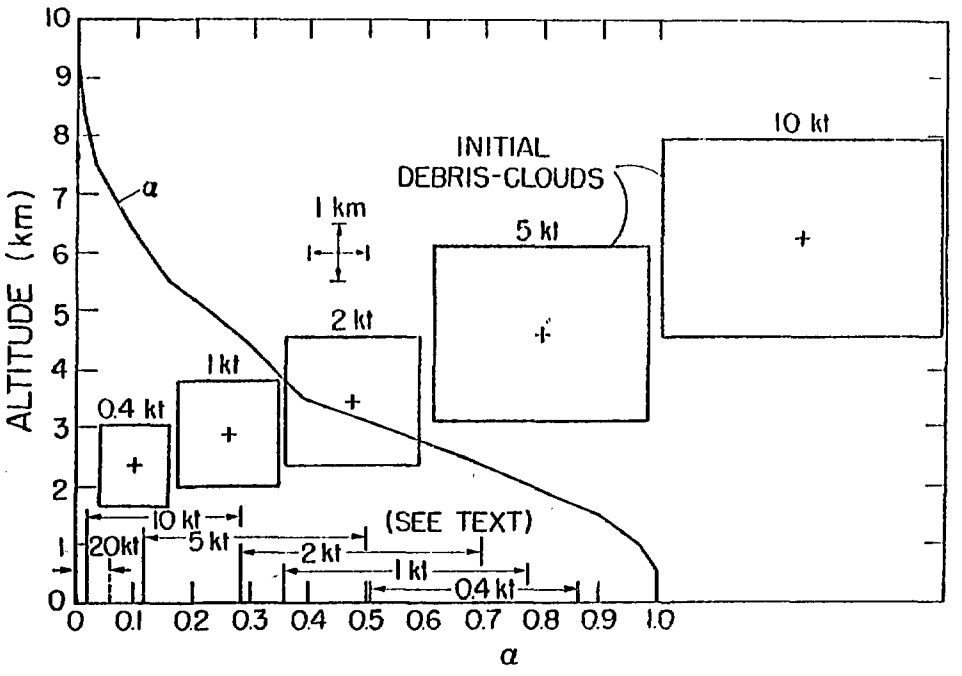

Fig. 25.
Initial debris-cloud sizes and heights and rain-intensity vertical weighting function $\alpha(Z)$.

function $\alpha(z)$.* Figure 25 also shows the range of α within which each source cloud lies and within which most of the debris remains as the clouds are transported and dispersed. Rainout effects as a function of yield are again determined by tradeoffs among several competing factors, particularly higher debris concentration and larger threat areas for higher yields versus reduced rain rates and lower scavenging probabilities at the higher altitudes associated with higher-yield debris. Rain intensities above $\sim$7-8 km, for example, are expected to be too small to produce substantial debris scavenging, and we limited our calculations to 10 kt for this reason (see the indicated α for 20 kt in Fig. 25, for example). Single-shot calculations versus yield are not quantitatively definitive, because statistical fluctuations inherent in the different wind fields and rain cells encountered by the different debris clouds, plus the different local population distributions affected, obscure detailed comparisons; we thus show no quantitative single-shot comparisons. Two points are clear, however, from these studies: rainout effects tend to fall off for yields below $\sim$1 kt, and they tend to level off at $\sim$5-10 kt. We will explore these points more fully in connection with our multishot results.

b. Initial Multishot Studies. A realistic, statistical simulation approach to rainout assessment is subject to statistical fluctuations as in nature, and these fluctuations lead to difficulties in interpreting the results of parameter studies, particularly for single-shot studies. Ideally, we would avoid these problems by simply running a statistically large number of shots as a unit, to sample effectively the variable fields (rain-cell and population fields, for example), and then make comparisons among the combined multishot results. Shot-to-shot fluctuations would then average out, and overall variations would become small in comparison with the effects being studied. Large numbers of shots require large computing times, however; so we have restricted most of our multishot calculations to 10-shot salvos as a useful compromise between increasing the computing time and decreasing the statistical uncertainties in the salvo results.

1. An Illustrative Multishot Calculation. Figure 26 shows the assumed initial source-cloud positions for our standard ten-shot scenario. These

*See Appendixes E and I.

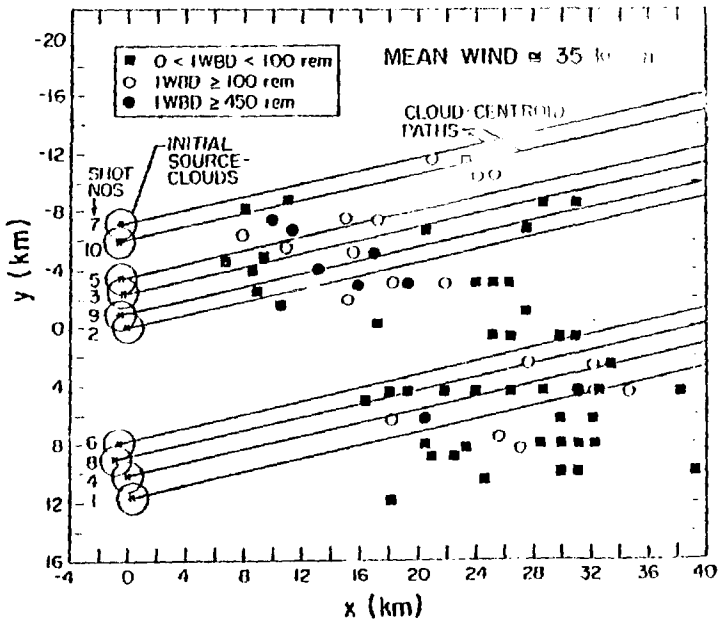

Fig. 26.
Standard ten-shot scenario; cloud-centroid paths for 1-kt shots in typical wind field; rainout-affected population points within 40 km in medium rain field.

locations were actually taken from a simulated tactical nuclear engagement;* the only significance we attach to these locations, however, is that shot density and shot separation distance are probably typical for low-yield defensive nuclear engagements. Figure 26 also shows cloud-centroid paths for a salvo of 10 1-kt shots in a typical wind field (mean wind speed of ∿35 km/h); population points within 40 km of the salvo that receive rainout deposition from a simulation in a light-to-moderate rain field (71 points with total population of ∿40 000); population points (circles) with IWBD ≥ 100 rem (26 points with total population of ∿17 000); and points (solid circles) with IWBD ≥ 450 rem (8 points with total population of ∿7 000). Figure 27 is the corresponding plot of population versus total IWBD.

2. Multishot Rain-Parameter and Scavenging Efficiency Studies. We repeated several of our earlier single-shot sensitivity studies with multishot salvos to determine whether statistical uncertainties in the single-shot

*Shot 2 is located at LAT 50.7394, LONG 9.6752.

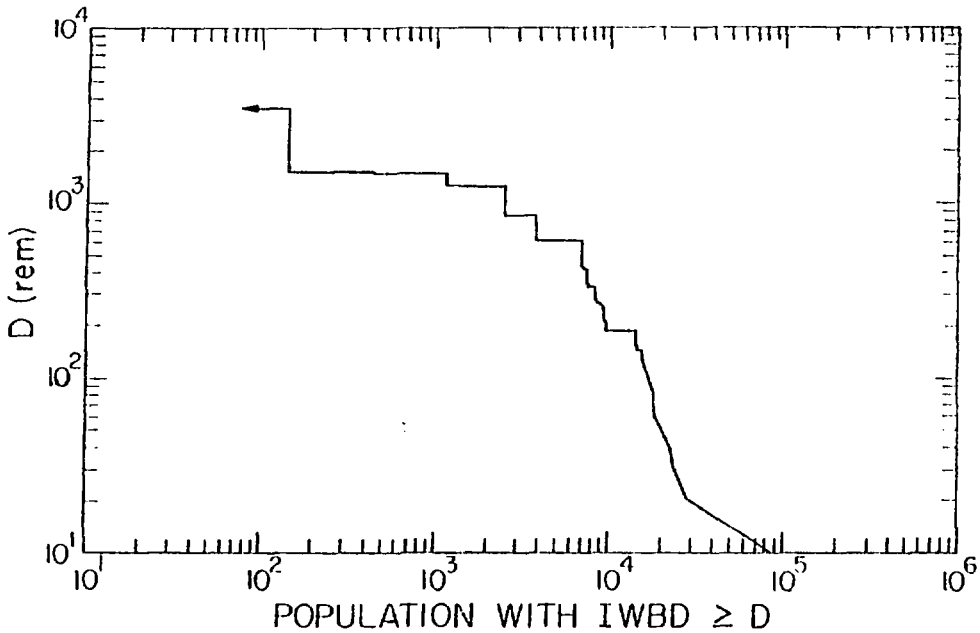

Fig. 27.
Dose-vs-population distribution for illustrative calculation; ten 1-kt shots in medium rain field.

results were misleading us in our earlier conclusions. Figures 28 and 29 show the effect of varying the probability density function for the maximum rain-intensity parameter R_o for 10-shot salvos of 0.4-kt and 1-kt devices, respectively; Figs. 30 and 31 show the effect of varying the within-cell rain-intensity parameter γ for a series of 4-shot salvos; Fig. 32 compares results from 10-shot salvos for different rain-cell size-distribution parameters σ_m^2 and m; and Fig. 33 shows the effect of varying the scavenging-coefficient multiplier K.

We found the same behavior in these multishot studies as we found in the earlier single-shot studies, and our previous conclusions thus remain unchanged.

IX. MULTISHOT PRODUCTION RUNS.

In the preceding sections we determined statistical and meshing parameters for ACRA, discussed the insensitivity of rainout effects to internal source-cloud details and to certain synoptic-scale dynamic storm features, and established reasonable, conservative, operating regimes for rain-morphology and

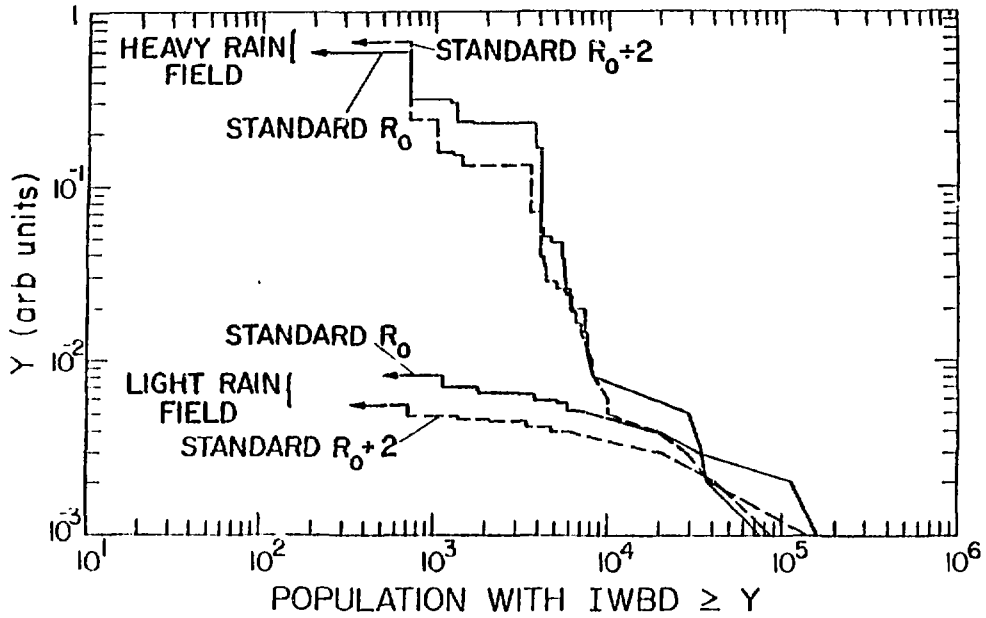

Fig. 28.
Effect on rainout results of varying R_o; ten 0.4-kt shots.

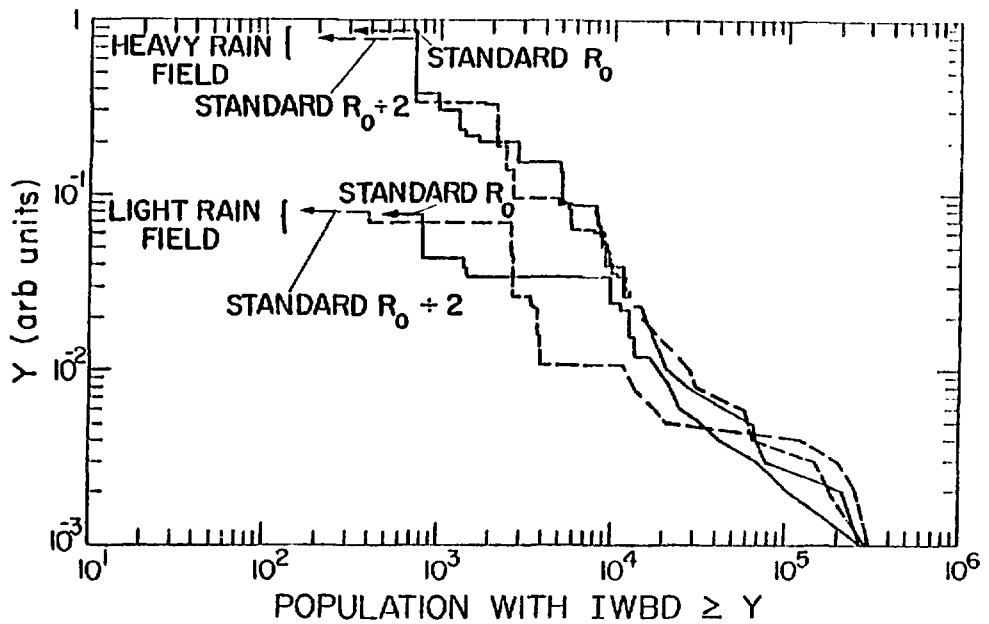

Fig. 29.
Effect on rainout results of varying R_o; ten 1-kt shots.

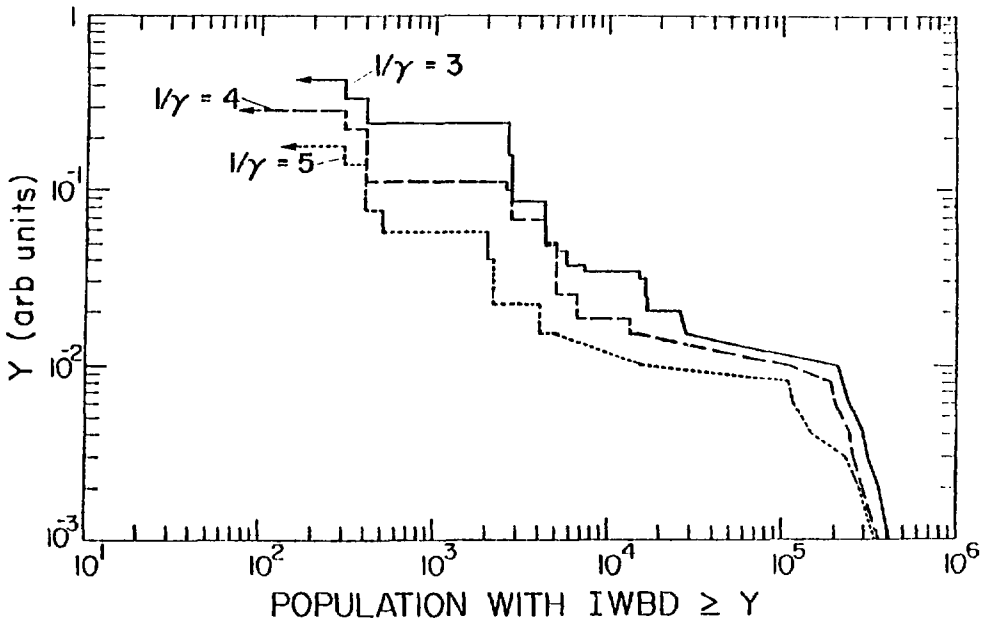

Fig. 30.
Effect on rainout results of varying γ; four 1-kt shots in medium rain field.

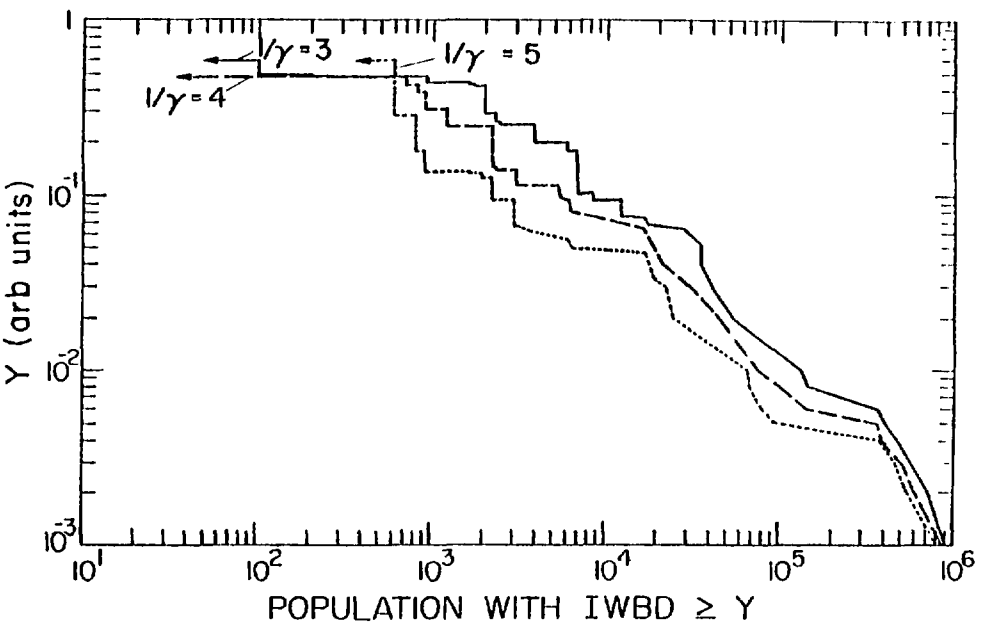

Fig. 31.
Effect on rainout results of varying γ; four 1-kt shots in heavy rain field.

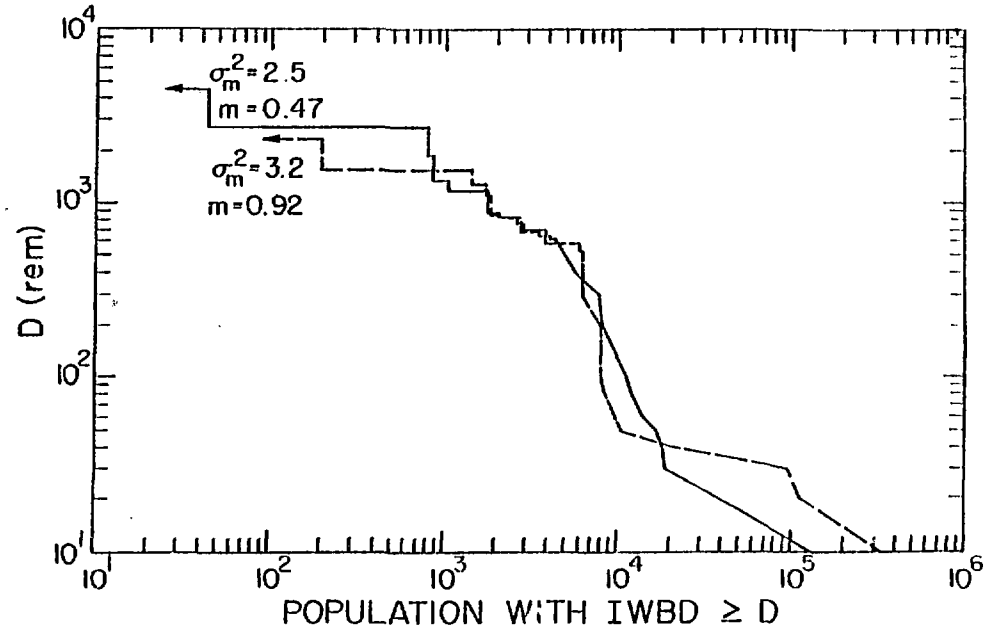

Fig. 32.
Effect on rainout results of varying cell-size parameters σ_m^2 and m; ten 1-kt shots in heavy rain field.

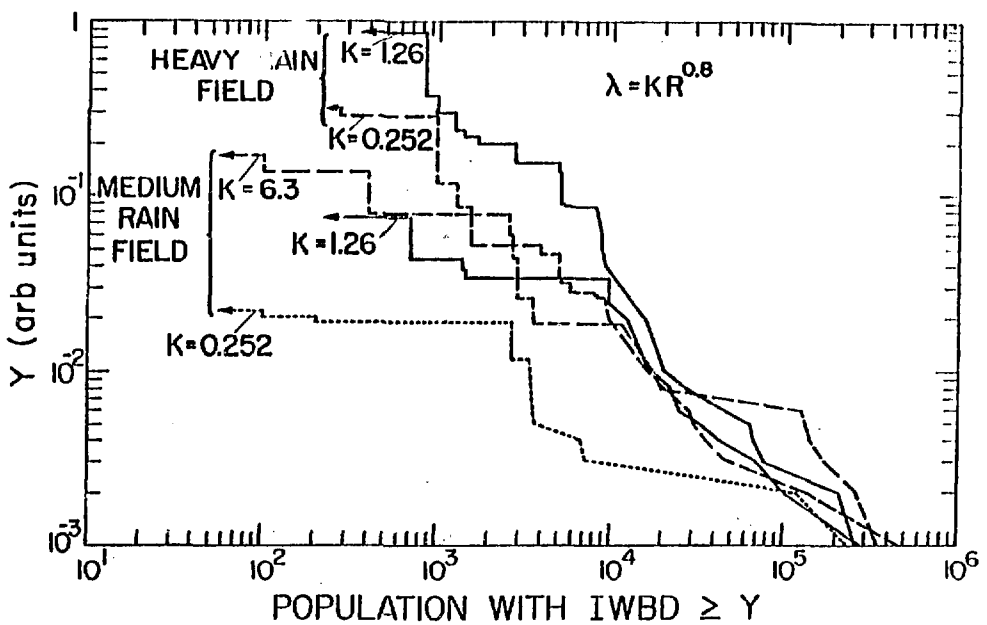

Fig. 33.
Effect on rainout results of varying λ; ten 1-kt shots.

scavenging-efficiency parameters. Most important, we showed that rainout effects are relatively insensitive to variations in rain-structure and scavenging-rate parameters over the most threatening range and that large sensitivites appear only when the parameters are such that rainout effects begin to fall off rapidly. We also demonstrated the fundamentally heterogeneous and probabilistic character of rainout collateral-damage effects, a natural consequence of the character of the driving rain-cell and population fields that determine where rainout depositions will occur.

These studies and the ACRA system (exclusive of the RAIN code) deal with debris transport and dispersal, precipitation morphology, debris-cloud and rain-cell interaction regimes, scavenging and ground-deposition rates, and local population distributions. In the following sections we assess the remaining requirement for rainout, that there must be a precipitating storm system in the area. We also examine the corollary question of the effect of being in different parts of a typical storm system. The goal here is to attach overall occurrence probabilities to our various rainout simulations through the use of regional climatic data.

Our approach is to calculate rainout effects as a function of input rain area fraction (RAF) and then, using the RAIN code to estimate effective average rain rates versus RAF for our simulated storms, to interpret average rain rates in terms of the local climatic data to infer probabilities of occurrence for given rainout situations.

A. Rainout Effects versus Rain Area Fraction.

We again use our "standard" 10-shot scenario to estimate rainout effects for 0.4-kt and 1-kt salvos. (Higher yields will be examined in the next section.) These results are presented as a function of input RAF (to TEMPEST). Actual rain area fraction is, of course, a time-dependent, statistically-varying quantity throughout any TEMPEST-SCAVDEN simulation. Table IV gives the input and actual rain area fractions for the present calculations.

Figures 34 and 35 show rainout effects for 0.4-kt salvos when input RAFs are varied between 0.1 and 0.4 and between 0.015 and 0.2, respectively. Figure 34 exhibits a lack of sensitivity to RAF for values above ~0.2; the 0.2-0.4 RAFs correspond to a more than threefold variation in average rain rate, but the rainout-effects curves are all very similar (except for about a threefold variation in IWBD for a single population point ~0.2 h downwind from the shot

TABLE IV

RAF INPUT VALUES, ACTUAL RANGES, AND CORRESPONDING APPROXIMATE EFFECTIVE VALUES ($\overline{RAF}$) FOR "PRODUCTION" RAINOUT RUNS

Input RAF	Range of Actual RAFs for Production Runs	Approximate Average ($\overline{RAF}$)
0.010	0.009 to 0.012	0.011
0.015	0.015 to 0.021	0.019
0.03	0.029 to 0.031	0.030
0.05	0.05 to 0.053	0.051
0.10	0.12 to 0.13	0.12
0.20	0.22 to 0.23	0.23
0.30	0.34 to 0.35	0.35
0.40	0.45 to 0.47	0.45

line). Rainout effects are somewhat lower when RAF = 0.05-0.1 and are falling off rapidly when RAF = 0.015.

Figures 36 and 37 show analogous results for 1-kt salvos. The variation of these results with RAF is similar to that for 0.4 kt, although the rate of falloff at lower RAF values is slower.

These same trends can be seen more clearly in Table V, which lists, for the calculations depicted in Figs. 34-37, the number of population points affected at various IWBD levels. (The number of affected points is not a direct measure of collateral damage but is still a useful measure for identifying such comparative trends because it is not subject to the population-weighting fluctuations that are present in the final effects estimates.) The data in Table V also suggest a broad maximum in rainout effects versus RAF at RAF = $\sim$0.1-0.2, for IWBD of $\sim$100 rem and larger. This maximum is real, but it is masked in Figs. 34-37 by the point-to-point variations in population weighting factors that ACRA attaches to the points of Table V to get the effects data in Figs. 34-37.

The dependence of rainout effects on RAF seen in Figs. 34-37 and Table V is directly related to how debris-cloud sizes compare with distances between rain cells. Cloud size is essentially independent of RAF but does depend on

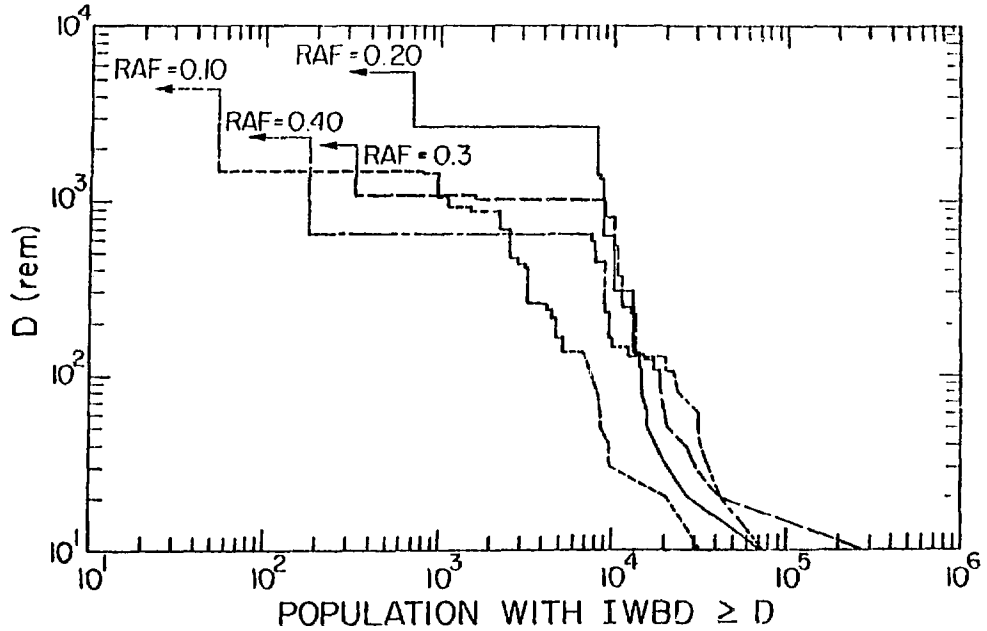

Fig. 34.
Effect on rainout results of varying input rain area fraction RAF; ten 0.4-kt shots.

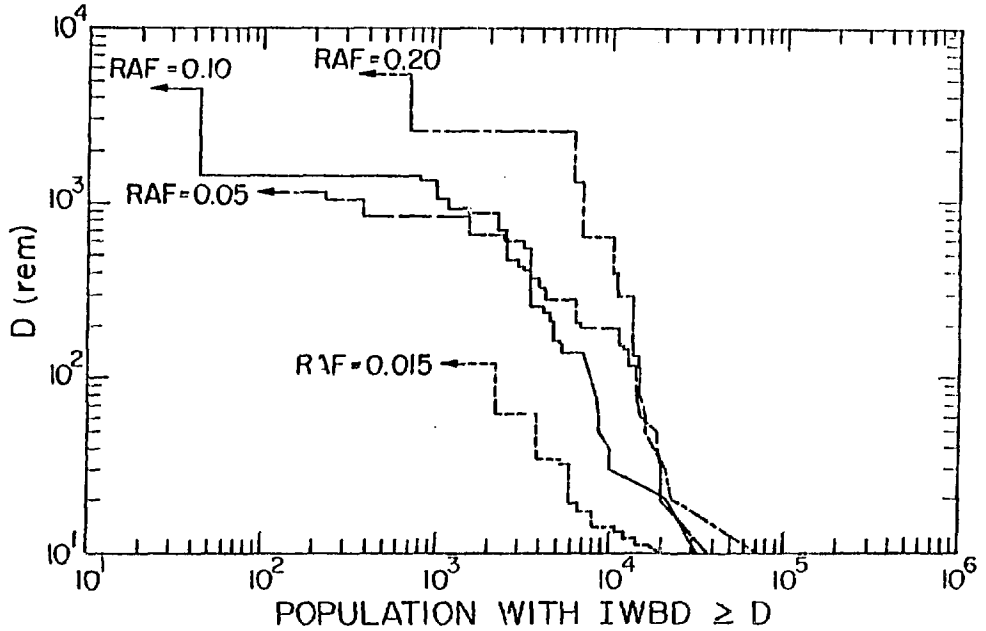

Fig. 35.
Effect on rainout results of varying input rain area fraction RAF; ten 0.4-kt shots.

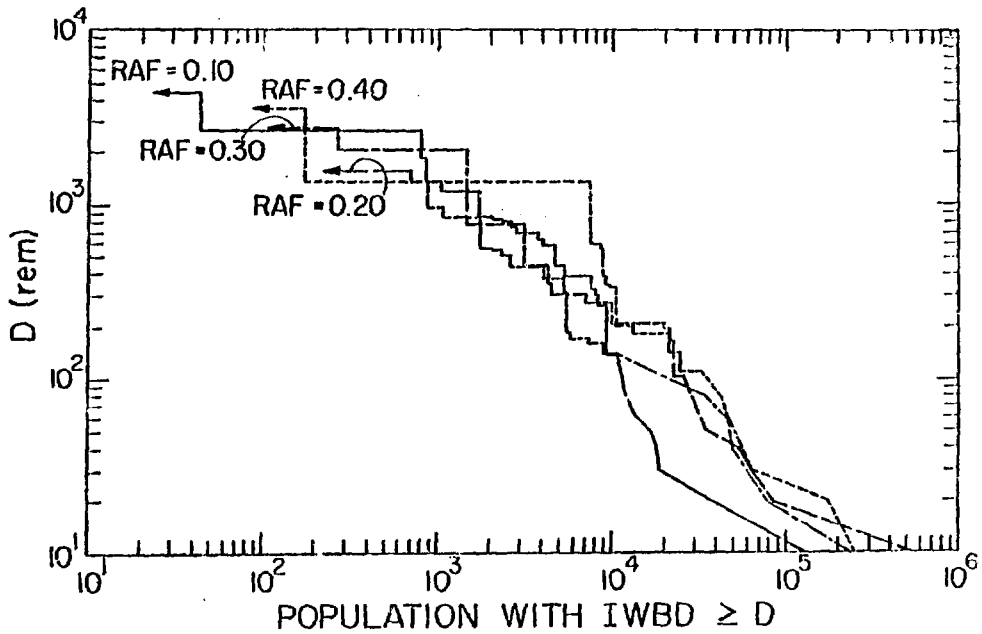

Fig. 36.
Effect on rainout results of varying input rain area fraction RAF; ten 1-kt shots.

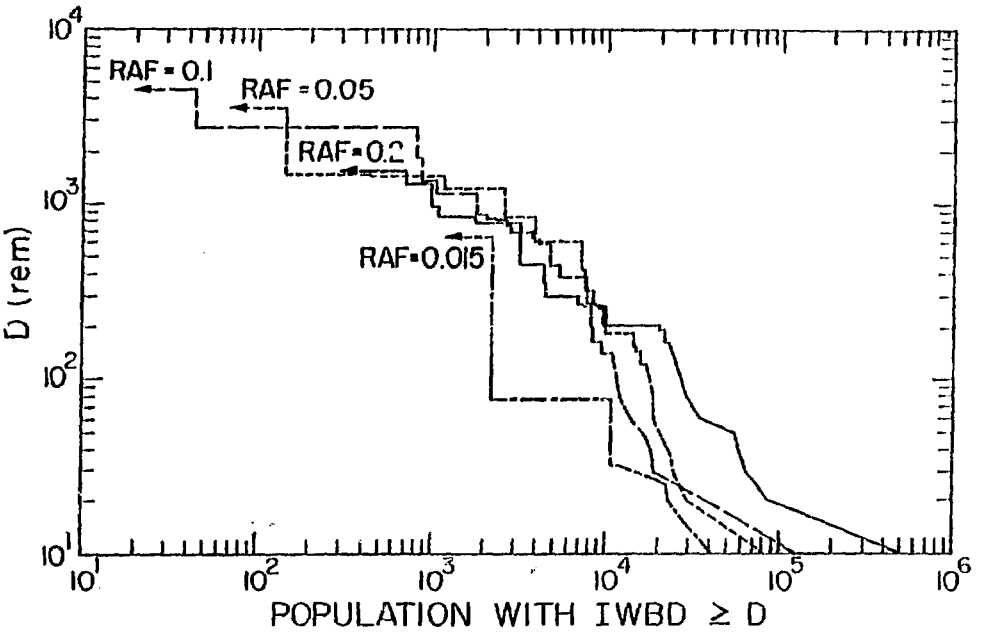

Fig. 37.
Effect on rainout results of varying input rain area fraction RAF; ten 1-kt shots.

TABLE V

NUMBER OF POPULATION POINTS WHERE IWBD EQUALS OR EXCEEDS D_c VALUES FOR LISTED RAFs, FOR 10-SHOT SALVOS OF FIGS. 34-37

(0.4-kt SHOTS)

	D_c (rem)						
RAF	10	50	100	200	450	1000	2000
0.015	18	2	1	0	0	0	0
0.05	49	26	19	10	6	2	0
0.1	49	21	18	14	8	4	1
0.2	54	13	11	9	5	4	2
0.3	59	23	16	10	6	3	1
0.4	78	27	14	6	3	1	1

(1-kt SHOTS)

	D_c (rem)						
RAF	10	50	100	200	450	1000	2000
0.01	25	9	4	0	0	0	0
0.015	37	2	1	1	1	0	0
0.03	23	12	8	4	3	1	0
0.05	99	33	27	19	8	5	1
0.1	85	34	25	20	14	5	2
0.2	150	42	22	12	6	2	0
0.3	147	36	19	10	6	2	2
0.4	174	44	29	16	5	2	1

yield, especially at early times, and increases rapidly with time; cell separation distance changes inversely with RAF and is essentially independent of time. Two characteristically different relative-size regimes thus result, with distinctively different dependences of rainout deposition on RAF.

For RAF $\gtrsim$0.1 and yields $\gtrsim$1 kt, cell separation distances tend, on the average, to be significantly less than debris-cloud dimensions; and a debris cloud continually intercepts rain cells at a relatively high rate, so it "sees" a set of cells at all times that fairly well represents the overall rain-cell field. (In other words, the cloud is big enough to encompass a statistically

meaningful sample of cells from the large-scale field.) In this event, the properties of the ensemble of cells acting on the debris cloud will be statistically "well behaved" (modest fluctuations) as functions of time and will vary with RAF in roughly the same way as the large-scale field. Because deposition depends on cell intensity R only through the scavenging coefficient $\lambda = KR^{0.8}$, the RAF-dependent variations in the R of the intercepted cells are exactly equivalent to corresponding variations in λ; and the resultant dependence of deposition on λ (and, hence, on RAF) is weak (Secs. VIII-A-4 and VIII-B-2).

For RAF $\lesssim$0.05 and for lower yields, an early period exists during which rain-cell separation distances are larger than debris-cloud sizes and substantial cloud dispersal takes place on the average before any rain cells are intercepted. Deposition thus begins at later times for lower RAFs because the cell separation distances are greater and because more time is required for the cloud to grow to a comparable size. Also, for smaller RAFs, the initial deposition rate is statistically more variable; and depletion, when it begins, is at a lower rate because of the lower average rain rate and the larger average cloud size at the onset of deposition. The net result with lower RAF is a rapid falloff of early-time deposition rates and an extension of the threat lifetime and, hence, of the distance and number of people threatened at lower IWBD.

Figures 34-37 and plots of IWBD versus distance show these characteristic features for those population points affected by rainout (analogous to Fig. 11). Figures 38-40* show examples of such plots for the 0.4-kt salvos; note the differences in the maximum "envelopes." Figure 41 shows analogous envelopes for the 1-kt salvos.

B. Rainout Effects versus Yield.

Figures 42 and 43 show rainout effects versus shot yield for "standard" 10-shot salvos in a rain field with RAF = 0.10, and Figs. 44 and 45 give analogous results for a rain field with RAF = 0.015. Table VI gives corresponding numbers of rainout-affected population points versus yield and IWBD.

---

*In these figures, we plot IWBD versus distance from shot 2 for all points with IWBD $\geq$ 10 rem.

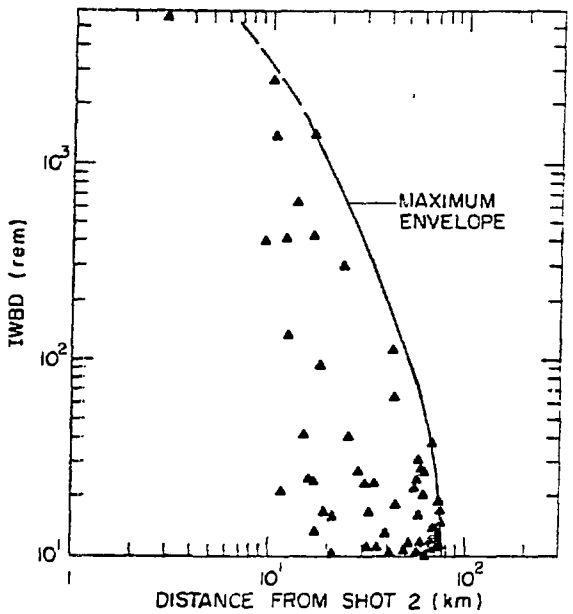

Fig. 38.
Dose vs distance for ten 0.4-kt shots with RAF = 0.2.

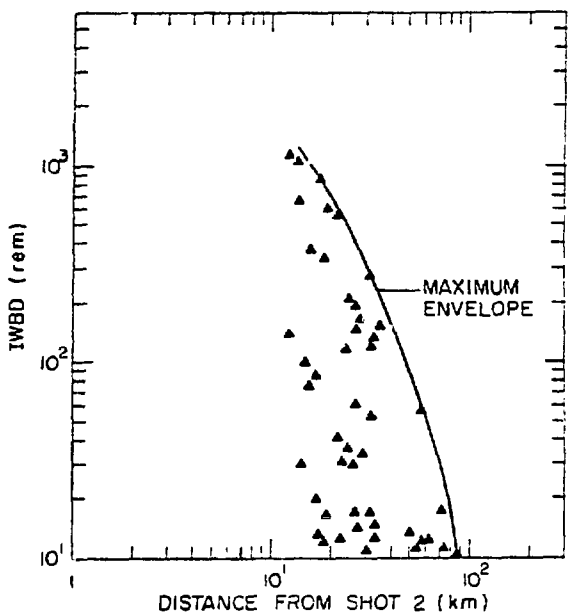

Fig. 39.
Dose vs distance for ten 0.4-kt shots with RAF = 0.05.

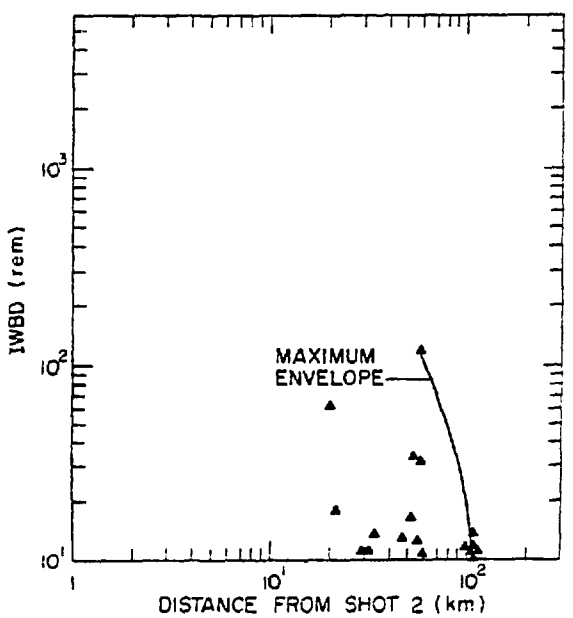

Fig. 40.
Dose vs distance for ten 0.4-kt shots with RAF = 0.01.

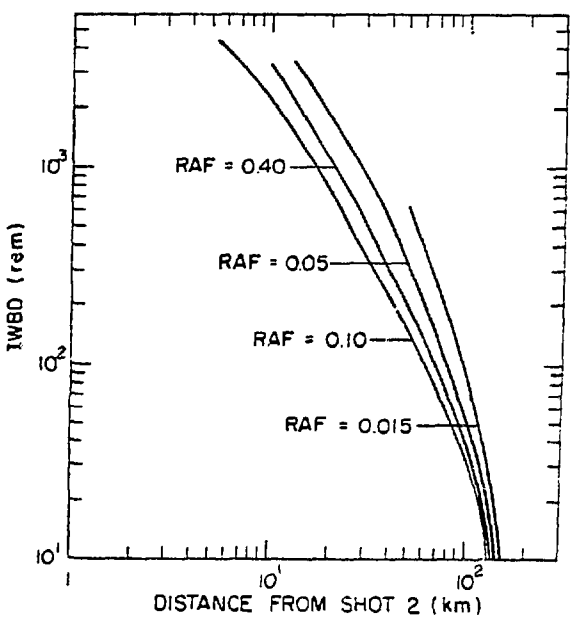

Fig. 41.
Maximum dose-vs-distance envelopes for ten 1-kt shots with various RAF.

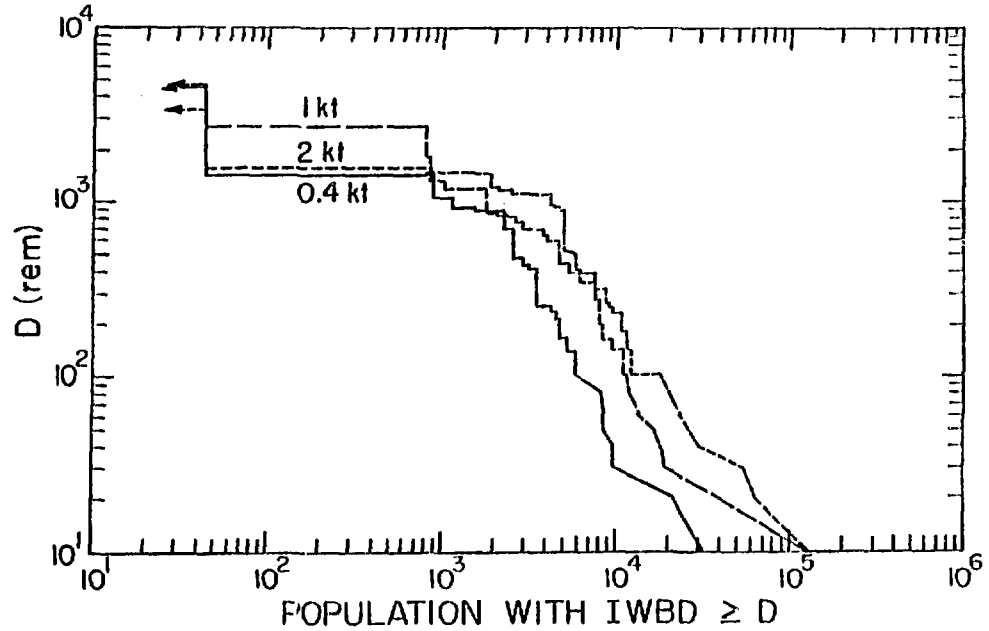

Fig. 42.
Effect on rainout results of varying shot yield; ten-shot salvos with RAF = 0.10.

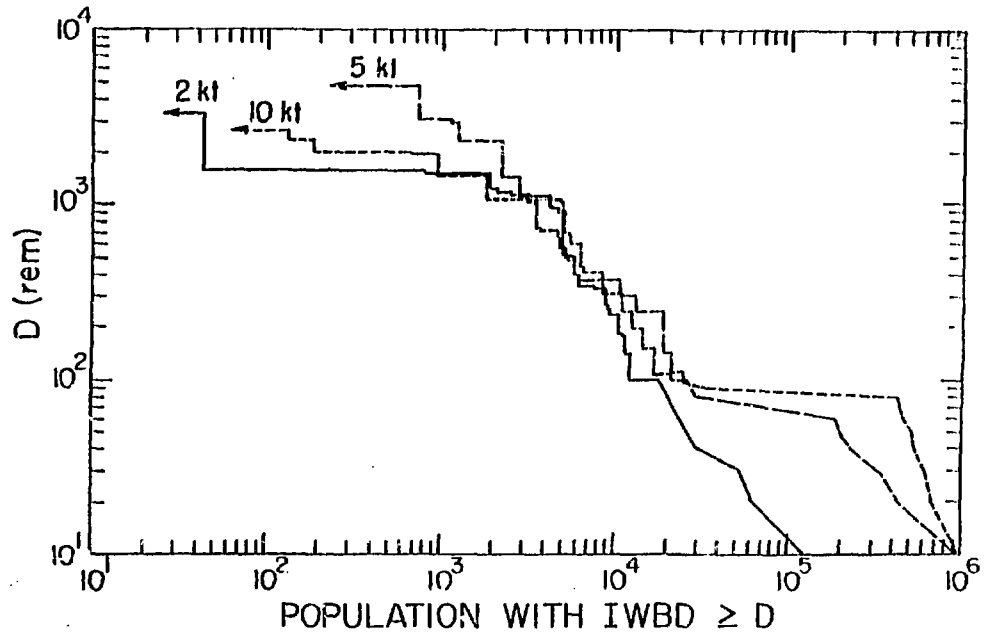

Fig. 43.
Effect on rainout results of varying shot yield; ten-shot salvos with RAF = 0.10.

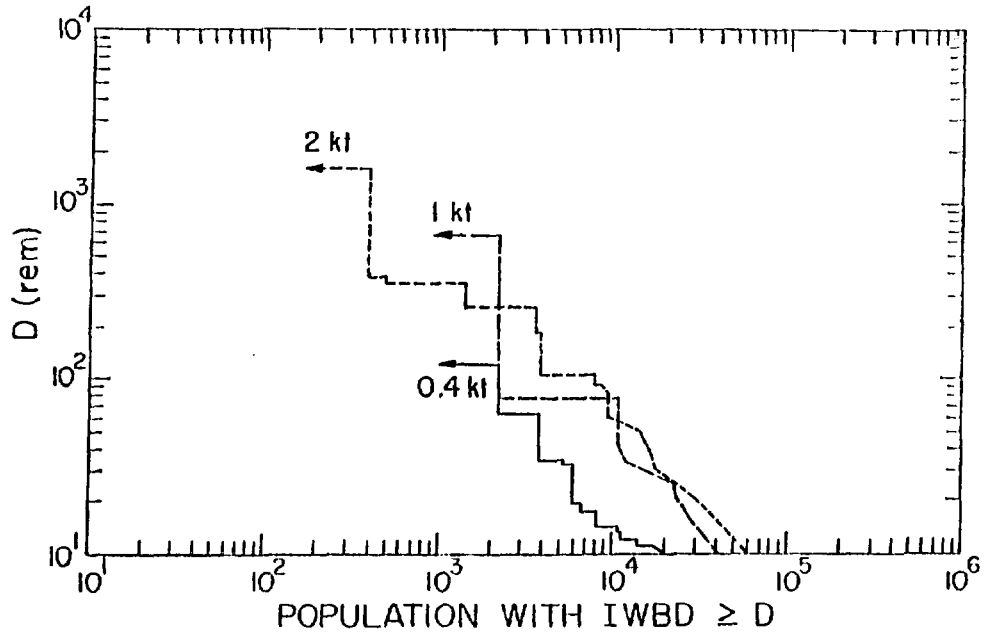

Fig. 44.
Effect on rainout results of varying shot yield; ten-shot salvos with RAF = 0.015.

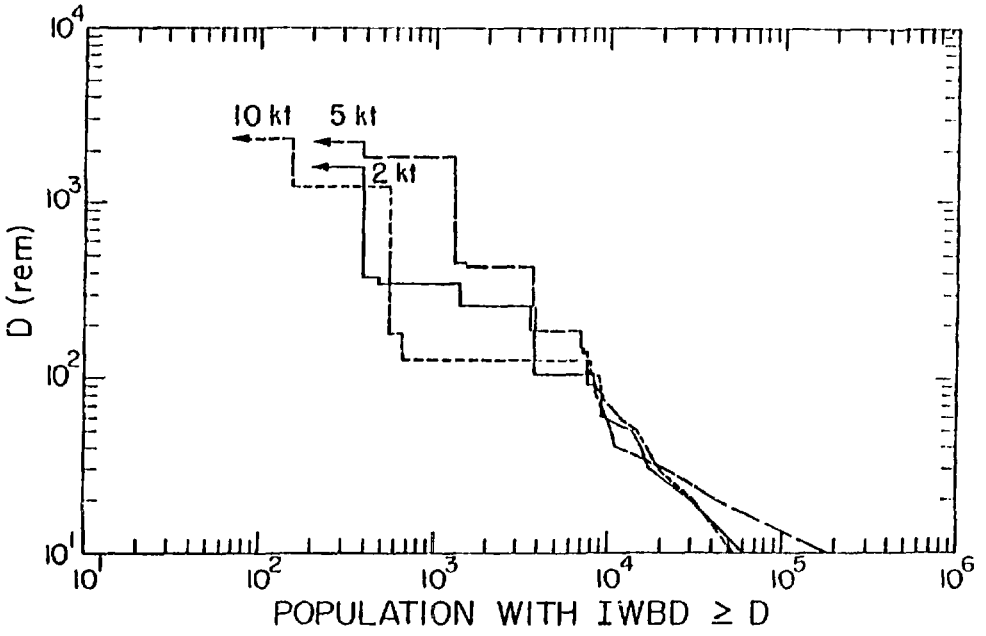

Fig. 45.
Effect on rainout results of varying shot yield; ten-shot salvos with RAF = 0.015.

TABLE VI

NUMBER OF POPULATION POINTS WHERE IWBD EQUALS OR EXCEEDS INDICATED D_c VALUES FOR LISTED YIELDS (FOR 10-SHOT SALVOS OF FIGS. 42-45).

(RAF = 0.10)

YIELD	D_c (rem)						
(kt)	10	50	100	200	450	1000	2000
0.4	49	21	18	14	8	4	1
1	85	34	25	20	14	5	2
2	177	47	36	22	15	8	1
5	536	78	43	29	17	9	5
10	302	104	49	31	14	7	3

(RAF = 0.015)

YIELD	D_c (rem)						
(kt)	10	50	100	200	450	1000	2000
0.4	18	2	1	0	0	0	0
1	37	2	1	1	1	0	0
2	107	14	7	4	1	1	0
5	93	14	9	5	2	2	1
10	43	13	5	2	2	2	1

The primary tradeoffs that determine how rainout effects vary with increased yield are between (1) decreased scavenging probability arising from increased debris altitude and (2) increased debris concentration and debris-cloud size. The net result is a yield dependence of rainout effects that is qualitatively similar to the RAF dependence discussed in the previous section.

The results in Figs. 42-45 and in Table VI show that rainout effects have a broad maximum at yields of ∿2-5 kt (particularly at higher IWBD) and a relatively rapid falloff below ∿1 kt (especially at lower IWBD). Rainout effects are also decreasing at ∿10 kt and will do so rapidly for higher yields (Sec. VIII-A-4).

An important yield-dependent factor is evident in the maximum-threat-distance envelopes of Fig. 46. Primarily because of the larger fission-product

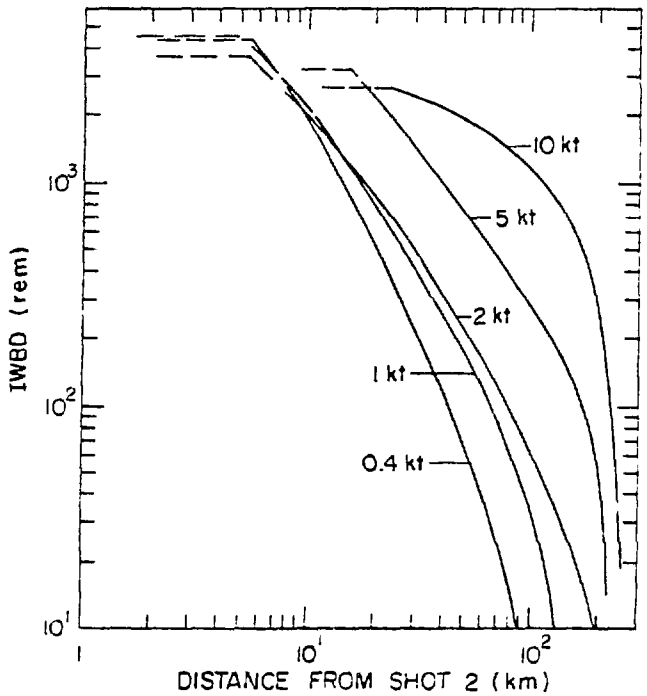

Fig. 46.
Maximum dose-vs-distance envelopes for ten-shot salvos with RAF = 0.10.

inventory, higher yield means longer threat lifetime at a given IWBD and, thus, a larger maximum threat distance, r_{max}. The higher wind speeds generally found at the higher altitudes associated with higher-yield weapons also increase the threat distance. Table VII and Fig. 47 show estimated r_{max} vs yield for various IWBD levels. Table VII also lists $\bar{v}$, the average velocity of the debris-cloud centroid in the calculations, and the quantity $r_{max}/\bar{v}$, which gives an approximate measure of threat lifetime.

C. Normalization to German Rain Data

In this section, we use west German rain data to estimate probabilities that the rainout events depicted in Figs. 34-47 will occur. We chose annual precipitation data here and estimated probabilities over a typical 1-yr period, although we could just as well have used seasonal data to estimate seasonal probabilities.

TABLE VII

MAXIMUM THREAT DISTANCE, r_{max}, AND AVERAGE DEBRIS-CLOUD CENTROID VELOCITY, $\bar{v}$, VS YIELD FOR 10-SHOT SALVOS WITH RAF = 0.10

		IWBD = 10 rem		IWBD = 100 rem	
YIELD (kt)	$\bar{v}$ (km/h)	r_{max} (km)	$r_{max}/\bar{v}$ (h)	r_{max} (km)	$r_{max}/\bar{v}$ (h)
0.4	31	89	2.9	43	1.4
1	35	130	3.9	66	1.9
2	39	190	4.9	78	2.0
5	47	225	4.8	170	3.6
10	55	255	4.6	220	4.0

IWBD = 200 rem		IWBD = 450 rem		IWBD = 1000 rem	
r_{max} (km)	$r_{max}/\bar{v}$ (h)	r_{max} (km)	$r_{max}/\bar{v}$ (h)	r_{max} (km)	$r_{max}/\bar{v}$ (h)
32	1.0	22	0.7	14	0.5
46	1.3	28	0.8	17	0.5
54	1.4	32	0.8	18	0.5
120	2.6	72	1.5	39	0.8
210	3.8	170	3.1	115	2.1

Figure G-3 of Appendix G gives the climate-based conditional PDF for the TEMPEST variable RAF,* given that a precipitating storm system is in the area such that $R_6 \neq 0$, where R_6 is the 6-h precipitation accumulation. The condition $R_6 \neq 0$, is equivalent to the condition RAF $\neq 0$, so we can write

*The large uncertainties in Fig. G-3 stem directly from the RAIN calculations of Fig. G-2 and will carry over directly into the final probability estimates. These uncertainties are not just a result of poor statistics in the RAIN calculations; they are of more basic import. The statistical uncertainties in Fig. G-2 derive primarily from local inhomogeneities in the TEMPEST-SCAWDEN rain field, on the spatial and time scales of the debris-cloud threats. Such large local variations occur in nature, and this fact injects a fundamental uncertainty element into any attempt to estimate, or even define, useful "occurrence probabilities" for rainout effects on the time and space scales pertinent to a specific tactical nuclear engagement. As we shall see, however, occurrence probabilities can still be bounded effectively.

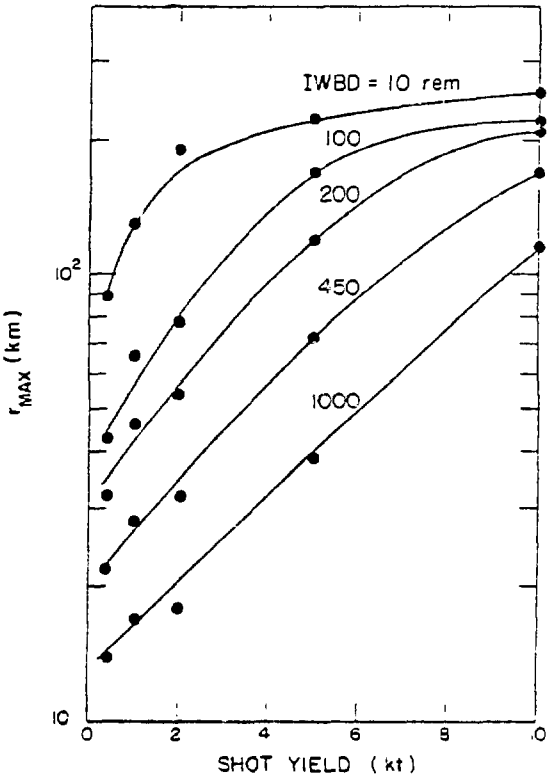

Fig. 47.
Maximum threat distance r_{max} vs shot yield; ten-shot salvos with RAF = 0.10.

$$P_1 = P(\overline{RAF} \geq RAF_o / \overline{RAF} \neq 0)$$
$$= \text{probability that } \overline{RAF} \geq RAF_o, \text{ given that } \overline{RAF} \neq 0$$
$$= 1 - P(\overline{RAF} \leq RAF_o / R_6 \neq 0),$$

where $P(\overline{RAF} \leq RAF_o/R_6 \neq 0)$ is taken from Fig. G-3. Table VIII lists selected values of P_1.

TABLE VIII

RAF_o	P_1 (Nominal)	Uncertainty Bounds on P_1
0.015	0.97	0.92-1.00
0.03	0.89	0.76-0.98
0.05	0.75	0.56-0.94
0.1	0.46	0.25-0.68
0.2	0.16	0.06-0.26
0.3	0.04	0.02-0.08
0.4	<0.01	-

We need another type of climatic date, the probability that RAF $\neq$ 0, to get overall probability of occurrence. Figure 48, a composite graph of West German data, shows the fraction of observation periods throughout the year that have observable precipitation versus length of the observation period. We used two different sources[9,10] to get 1-, 6-, and 24-h observation times. The plotted points reflect different stations available from each source and include stations in the Alps as well as in lowland and coastal sites. The "nominal" line appears adequate to represent the region of interest, with an uncertainty spread of perhaps $\pm$0.05 for times pertinent to our rainout scenarios (1-6 h).

We can use Fig. 48 to estimate probabilities of observable precipitation for different observation periods and thus make some allowance for the fact that the relevant "observation" period varies with yield and with IWBD (Table VII).* We define $P_2 = P(R_T \neq 0)$ = probability that observable precipitation occurs during time T, and use Fig. 48 to estimate the following:

*We should, in principle, also use different $\overline{RAF}$ PDFs (Fig. G-3) for different yields and different IWBDs. Such detail is presently not justified by the available data, however, so we used the 6-h PDF throughout our work; this gives somewhat conservative (high) probability estimates for our rainout events, which generally occur over times smaller than 6 h.

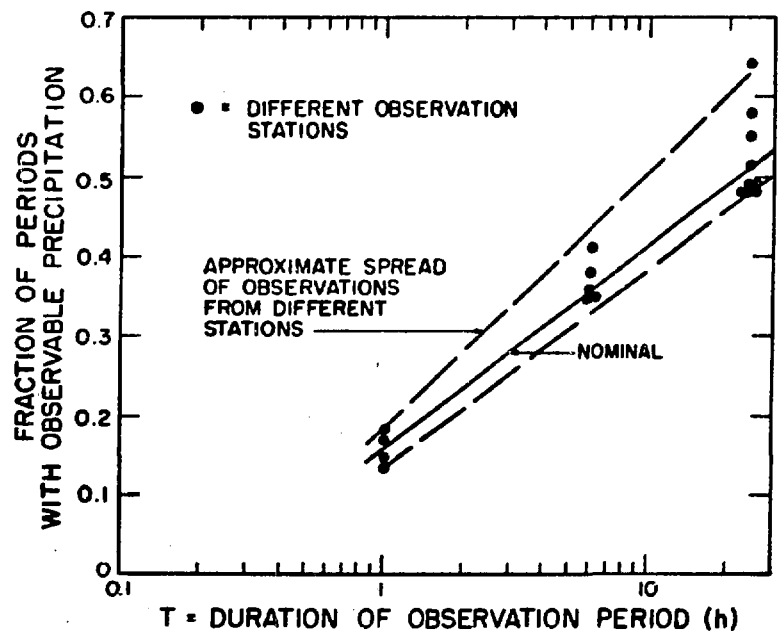

Fig. 48.
Estimated probability that $R_T \neq 0$ vs observation time T; German climate.

T(h)	P_2
1	0.16 ± 0.03
2	0.24 ± 0.03
3	0.28 ± 0.04
4	0.32 ± 0.04
5	0.34 ± 0.05
6	0.36 ± 0.05

The overall probability that $\overline{RAF} \neq 0$ during time T and that $\overline{RAF} \geq RAF_o$ is then the product P_T of P_1 (Table VIII) and P_2:

$$P_T = P(\overline{RAF} \geq RAF_o,\ R_T \neq 0) = P_1 P_2.$$

Table IX and Fig. 49 show the resulting P_T; Table X and Fig. 50 give the corresponding P_T range of uncertainty.

Finally, we can identify the various scenarios (of Figs. 34-47) in terms of the probabilities in Tables IX and X (Figs. 49 and 50) by using Table VII, in conjunction with deposition-time information tabulated by ACRA, to estimate (conservative) maximum threat times of interest. Table XI lists these times.

TABLE IX

ESTIMATED PROBABILITY THAT RAF ≠ 0 DURING THREAT TIME T AND THAT $\overline{RAF} \geq RAF_o$

	$P_T = P_1 P_2$					
RAF_o	T = 1h	2h	3h	4h	5h	6h
0.015	0.16	0.23	0.27	0.31	0.33	0.35
0.03	0.14	0.21	0.25	0.28	0.30	0.32
0.05	0.12	0.18	0.21	0.24	0.26	0.27
0.1	0.074	0.11	0.13	0.15	0.16	0.17
0.2	0.026	0.038	0.045	0.051	0.054	0.058
0.3	0.0064	0.0096	0.011	0.013	0.014	0.014
0.4	<0.0016	<0.0024	<0.0028	<0.0032	<0.0034	<0.0036

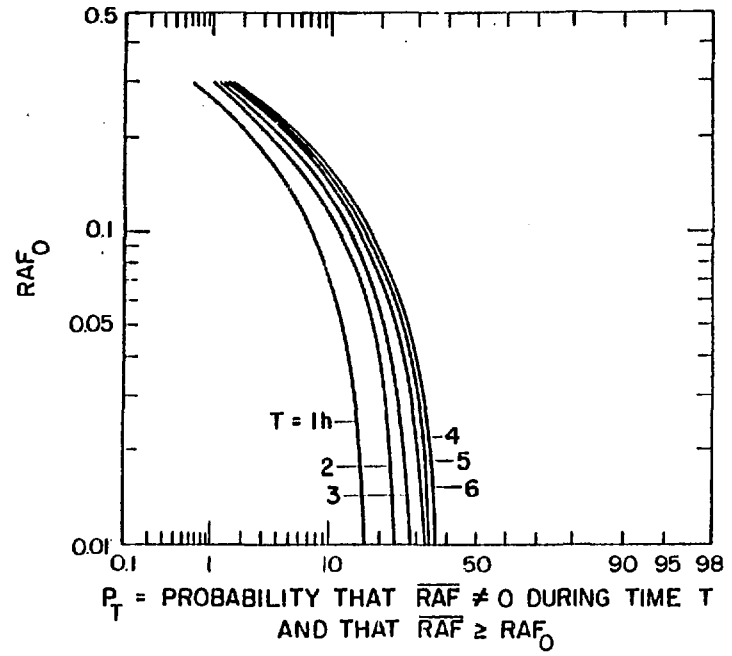

Fig. 49.
Estimated occurrence probabilities for indicated storm and precipitation conditions.

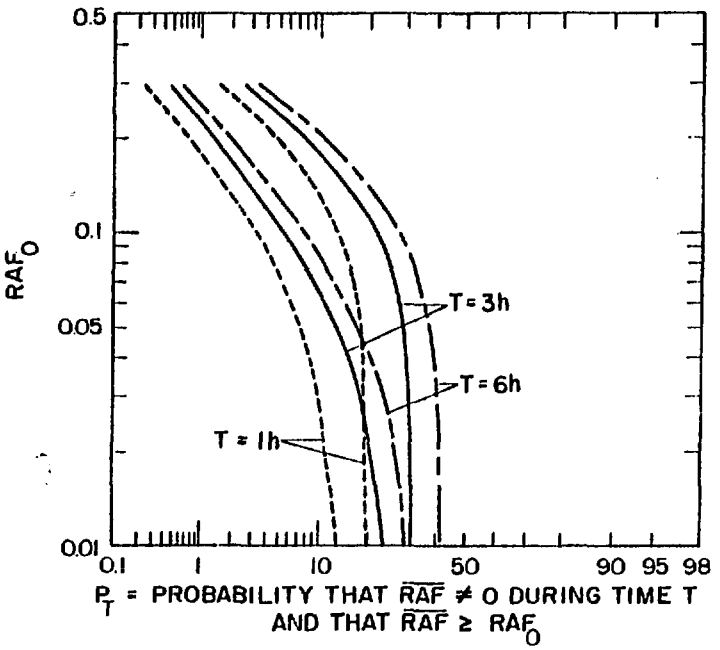

Fig. 50.
Uncertainty bounds of occurrence probabilities for indicated storm and precipitation conditions.

TABLE X

UNCERTAINTY BOUNDS FOR PROBABILITY THAT $\overline{RAF} \neq 0$ DURING THREAT TIME T AND THAT $\overline{RAF} \geq RAF_o$.

Uncertainty Bounds for P_T

RAF_o	T_1 = 1h	2h	3h	4h	5h	6h
0.015	0.12 - 0.19	0.19 - 0.27	0.22 - 0.32	0.26 - 0.36	0.27 - 0.39	0.29 - 0.41
0.03	0.099 - 0.19	0.16 - 0.26	0.18 - 0.31	0.21 - 0.35	0.22 - 0.38	0.24 - 0.40
0.05	0.073 - 0.18	0.12 - 0.25	0.13 - 0.30	0.16 - 0.34	0.16 - 0.37	0.17 - 0.39
0.1	0.033 - 0.13	0.053 - 0.18	0.060 - 0.22	0.070 - 0.24	0.073 - 0.27	0.078 - 0.28
0.2	0.0078 - 0.049	0.013 - 0.070	0.014 - 0.083	0.017 - 0.094	0.017 - 0.10	0.019 - 0.11
0.3	0.0026 - 0.015	0.0042 - 0.022	0.0048 - 0.026	0.0056 - 0.029	0.058 - 0.031	0.0062 - 0.033

TABLE XI

MAXIMUM THREAT-TIME BOUNDS T FOR 10-SHOT SALVOS OF FIGS. 34-47

Yield (kt)	T(h) IWBD $\geq$ 10 rem	100 rem	200 rem	450 rem	1000 rem
0.4	3	2	1	1	1
1	4	2	2	1	1
2	5	3	2	1	1
5	5	4	3	2	2
10	6	5	4	4	3

To summarize, we use Table XI to estimate the appropriate "observation" time T for a standard 10-shot salvo with given shot yield and for a given IWBD threshold. This T then identifies the appropriate P_T in Tables IX and X (Figs. 49 and 50) that applies to the given case.

Despite the large uncertainty bounds on P_T, Tables IX-XI and Figs. 49 and 50 give probability information of direct value for assessing rainout threats. For example, the probability of any rainout threat from local rain fields, for our calculated scenarios, ranges from 10-20% at yields below ~1 kt and IWBDs

$\gtrsim$200 rem to a maximum of ~30-40% for yields $\gtrsim$2 kt and IWBDs $\gtrsim$10 rem. Also, $\overline{RAF}$s larger than those we calculated (0.45) are unlikely in the German climate. The worst-case rainout situations (highest occurrence probability and largest rainout effects) are those with $\overline{RAF}$ between ~0.05 and 0.2 ($R_6 \approx$ 0.1-1 mm/h), and this maximum is very broad. The rainout threat falls off rapidly at higher $\overline{RAF}$s because of decreasing probability of occurrence and falls off rapidly at lower $\overline{RAF}$s because of decreasing average rainout doses. These are fundamental features of rainout that will also apply to other scenarios.

Table XII shows $\overline{RAF}$ and R_6 for three different rain-field regimes. Table XIII lists some representative, specific, rainout-effects data from our calculated scenarios for the three regimes shown in Table XII, to illustrate different types of "casualty" information available from our results. XIII gives conservative estimates for the number of people N with IWBD $\geq D_c$ and associated occurrence probabilities for the 1-kt and 0.4-kt salvos of Figs. 34-41.

D. Comparisons with Surface-Burst Fallout and Prompt Collateral-Damage Effects.

Results presented in the previous sections show that casualties could occur from the postulated scenarios, and that although occurrence probabilities in the west German climate are not large they are not negligible. The actual number of people threatened with "damaging" doses in these engagements would depend on the level of radiation dose assumed to be damaging, but tens of thousands of people could be involved at levels of ~100 rem and higher.

In an actual engagement, the number of people that would receive rainout doses at such levels would be much smaller than our results indicate because of shielding and postdeposition protective factors (Sec. V). Furthermore, even if we had made less conservative estimates for rainout "casualties," the assessment of their significance in actual operational contexts would be a

TABLE XII

THREE RAIN-FIELD REGIMES

Qualitative Description	$\overline{RAF}$	6-h Average Rain-Rate R_6 (mm/h)
Light	<0.03	<0.1
Medium	0.03 to 0.2	0.1 to 1
Heavy	>0.2	>1

TABLE XIII

NUMBER OF PEOPLE N WITH IWBD $\geq D_c$, AND ASSOCIATED OCCURRENCE PROBABILITY P, FOR SCENARIOS OF FIGS. 34-41

Shot Yield (kt)	D_c (rem)	P(N ≠ 0)	N_{max}	Light-Rain Field		Medium-Rain Field		Heavy-Rain Field	
				P	N	P	N	P	N
1	200	0.25 ± 0.03	20 000	0.04	<10 000	0.17	∿10 000	0.04	10 000 - 20 000
1	450	0.17 ± 0.03	9 000	0.03	<7 000	0.11	4 000 - 7 000	0.03	4 000 - 9 000
1	1 000	<0.17	7 500	<0.03	<3 000	<0.11	1 000 - 2 500	<0.03	1 000 - 7 500
0.4	200	0.17 ± 0.03	14 000	0.03	<4 5000	0.11	4 500 - 13 000	0.03	4 500 - 14 000
0.4	450	<0.17	11 000	<0.03	<3 500	<0.11	3 500 - 10 000	<0.03	3 000 - 11 000
0.4	1 000	<0.17	9 000	<0.03	<400	<0.11	400 - 7 000	<0.03	200 - 9 000

complex problem more appropriately handled by military scientists. We have thus made no attempt at such assessments here. We can provide some useful insight into the relative magnitudes of these rainout threats, however, by comparing them with corresponding fallout and prompt effects for the same scenarios.

Fallout, prompt effects, and rainout effects for 10-shot salvos are compared in Figs. 51-54 for shot yields of 0.4, 1, 5, and 10 kt, respectively. These rainout scenarios are our standard airburst salvos (Sec. X), with RAFs of 0.1 and 0.015; the fallout and prompt results are for the same scenarios with all shots fired as surface bursts.* No shielding or postdeposition factors are in any of these calculations.

Rainout effects compare least favorably for shot yields of ∿1 kt and less, where fallout effects are smallest, and at IWBDs ≳100 rem. In this regime, the worst rainout effects are higher than surface-burst fallout effects by a factor of 2 or less and are higher than the prompt effects** by a factor of 2 to 5. In real engagements, rainout "casualties" would compare more favorably than indicated because (1) rainout-specific, postdeposition, protective factors such as runoff, seepage, and avoidance possibilities would reduce real rainout doses as compared with real fallout and prompt doses, and (2) the probability of rainout (10-20%) is smaller than for fallout (100% for surface bursts) and for prompt effects (100% in all cases).

*The surface-burst calculations were made by LASL staff member T. W. Dowler with the LACOMP fallout code.

**Recall that prompt effects will also be present in the rainout (airburst) scenarios.

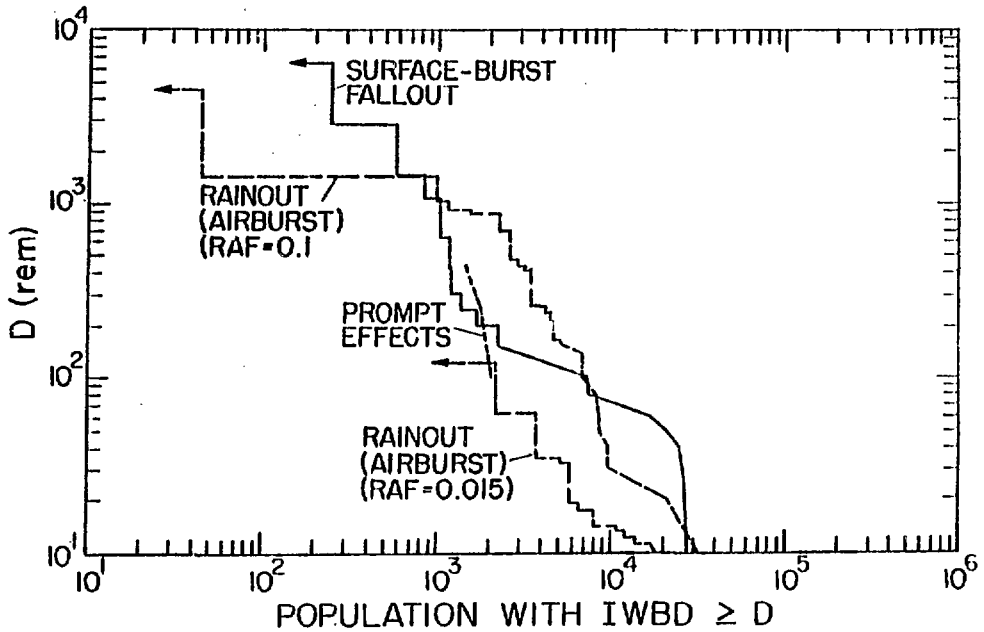

Fig. 51.
Comparisons of rainout effects to surface-burst fallout and to prompt effects; ten 0.4-kt shots.

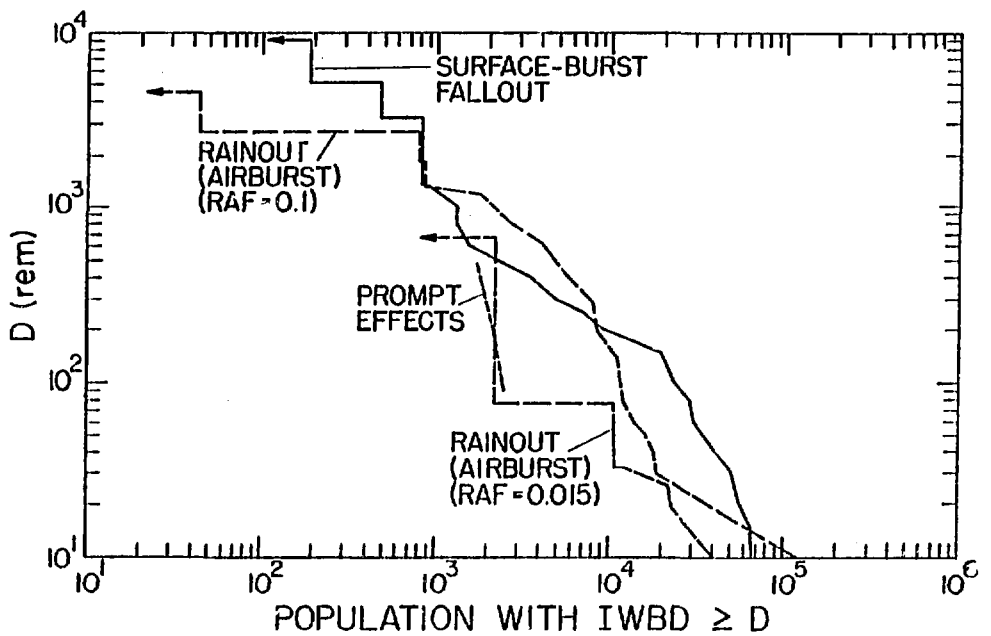

Fig. 52.
Comparisons of rainout effects to surface-burst fallout and to prompt effects; ten 1-kt shots.

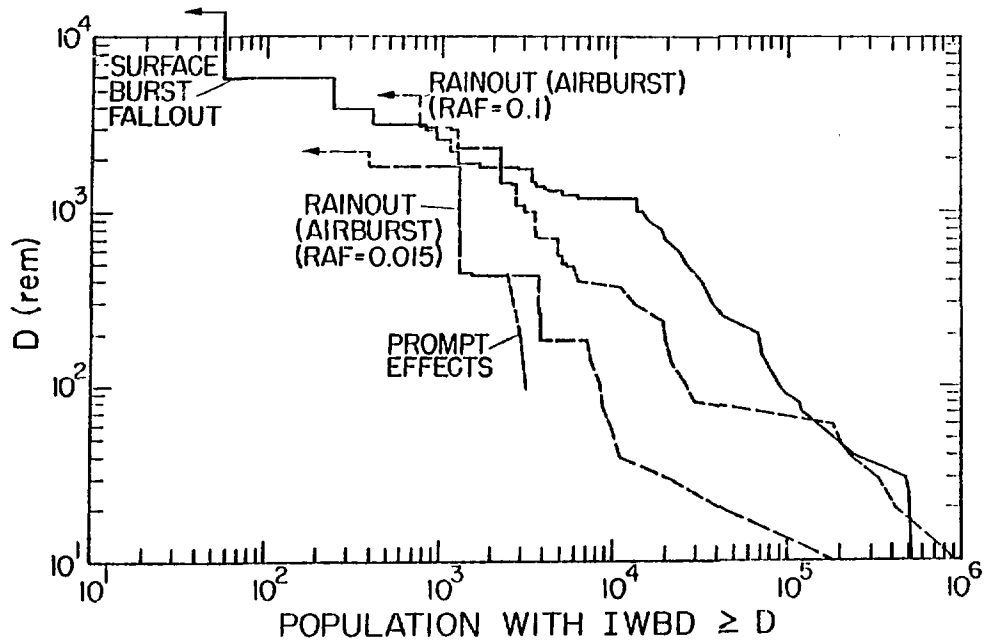

Fig. 53.
Comparisons of rainout effects to surface-burst fallout and to prompt effects; ten 5-kt shots.

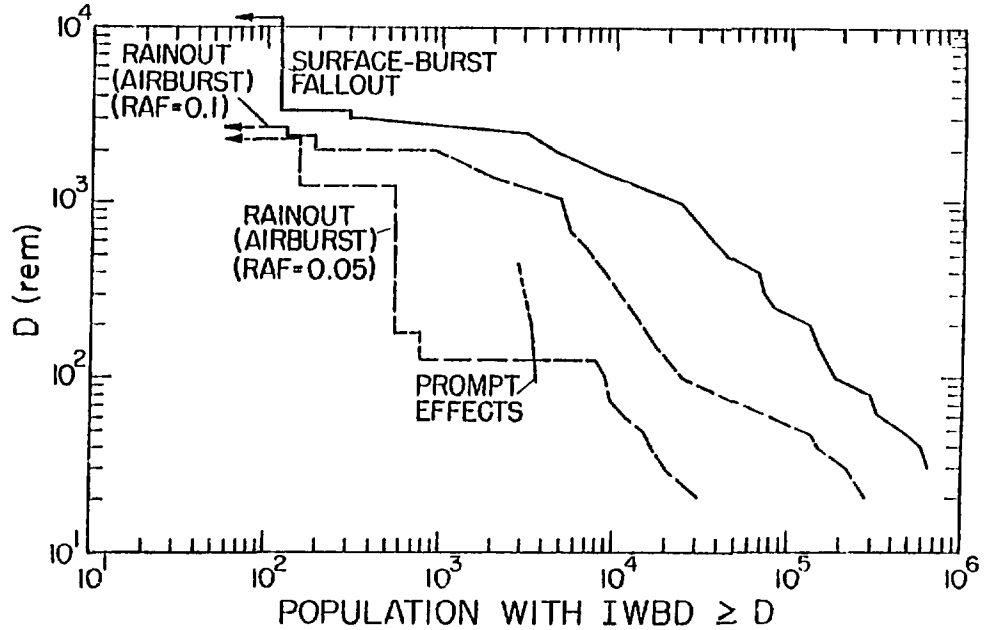

Fig. 54.
Comparisons of rainout effects to surface-burst fallout and to prompt effects; ten 10-kt shots

Fallout and prompt effects increase monotonically with shot yield, whereas rainout threats level off at shot yields of ∿2-5 kt and then begin to fall off (to zero) above ∿10 kt. Maximum potential rainout effects thus rapidly fall below fallout effects as shot yield increases above ∿1 kt, and they eventually fall below the level of prompt effects at shot yields somewhere above 10 kt. These features are seen in Figs. 51-54. In a "light" rain field, potential rainout effects for our 10-shot salvos are comparable to or less than the level of prompt effects (for IwBD $\geq$ ∿100 rem) for all shot yields.

X. GENERAL CONCLUSIONS

We have no "position" on the commonly asked question, "Is rainout important?" We believe the question is pointless unless the answer is an unequivocal "no," and such an answer is not possible. The only condition that would permit such an answer would occur if scavenging efficiencies for low-yield, airburst, nuclear debris were so low that only trivial amounts of debris could be brought down even in very heavy rain fields. This condition has not been proved as yet and may well never be.

We must therefore assume that precipitation scavenging of low-yield airburst debris is possible, and this means that significant local rainout radiation fields are an *a priori* possibility if a rain field is in the area. Because both the number and intensity of such "hot spots" will increase monotonically as the number of shots increases, dangerouus rainout areas on the ground will be inevitable if the rain field persists and the number of low-yield shots is large enough. In this event, some of these hot spots clearly could fall on nearby, downwind cities or friendly troops; and we would then have a potential for rainout "casualties."

The proper rainout "question" under these circumstances is then manifold and complex: (1) where, when, under what conditions, to what extent, and with what probabilities can rainout doses occur; (2) what are the driving physical elements, how do they affect the answers to the above questions, and how can such insight be used to ameliorate undesirable collateral-damage threats; and (3) what are the operational implications of the answers to all of the above questions in realistic military contexts, and does rainout raise important long-range issues that planners and decision makers should address.

We have dealt with questions (1) and (2) in this report. In the rest of this section we make generalized observations that summarize some of what we have learned about the magnitudes, sensitivities, and basic character of rainout threats. We also offer our present views on some long-range implications.

The most striking result of our studies is the consistent behavior of rainout effects as functions of the three driving independent variables: yield, average rain rate (RAF), and scavenging efficiency (measured by the parameter K). The dependence of rainout effects on each of these variables is shown in Fig. 55. These variables are independent in the sense that each of them produces the rainout behavior of Fig. 55 independently of the other two. Rainout threats are small, for example, if the yield, or the RAF, or the scavenging efficiency is small; furthermore, if any two of these variables have values that could produce substantial rainout, the dependence of rainout effects on the third variable is as shown in Fig. 55.

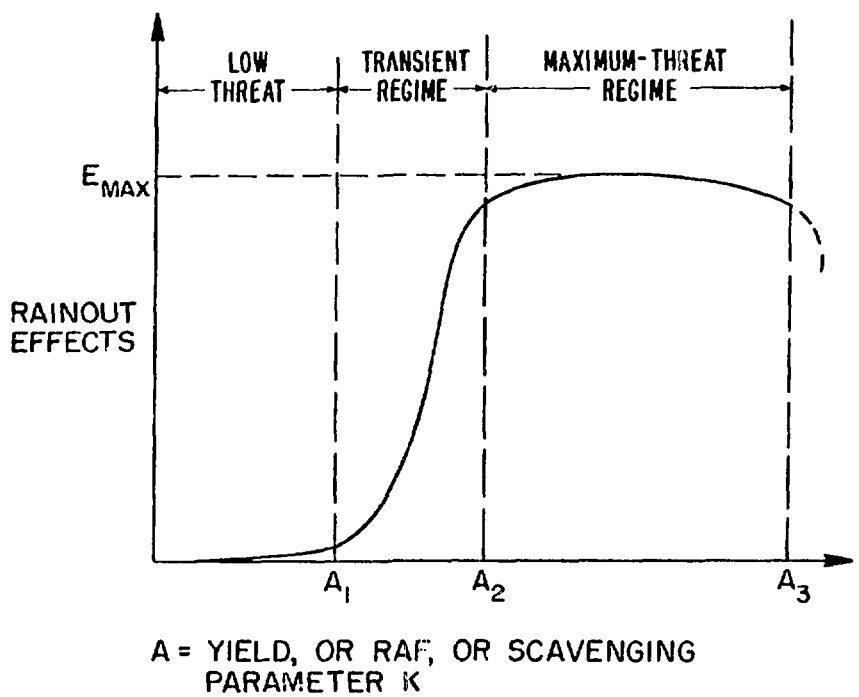

Fig. 55.
Rainout effects vs yield, RAF, or scavenging efficiency.

The important features illustrated in Fig. 55 are as follows.

1. There is a range of A between zero and a rough "threshold" (A_1) where rainout effects are innocuous because A is too small to support significant rainout threats.

2. In the transition regime between A_1 and A_2, rainout effects increase rapidly with increasing A as the intensity and extent of ground-deposited debris reaches significant levels.

3. There is a broad, shallow maximum in effects versus A over a large range of A; effects are relatively insensitive to A over this range because of complex tradeoffs among factors that tend to cancel one another.

4. A maximum threat level E_{max} can be identified within a factor of about 2 in our calculations.

5. There is a limiting value A_3 beyond which effects fall off rapidly to zero (for A = yield), or beyond which the values of A are no longer credible (for A = RAF) or are of no interest (for A = K).

6. Rainout effects decrease slowly from E_{max} as A approaches A_3.

Table XIV shows our current estimates of the three ranges in Fig. 55 for the three driving independent variables.

The existence of the broad maxima in rainout effects versus yield, RAF, and K (item 3) is the most important of these features. This behavior gives us confidence that the worst-case regimes have been adequately identified and that

TABLE XIV

ESTIMATED VALUES OF A_1, A_2, and A_3 IN FIG. 55
FOR THE DRIVING VARIABLES YIELD, RAF, AND K

Variable	A_1[a]	A_2	A_3
Yield (kt)	$\lesssim$0.1	0.4 to 1	$\sim$10 to 20
RAF	$\lesssim$0.01	0.05 to 0.1	0.4
K[b]	$\sim$0.05	0.5 to 1	30

[a] Rough guesses based on extrapolations of our results.

[b] Scavenging coefficient $\lambda(h^{-1})$ is $\lambda = KR^{0.8}$, where R = instantaneous rain rate in mm/h.

no special sensitivities have been overlooked that could lead to unpleasant surprises. The breadth and shallowness of the HAF and K threat regimes also mean that unpredictable fluctuations in local HAFs and uncertainties in scavenging efficiencies are relatively unimportant over broad ranges of values that are most important for rainout assessment. These are key points: they allow us to bound rainout threats and probabilities (as described earlier) usefully and with confidence.

A second generalized observation based on our results is that "fine" structure, or "local" details* in the time and space gradients of other physical variables are relatively unimportant, especially for multishot scenarios, provided certain integral conditions such as overall fission-product inventory and average rain rate remain essentially constant over the time and space regions of interest. Examples of such variables include the initial debris-cloud source distribution; the size distributions, the internal-intensity distributions, and the individual ground speeds of rain cells; and the local distribution of ground-deposited debris as affected by local transport features. Variations in overall, net rainout effects as functions of such details generally appear to be less than the scatter produced by inherent statistical fluctuations or by the heterogeneous population-weighting.

A third important class of generalized rainout behavior is the direct correlation between dose level and distance and direction from the shots, as illustrated in Figs. 8, 9, 11, 26, 38-41, 46, and 47. Large numbers of people can be threatened with high dose rates, but only if they are directly downwind from or relatively close to the engagement, and then only if a substantial rain field is in that same area at the same time as the debris clouds. These are conditions that should be predictable in a given conflict area for the pertinent few hours before and after an engagement.

Finally, we emphasize again that shielding and other postdeposition factors would generally reduce the rainout IWBDs calculated in this study, perhaps tenfold or more. Furthermore, simple protective responses, particularly if preplanned, would provide additional large reductions in IWBDs for affected people; such responses might include avoidance of precipitation

*By "fine" and "local" we mean of the same scale as debris or rain-cell sizes and threat lifetimes, and smaller.

accumulations, moving to protected places, or simply leaving the area of a rainout "hot spot." All these responses could be effective and would usually be feasible during the time required to accumulate large rainout doses. Specific operational considerations would also reduce rainout hazards; such considerations include city avoidance procedures, minimum total yield to do the job, and timely assessment of local wind and rain conditions. We believe that realistic inclusion of postdeposition factors, protective responses, and operational considerations would lead to the general conclusion that the scenarios calculated in our studies would not pose serious rainout problems.

In summary, rainout is real; it must be considered an integral part of nuclear-weapon effects studies just as any other delayed weapon effect. We believe debris from nuclear wars can be dangerous to nearby populations, even for airburst weapons; and to try to prove otherwise is futile unless unequivocal new evidence should somehow materialize to show that scavenging efficiencies are very low.

At the same time, we believe that the probability of producing large-scale rainout collateral-damage casualties is not large and that resultant effects, if they materialize, need not be prohibitive. Rainout does not rule out the effective use of small fission weapons in the airburst mode for defensive nuclear engagements. Rather, the airburst mode substitutes a low-probability threat of delayed effects for the certainty of delayed effects to be expected from other militarily equivalent modes; and rainout effects will generally be more innocuous if they occur. We expect that, if the character and magnitude of rainout threats are properly understood and are taken into account in realistic operational contexts, rainout damage may generally be within reasonable bounds. We believe the results of earlier studies raise an unnecessarily severe specter in this regard.

We emphasize, however, that we cannot be certain of this until more work is done (by the military community we hope) to define and evaluate conflict situations that provide the context within which rainout effects must be evaluated. Conflict scenarios, nuclear-weapon employment doctrine, and force deployment should be included. The next basic problem is to determine the effects of rainout on these elements. Until these effects are determined, the significance of rainout will remain in question.

APPENDIX A

MESOSCALE VARIABILITY OF PRECIPITATION

An important measure of uncertainty in precipitation scavenging is introduced through the variability of precipitation rates in time and space. In particular, when the variations are on a scale corresponding roughly to the size of a contaminant cloud subject to scavenging, the morphology of the contaminant-precipitation system becomes a dominant consideration. Two limiting ideal cases that can help in scoping the problem are (1) a small contaminant cloud embedded in a large, homogeneous rain shield and (2) the inverse, a small rain shower within a large contaminant cloud. Real situations, however, seldom present these simplified cases; and we must consider some concepts of interaction. The simplest useful interaction to study is the morphological intersection of rain and debris clouds. The results of this type of study must eventually be modulated by the dynamic interactions of entrainment and mixing within the circulation systems associated with precipitation.

For travel times of $\sim$1-10 h, dispersing clouds of atmospheric contaminant have horizontal areas of $\sim$1-1000 km^2. Cursory examination of precipitation patches shows that they cover $\sim$10-1000 km^2, so the debris and precipitation occupy areas of equivalent size, and, in estimating interactions, we must account for their respective geometries. Atmospheric structure on the scale of current interest is best investigated by means of weather satellites and radar, supplemented by *in situ* rain gauges to provide ground truth. Data collected by these observation tools have been examined in a number of studies. Although each study had different objectives, we can compile a composite summary of the mesoscale structure of precipitation in a "typical" occluding cyclone. With such a signature available, we can use traditional climate data such as storm tracks and precipitation records for individual stations to calibrate a statistical simulation technique and deduce time and space patterns for precipitation in a selected geographic region.

The picture that evolves is a multiscale structure with each scale exhibiting details on smaller scales, down to the basic unit of a precipitation cell. The major large-scale structure has been described by Boucher[11] and by Nagle and Serebreny.[12] From their discussions, it appears that the occluded

mid-latitude cyclone can be broken into four zones based on the character of precipitation, as follows.

1. Continuous stratiform precipitation in a broad shield ahead of a developing wave (generally north to northeast). This shield covers a zone of $\sim 10^4$ km^2 in which the precipitation is distributed in a banded structure covering 10-25% of the zone. The precipitation is shallow and rates are low, leading to inefficient wet deposition of suspended material. This category is marked by the least amount of definitive observational data. Not all storms contain an area of extensive uniform precipitation. Summer and early-fall systems will have convective clouds and precipitation in the northeast quadrant.

2. Ragged, patchy, stratiform precipitation in an area of 1000 km^2 close to the storm center in the forward quadrant. This zone tends to represent patches of heavier precipitation superposed on the lighter background rates. Again, $\sim$10% of the zone is involved in active precipitation, with $\sim$5% at rates exceeding 6 mm/h.

3. Frontal convective showers that are an integral part of mid-latitude cyclones. The frontal band during the active developing stage of a storm may extend 1000 km to the south or southwest of the vortex center. The band tends to be long and narrow, with an east-west width of 50-100 km. The frontal band is not a solid band of precipitation but rather is represented by patches of precipitation covering $\sim$10% of the region. Rates exceed 6 mm/h in <1% of the zone.

4. Postfrontal convective showers that tend to be smaller, shallower, less intense, and more sparse than those within the frontal zone. These showers are more randomly distributed but still tend to orient themselves in bands. The postfrontal shower region covers a large area, but active precipitation in the zone probably covers well under 100 km^2 at any one time.

Figure A-1 shows a composite of the models of Nagle and Serebreny,[12] Austin and Houze,[13] and Boucher,[11] with characteristic radar echo signatures for each of the four major regions from Battan.[14] The figure indicates the inhomogeneity of precipitation echoes, but the absence of quantitative rate information undoubtedly results in an underestimate of the variations. Clearly, the size, depth, and number of fundamental cellular units depend on location within the main system.

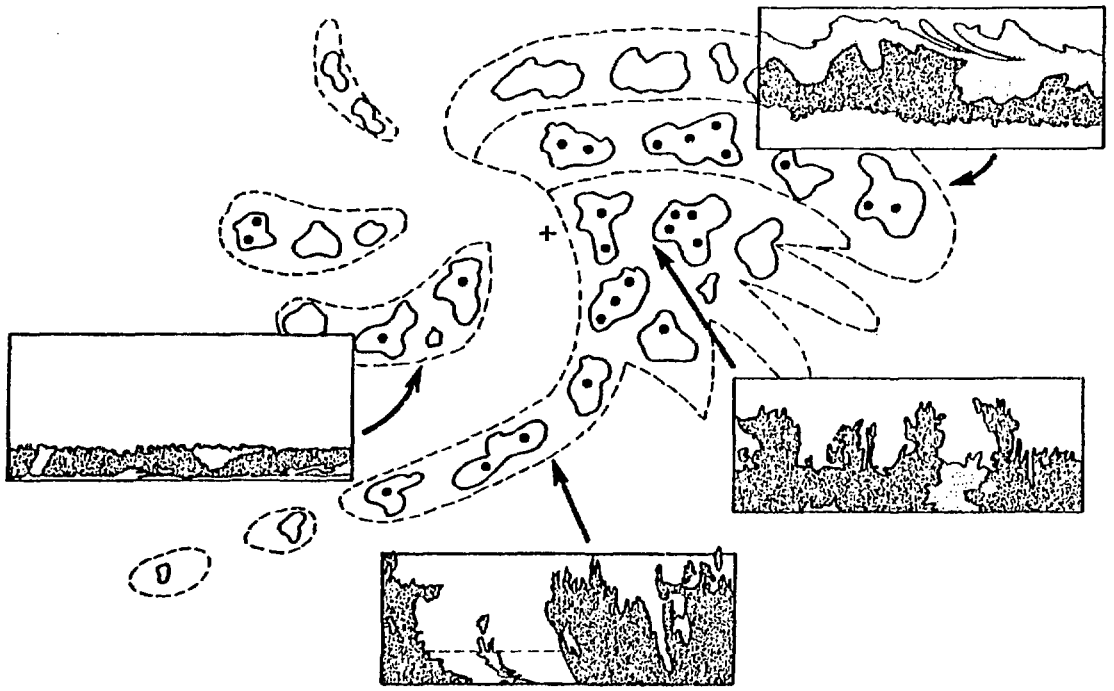

Fig. A-1
Composite diagram of precipitation zones in a mid-latitude storm.

The relationship between geographic location and type of precipitation encountered depends on local topography, upstream moisture sources, and the preferred tracks of synoptic storms. Although storms vary widely in development and motion, climatologists have been able to identify a few most likely storm tracks for a given region. These tracks can be related to properties of atmospheric general circulation and orographic conditions. Figure A-2 represents the two dominant storm tracks for western Europe derived from Woronicz.[6] The northernmost track, which tends to be a summer case, would subject west Germany to frontal convective and postfrontal air-mass showers. The southern track would tend to occur in winter and produce light, continuous precipitation. The reduced incidence of storms between the two dominant paths is due partly to the orographic barrier of the Alps.

On the subsynoptic scale, many variables concerning precipitation structure are considered: rain area fraction (RAF), central peak rainfall intensity, intensity as a function of spatial position, cell size distribution, cell lifetime, cell shape, cell movement, orientation of cells' major axis, and

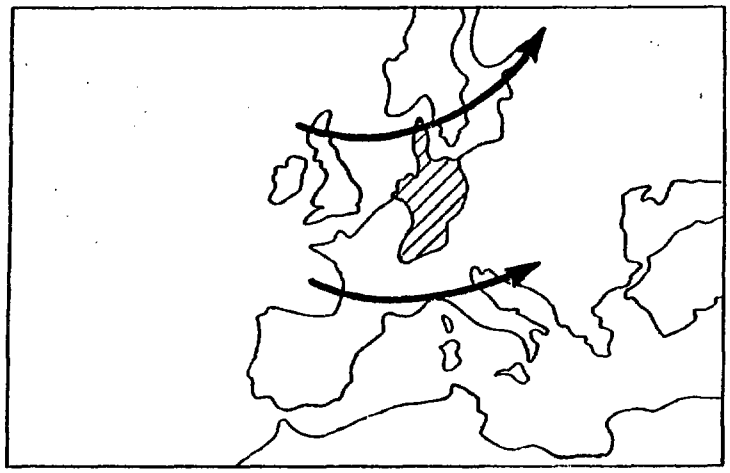

Fig. A-2
Major storm tracks over Western Europe.

spatial variation of precipitation intensity. These quantities may vary within each synoptic zone above, but most of our calculations to date vary only the rain area fraction in each zone in the TEMPEST and SCAWUEN programs. Most of these quantities are given statistical distributions specified as cumulative probability distribution functions.

The open literature has a number of fine papers summarizing various statistical results of radar precipitation patterns.[11-22] Table A-1 presents selected parameters of precipitation patterns for each of the four major zones of an occluding cyclone. The table entries were derived from the literature references, and as many corroborating data sources as possible were used. The entries reflect a measure of subjectivity in compromising among various reported results, but these compromises were generally easy to make because there was a remarkable consistency among the authors. The largest differences appeared in how the quantities were defined: different researchers defined similar structure in either descriptive or statistical terms, or both.

Our simulation model is based on the parameters of Table A-1, and the initial inputs were derived from the table entries. As the computational properties of the model evolved, however, we also recognized certain consistency requirements that changed the character of the parameterization. As the evolutionary nature of the model is important in understanding its present form, we will discuss some parts of Table A-1 and then present the current parametric scheme.

TABLE A-I

SUMMARY OF PROPERTIES OF MESOSCALE PRECIPITATION STRUCTURE

(Numbers in square brackets denote references used in deriving table entries.)

Property	Continuous Stratiform	Patchy Stratiform	Frontal Convective	Postfrontal Convective
Area (km^2) per Storm [11,12,13]	10^5	10^3	10^4	10^5
Fraction of Storm Area with Precipitation $\geq$0.25 mm/h [13,15]	0.10-0.2	0.10-0.2	0.10	0.02
Maximum Cell Area (km^2) [12,15,16,17,18,19]	$f(A_m) = \frac{1}{A_m\sqrt{2\pi\sigma_m^2}} \exp\left[\frac{1}{2\sigma_m^2}(\ell nA_m - m)^2\right]$			
	$m = 2.5$ to 3.2, $\sigma_m^2 = 0.3$ to 1.0			
Altitude (km): 0.5 mm/h [13,14,15,20]	3	4.5	5-10	5-6
2.5 m/h	0	2	1-5	1-3
6.0 m/h	0	1-2	0-3.5	0-1
Hourly Av Rate (mm/h) [15,16,21]	1	3	3	<0.1
Lifetime, T (h) [13,15,16]	Scale-dependent: $T \sim 0.8\ L^{2/3}$ (L = characteristic size). Height-dependent: 0.08 h per 2-km vertical extent.			
Shape [13,15,16]	Ellipse, with aspect ratio β given by the cumulative distribution function:			

β'	1.0	0.8	0.5	0.33
$P(\beta \geq \beta')$	0	0.25	0.6	1.0

Orientation (with respect to W/D) [13]: Degrees, θ, measured clockwise, given by the cumulative distribution function:

θ'	90	100	110	200	290	360
$P(\theta \leq \theta')$	0	0.15	0.70	0.85	0.95	1.00

Movement [16]: Approximately parallel to mid-tropospheric wind

Rate variation within cells [22]: (Eq. A-3), $0.25 \leq \gamma \leq 0.5$

The area coverage is a function of the type of precipitation or the location in a storm. Table A-I shows that the continuous-stratiform region probably has the largest area covered by precipitation, although generally of low intensity. If we select a clock-hour rate criterion of 2.5 or 6 mm/h, the ragged patchy stratiform and the frontal-convective zones show the most coverage. Zawadski[16] performed a detailed case study on a developing frontal wave that passed through Montreal on September 16, 1969. The gross statistics he calculated from the radar returns can be combined to give a simple proportionality relation between the mean rainfall rate and its standard deviation:

$$\sigma = 1.8 \langle R \rangle \quad , \tag{A-1}$$

where the angle brackets denote spatial average. Zawadski used autocorrelation functions to deduce the mesoscale structure of the precipitation. The Lagrangian autocorrelation yields information on the characteristic lifetime of precipitation units. Zawadski reports lifetimes of identifiable precipitation features to be about an hour.

The two-dimensional autocorrelation yields a shape characteristic that is essentially elliptical with a ratio of major to minor axes of about 1.5 to 2.0, which is consistent with other studies. For the smaller scales (<10 km), the shape is nearly circular.

The storm system moved with the individual cells until the final stage, when the storm appeared to be nearly stationary, with cells forming on the upwind side, moving through, then dissipating at the downwind edge. Although Zawadski did not compare the movement with observed winds, the cells and system appeared qualitatively to move parallel to the upper-level flow.

The precipitation-cell size distribution derived from a composite of radar results of Marshall and Holtz,[15] Konrad et al.,[23] and Austin and Houze[13] and from rain-gauge results of Fullerton and Wilson[22] appears to satisfy the log-normal relationship given in Eq. (A-2):

$$f(A_m) = \frac{1}{A_m \sqrt{2\pi\sigma_m^2}} \exp\left[-\frac{1}{2\sigma_m^2}\left(\ell n A_m - m\right)^2\right] \quad , \tag{A-2}$$

where A_m is the maximum cell area and m and σ_m are parameters of the distribution given by: median = e^m, mode = $e^{m-\sigma_m^2}$. The observed cell size

distributions demonstrate a great deal of consistency among the different geographical locations of the observation sites.

We recognized early in our work that processes such as precipitation scavenging that depend on the colocation of airborne debris and precipitation have a fundamental resolution requirement determined by the characteristic scales of variation of the two functions. In the present application, this resolution translates to a few kilometers and to a few tenths of hours. Conventional rain data do not provide this resolution, but, by the techniques discussed above, we were able to simulate precipitation with the required resolution. An acid test of such a model, of course, is its ability to match the observed conventional precipitation characteristics when they are appropriately integrated (see also Appendix F). The current parameters are the result of tuning efforts to produce precipitation that matches records for 4-min, 1-h, and 6-h rainfall observations in Germany.

Several parameters described in Table A-I that are factored into the model were determined to have a weak input to either simulated rain-gauge records or scavenging-event probability. These parameters received less attention than those that showed greater sensitivity, such as the cell size distribution, the distribution of maximum rain intensities, and the rain area fraction, which bear very directly on precipitation integrals. On the other hand, the aspect ratio and the orientation of cells appeared to affect the integrated rainfall much less. Also, transitions from one zone of a storm to another had only minor effect but complicated the interpretability, so parametric studies were performed with 6- to 10-h traverses through a single zone.

The results of RAF variation are shown in Fig. A-3. The RAF generally remains at 40% or less. Use of much larger values results in severe overestimates of the 1- to 6-h precipitation totals. The RAF is basically a real physical parameter describing that fraction of a large area that precipitation is covering at a given time. The parameter is also related to cell size distribution and cellular-intensity cross section.

In simulating a mesoscale precipitation structure, we must address several items of precipitation-rate information. Two main items are the distribution of peak rain rates for various cells and the form of rain-rate variation within the cell. Data for defining either parameter in detail are scarce, although existing data can certainly afford guidance in selecting logical functions and magnitudes. The fundamental precipitation units require rate data at very high

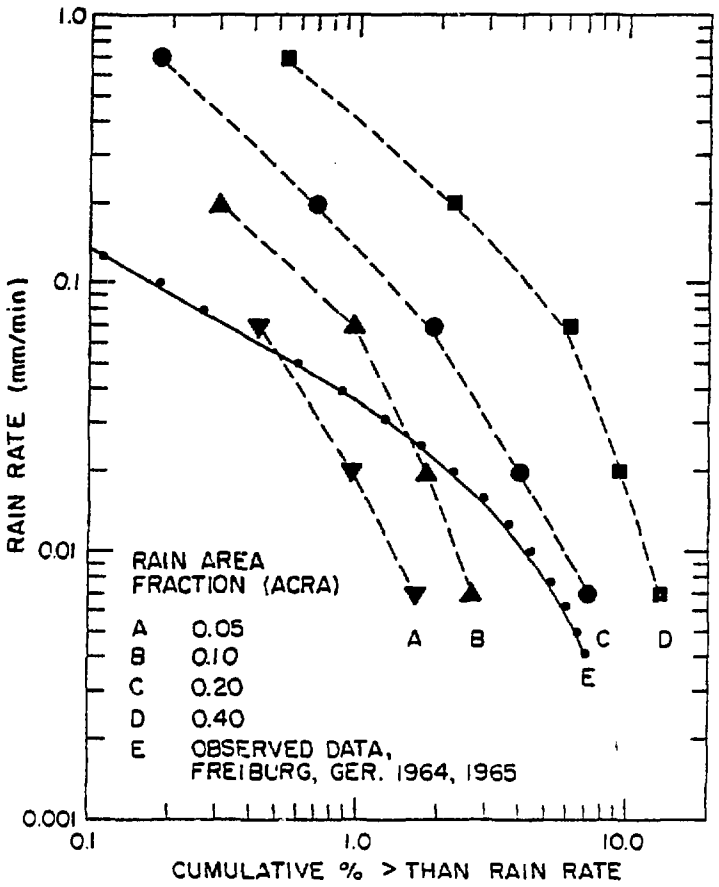

Fig. A-3.
Effect of rain area fraction on distribution of rain rates.

resolution to document their statistical properties. Two data sources are the 1-min-resolution data of Jones and Sims[24] and the work of Fullerton and Wilson,[22] which reflects resolution of a few seconds. These studies show precipitation rates that are very high compared with data that are smoothed over periods of an hour. Figure A-4 shows the distribution of peak rates derived by Wilson from radar and in situ measurements. Rates exceeding 100 mm/h are observed, whereas the median rate for cell cores is 25-30 mm/h.

The decrease in precipitation rate from the core of a cell to its edge has been expressed in the form

$$R(r_i) = R_o \exp\left[-\frac{r_i^2}{2\gamma_i^2 a_i^2}\right], \quad i = 1,2 \quad . \tag{A-3}$$

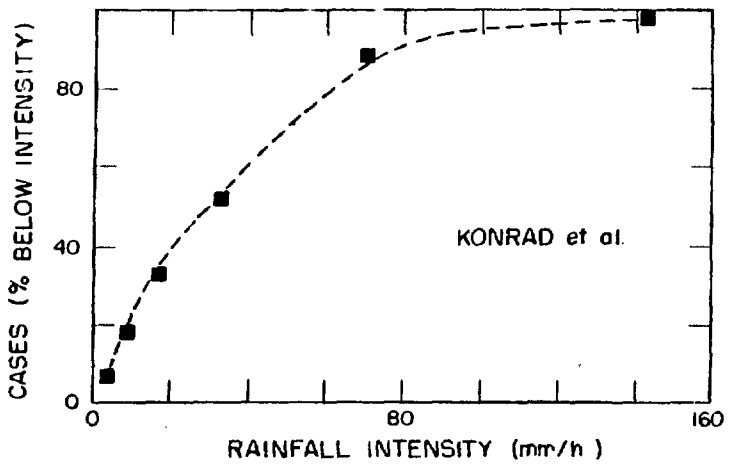

Fig. A-4.
Distribution of peak precipitation rates.

There is no rigorous basis for selecting Eq. (A-3), and existing data offer little promise of imminent empirical documentation. The function does, however, offer a reasonable variation that has flexibility in the parameter γ to adjust "peakiness" and account for regions of very low background rates with narrow shafts of heavy rain (small γ). When RAF, γ, and cell sizes are all large, areas of low rain rate would be extensive and peaks of high rate would be few. As cell sizes go down, the number of peaks would increase. If γ were increased while the other two parameters stayed constant, the peaks would be broader, yielding more rain. As RAF goes down, the rain coverage drops from continuous to sparse. This method of describing rain morphology is thus quite general and includes such usual descriptions as "continuous light rain" and "scattered showers."

APPENDIX B

ACTIVITY NORMALIZATION AND INFINITE WHOLE-BODY DOSE (IWBD) ESTIMATION

The SHASTA code estimates free-field IWBD from ground-deposited debris by means of the following assumptions:

1. Biological dose rate, d_t, from deposited debris is proportional to the energy-decay rate of the debris; and this is, in turn, proportional to t^c, where t = time from detonation and c is a "decay constant."

2. Rainout-deposition times of interest, t_d, lie between a few tenths of an hour and a few tens of hours after detonation.

3. The proportionality factor between dose rate and deposited-debris decay rate is a constant such that[25]

d_1 = dose rate from deposited debris at 1 h after detonation.

= 2600 (rem/h) per (equivalent kt/mi^2) of deposited-debris intensity.

Thus,

d_t = dose rate from deposited debris at time t after detonation

$$= d_1 t^c \quad , \tag{B-1}$$

and, for a SCAWDEN-SHASTA simulation,

$$d_t = 2600 t^c (\text{rem/h})/(\text{kt/mi}^2)$$

$$= 6734 t^c (\text{rem/h})/(\text{kt/km}^2)$$

$$= 6734 Y \frac{I_{jk}}{M} t^c (\text{rem/h}) \quad , \tag{B-2}$$

where Y = fission-equivalent yield (kt), I_{jk} = deposited-debris intensity (particles/km^2), and M = number of source particles in the simulation.

For gross fission-product activity, the parameter c can be taken to be constant as a function of time, over the time span of assumption 2, with errors of less than 10 to 20%. Also, for such deposition times, IWBD can be estimated within <10-30% by

$$\text{IWBD} \approx \int_{t_d}^{kt_d} d_t \, dt \quad , \tag{B-3}$$

provided κ is a few hundred or larger and t_d is in the range of assumption 2. Equations B-1 to B-3 then give

$$IWBD \approx \frac{(k^{1+c} - 1)}{1 + c} d_{t_d} t_d$$

$$= \frac{6734(k^{1+c} - 1)}{1 + c} Y \frac{I_{jk}}{M} t_d^{1+c} (rem/h) \quad . \tag{B-4}$$

In the calculations for this report we used $c = -1.24$ and $\kappa = 200$ to get

$$IWBD \approx 3d_{t_d} t_d = 2.02 \times 10^4 Y \frac{I_{jk}}{M} t_d^{-0.24} \quad . \tag{B-5}$$

APPENDIX C
THE NCAR WIND DATA BASE AND SPOOR INTERPOLATION SCHEMES

The built-in mean-wind data we use in SPOOR came from data tapes compiled by the National Center for Atmospheric Research (NCAR), Boulder, Colorado.[26] The NCAR compilations contain worldwide historical wind data translated to the National Meteorological Center (NMC) octagonal grid system.[27] Figure C-1 shows the northern hemisphere of this system, which is a regularly spaced rectangular grid laid out on a polar stereographic projection of the earth's surface. We later give the transformations between NMC (I,J) coordinates and geographic (latitude-longitude) coordinates. We have written codes* to read the NCAR tapes, process and print the data in various ways, tally and print statistical features of the data, and produce a SPOOR wind-data tape.

The specific data base now in SPOOR covers a 42-point, western Europe subset (I = 33, 34, 35, 36, 37, 38; J = 23, 24, 25, 26, 27, 28, 29) of the NMC grid. Figure C-2 shows this subset.

---

*This was the work of W. Rich and R. Allenson, LASL.

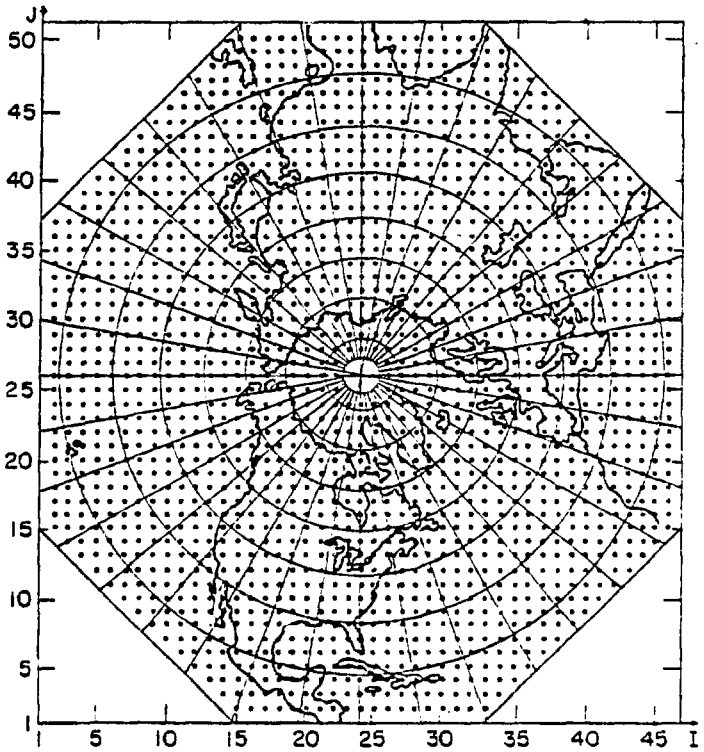

Fig. C-1.
NMC 47 by 51 grid. There are 1977 data points in the octagon. The pole point is I,J = 24, 26.

The NCAR data are given in (I,J) space and consist of orthogonal wind components, $\bar{u}$ in the I-direction and $\bar{v}$ in the J-direction. For each of the 42 (I,J) grid points shown in Fig. C-2, the specific data set extracted for SPOOR gives these components at 6 pressure altitudes (850, 700, 500, 400, 300, and 250 mbar) for each 12-h interval from September 1963 to December 1967.*

Because SPOOR operates in a continuous phase space, we needed an interpolation scheme to supply $\bar{u}$ and $\bar{v}$ values between the data-base points; and we developed a generalized code module for this purpose.[28] When called by SPOOR, this module generates biquadratic or bicubic least-square fits of the appropriate data-base winds versus I and J for any of the six altitudes and 12-h time points in the data base. Linear interpolations in altitude and time then provide the required $\bar{u}_j$ and $\bar{v}_j$.

*Many of these data are not actually available. We have used simple linear extrapolations and interpolations to infer missing data-base entries.

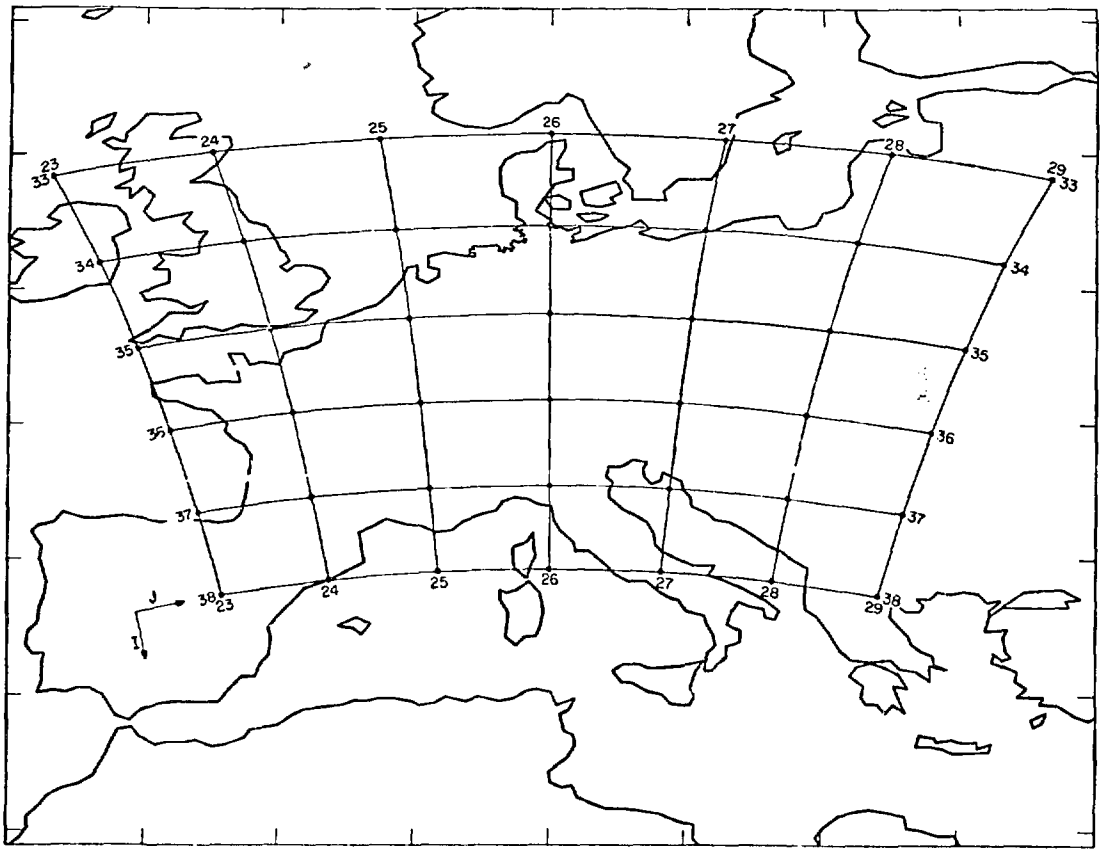

Fig. C-2.
NMC grid from SPOOR overlaid on map of Western Europe.

To illustrate, consider a trajectory step beginning at $\omega_j = (I_j, J_j, z_j, t_j)$, which defines bounding altitudes z_k and z_{k+1} and times t_i and t_{i+1} in the data base, so that

$$z_k \leq z_j \leq z_{k+1} \quad ,$$

$$t_i \leq t_j \leq t_{i+1} \quad .$$

we then make separate least-square fits versus I and J over the 42-point grid of Fig. C-2 for altitudes k and k + 1 at times i and i + 1. Linear interpolations in z and t between these surfaces then give $\bar{u}_j = \bar{u}(\omega_j)$ and $\bar{v}_j = \bar{v}(\omega_j)$.

It is convenient to do these calculations in the (I,J) space, whereas the SPOOR tracking module operates more conveniently in the horizontal (x,y) space defined at each step by the tangent plane to the earth's surface at ω_j. A transformation between the (I,J) and (x,y) spaces is thus required. We avoid some complications by using instead the transformation between (I,J) coordinates and geographic coordinates.[27] As an example, for step j at ω_j, let the displacements in (x,y) space be $(\Delta x_j, \Delta y_j)$, where

$$(\Delta x_j, \Delta y_j) = (v_j \Delta t, u_j \Delta t) \quad .*$$

The corresponding displacements in (I,J) space are

$$(\Delta I_j, \Delta J_j) = (\Delta y_j / \Delta E_j, \Delta x_j / \Delta E_j) \quad ,$$

where

$$\Delta E_j = 381/k_j \quad ,$$

$$k_j = \frac{1 + \sin 60^\circ}{1 + \sin \phi_j} \quad ,$$

$$\phi_j = \text{latitude of the point } (I_j, J_j) \quad ,$$

$$\sin \phi_j = \frac{4a^2 - R_j^2}{4a^2 + R_j^2} \quad ,$$

$$R_j^2 = (I_j - 24)^2 + (J_j - 26)^2 \quad ,$$

$$4a^2 = 973.712023868 \quad .$$

---

*In SPOOR, we arbitrarily take the positive x-direction along the positive J-axis and the positive y-direction along the positive I-axis.

Substituting the (I,J)-to-geographical transformation for the (i,j)-to-(x,y) transformation introduces a small bias in the trajectories, but, at latitudes of usual interest to us, this bias is small for track lengths up to several thousand kilometers.

APPENDIX D

RAIN-MORPHOLOGY MODELING IN THE TEMPEST CODE

The rain-cell geometry models used in TEMPEST are based on the following assumptions (see also Appendix A):

1. The synoptic storm geometry does not change shape with time.
2. All cells are elliptical and have a constant aspect ratio (ratio of minor to major axis) for a given cell as a function of time.
3. Initial cell positions are uniformly distributed in area in each storm zone.
4. Linear cell-growth is parabolic in time.
5. The cell areas A_{max} at maximum size are log-normally distributed.
6. Life-cycle times of new rain cells are uniformly distributed on their individual life-cycle time lines.

These assumptions, the input PDFs, and the logic flow described below completely define the TEMPEST methodology. Although some of these assumptions appear to be somewhat artificial, the parameters available in the formulation allow us to adjust overall cell structure and behavior to match statistically the characteristics of real precipitation systems. Furthermore, if we vary these parameters to study influences on final rainout effects, we find that the most important properties of the system are just those features that can be related empirically to real-world precipitation systems (for example, cell-size distributions, within-cell distribution parameters, and overall area fractions); these properties are exactly what is required of the model.

To outline the model specifics, we refer to Fig. D-1 and define the following:

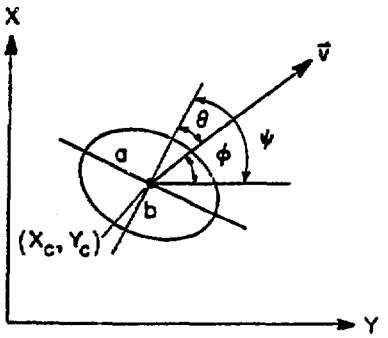

Fig. D-1.
Rain-cell geometry.

(X,Y) = TEMPEST coordinate system (defined by the storm-geometry input).

(X_c,Y_c) = location of a rain-cell center.

$\vec{V} = (V_X,V_Y)$ = rain-cell velocity (zone-dependent input).

ϕ = angle between the Y-axis and $\vec{V}$.

θ = angle between the cell minor axis and $\vec{V}$ (obtained from an input PDF).

$\psi = \theta + \phi$.

β = aspect ratio (obtained from an input PDF).

a = semimajor axis (see below).

b = semiminor axis = βa.

The equation for this cell is

$$AX^2 + BY^2 + CXY + DX + EY + F = 0 \quad , \tag{D-1}$$

where

$$A = \beta^2 \cos^2 \psi + \sin^2 \psi \quad ,$$

$$B = \beta^2 \sin^2 \psi + \cos^2 \psi \quad ,$$

$$C = 2(1 - \beta^2) \sin \psi \cos \psi \quad ,$$

$$D = -2[X_c(\beta^2 \cos^2 \psi + \sin^2 \psi) + Y_c(1 - \beta^2) \sin \psi \cos \psi] \quad ,$$

$$E = -2[Y_c(\beta^2 \sin^2 \psi + \cos^2 \psi) + X_c(1 - \beta^2) \sin \psi \cos \psi] \quad ,$$

$$F = X_c^2(\beta^2 \cos^2 \psi + \sin^2 \psi) + Y_c^2(\beta^2 \sin^2 \psi + \cos^2 \psi)$$

$$+ 2X_cY_c(1 - \beta^2) \sin \psi \cos \psi - \beta^2 a^2 \quad .$$

Both TEMPEST and SCAWUEM handle all rain cells in the form of Eq. (D-1). Because the parameters β and ψ are assumed constant throughout the lifetime of a given cell, the cell size is completely determined by the parameter a (semimajor axis).

A cell's growth curve is given in terms of the life-cycle parameters in Fig. D-2 plus a correlation between a_{max} and T_{max} taken from the literature.[15]

a_{max} = maximum value of semimajor axis during a cell's lifetime.

T_{max} = total lifetime of the cell.

$$T_{max} = 0.8\, a_{max}^{2/3}. \qquad \text{(D-2)}$$

When new cells are created (such as when TEMPEST sets up the starting cell structure), each new cell is assumed to start at a point in its life cycle selected uniformly over the interval $(0, T_{max})$ (assumption 6). To do this, we pick a δT uniformly on $(0, T_{max})$ (Fig. D-2); the cell's size as a function of time is then

$$a = G + HT + IT^2 \qquad \text{(D-3)}$$

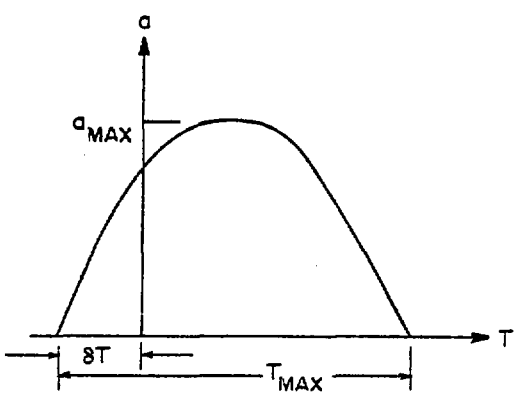

Fig. D-2.
Cell growth curve.

where

T = time measured from the cell's appearance (Fig. D-2),

$$G = 4a_{max}\delta T(T_{max} - \delta T)/T_{max}^2 \quad ,$$

$$H = 4a_{max}(T_{max} - 2\delta T)/T_{max}^2 \quad ,$$

$$I = -4a_{max}/T_{max}^2 \quad .$$

We thereby completely determine the history of a cell. When we need a new cell,

1. a value of A_{max} is selected from an input log-normal distribution* (assumption 5): Eq. (D-2) gives T_{max} for the cell,
2. a value of δT is selected uniformly on $[0, T_{max}]$, and
3. equations (D-3) and (D-1) then give the cell equations as functions of time.

The overall TEMPEST logic flow is as follows:

Inputs: Storm geometry, total TEMPEST time for the simulation, cell velocities, rain-area fractions (RAFs),** and PDFs for A_{max}, β, and θ.

1. Uniformly select an initial rain-cell location in a given zone of the storm system.
2. Select values of A_{max}, β, and θ from the appropriate PDFs.
3. Calculate coefficients for Eqs. (D-3) and (D-1).
4. Repeat steps 1 to 3 until the cumulative fractional rain-cell area in the given zone equals the input rain-area fraction.
5. Repeat steps 1 to 4 until all zones are filled.

This establishes the initial conditions for TEMPEST.

6. Advance all cells one time step in (X,Y), according to $\vec{V}$.
7. If, during any time step, a cell leaves its zone or its area goes to zero kill it and start a new cell for that zone as in steps 1 to 3.
8. Get new coefficients for all cells.
9. Repeat steps 6 to 9 from time step to time step until the total TEMPEST time is reached.

This gives the desired TEMPEST storm and rain-cell data for SCAWDEN.

---

*We use a routine given in Ref. 29.

**RAF is the same variable discussed in Appendixes A and G and Section IX.

APPENDIX E

SPECIFIC MODELS IN THE SCAWDEN CODE

1. RAIN-INTENSITY DISTRIBUTION WITHIN A PRECIPITATION CELL

A. Horizontal Distribution

The horizontal (X,Y) distribution of rain intensity within a cell is assumed to be a time-invariant, two-dimensional Gaussian whose center intensity varies with time as the cell area and whose center value is R_o when the cell is at its maximum size. The parameter h_o is picked from an input PDF that can depend on the storm zone. Consider a specific cell at a given time step (Fig. E-1):

(x_c,y_c) = location of the cell center (in SCAWDEN or SPOOR coordinates).
(x_s,y_s) = location of a SPOOR particle within the cell.
a = semimajor axis of the cell.
b = semiminor axis of the cell = βa.
β = aspect ratio of the cell.
ω = angle between the y-axis and the minor axis of the cell.
$h(\ell,d)$ = rain intensity at position (x_s,y_s) in the cell.

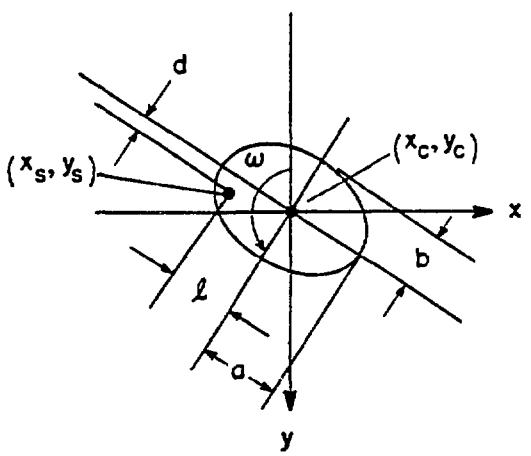

Fig. E-1.
Precipitation-cell and SPOOR-particle geometry.

Then,

$$\ell = (x_s - x_c) \cos \omega + (y_s - y_c) \sin \omega \quad ,$$

$$d = (y_s - y_c) \cos \omega - (x_s - x_c) \sin \omega \quad ,$$

and the rain intensity (mm/h) at (x_s,y_s), assumed to be proportional to cell area, is

$$R(\ell,d) = \left(\frac{a}{a_{max}}\right)^2 R_o \exp \left[- \left(\frac{\ell^2}{2\sigma_a^2} + \frac{d^2}{2\sigma_b^2} \right) \right] \quad , \qquad \text{(E-1)}$$

where

a_{max} = cell semimajor axis at maximum cell size,

$$\sigma_a = \gamma_x a \quad ,$$

$$\sigma_b = \gamma_b b \quad .$$

The distribution parameters γ_x and γ_y are key input variables that can be used to match the ACRA system to rain-rate frequency and intensity data.

B. Vertical Distribution*

In our present rain-intensity module, we assume an effective rain intensity that depends on altitude but not on the other SPOOR or TEMPEST state variables. The Z-dependence is introduced through a simple multiplicative factor to account for the expected decrease in rain intensity with increasing altitude. The rain intensity at time step j, corresponding to time t_j after the shot, at a location (x_s,y_s,Z_s) within a rain cell, is given by

$$R_j(x_s,y_s,Z_s) = R_j(\ell,d)\ \alpha(Z_s) \quad , \qquad \text{(E-2)}$$

where $R_j(\ell,d)$ is given by Eq. (E-1), and $\alpha(Z)$ is linearly interpolated from an input table.

*Also, see Appendix I.

A more sophisticated model to account for the variability of rain with altitude could readily be incorporated into SCAWDEN. Such a model could be either deterministic or stochastic, and it could be a function of any of the ACRA state variables, such as local winds, time, synoptic location in the storm system, and cell size. It could also use other types of input data such as PDFs for cell heights and vertical intensities. We have not incorporated such a model because it is not clear that the sensitivity of overall rainout effects to such details warrants upgrading our system at this time. This question probably deserves further investigation, however.

II. SCAVENGING OF DEBRIS PARTICLES*

The scavenging rate for a SPOOR particle located at the phase-space position $\vec{\Omega}_j = (x_j, y_j, z_j, t_j)$ in a local rain field with intensity given by Eq. (E-2) is

$$\frac{dW_s}{dt} = -\lambda(R_j)\, W_s \quad , \tag{E-3}$$

where W_s is the unscavenged debris weight represented by the SPOOR particle at $\vec{\Omega}_j$ and λ_j is a "scavenging coefficient."

Typically, λ depends on many factors and cannot be determined with high confidence. Sensitivity studies have established conservative values (highest rainout threat) for λ, however; and its dependence on rain intensity can be included explicitly. The resulting expression that we use is

$$\lambda = 1.26\, R^{0.8}\ (h^{-1}) \quad , \tag{E-4}$$

where R is the rain intensity from Eq. (E-2).

The debris weight scavenged by a rain cell from a contained SPOOR particle during a small time interval Δt is thus

$$\Delta W_s = W_s(1 - e^{-\lambda \Delta t}) \quad . \tag{E-5}$$

When a SPOOR particle at $\vec{\Omega}_j$ is inside several overlapping rain cells, the total

---

*Also, see Appendix H.

scavenged weight during Δt is taken as a linear sum of the independently scavenged weights from each of the several cells:

W_t = total weight scavenged during Δt from a given SPOOR particle at $\vec{\Omega}_j$

$$= W_s \sum_{i=1}^{k} e^{-\Delta t \sum_{j=1}^{i-1} \lambda_i} (1 - e^{-\lambda_i \Delta t}) \quad , \tag{E-6}$$

where i = 1, 2, 3, ..., k is a cell index for affected cells, the λ_i are scavenging coefficients at $\vec{\Omega}_j$ for the individual cells, and k is the number of cells within which the SPOOR particle is located at $\vec{\Omega}_j$.

After ΔW_t has been determined for a SPOOR particle, a new particle with weight ΔW_t is created at $\vec{\Omega}_j$, and the original SPOOR particle is continued to the next time step in its history with its weight reduced by ΔW_t.* The set of newly created (scavenged) particles from all the SPOOR particles at each time step constitutes the input to the deposition and tallying modules.

III. DEPOSITION OF SCAVENGED PARTICLES**

In SCAWDEN, each newly created scavenged particle is transported to the ground as follows:

Let $\bar{v}_z$ be the effective, vertical, water-transport velocity at altitude Z; then:

$$\bar{v}_z = 11.2R^{0.16} \text{ (km/h)},$$

where

R = rain-rate (mm/h) at Z = $\alpha(Z)$ R_g (R_g = ground rain rate).

---

*When the SPOOR particle's weight decreases to a low value, the particle is subjected to a Russian Roulette termination scheme,[30] at a substantial savings in computer time.

**Also, see Appendix H.

A scavenged particle located at vertical height Z_o (km) is then assumed to reach the ground in a time t_f given by

$$t_f(h) = \int_0^{Z_o} \frac{dZ}{\bar{v}_z} = 0.09 R_g^{-0.16} \int_0^{Z_o} \frac{dZ}{\alpha(Z)^{0.16}} \quad . \tag{E-7}$$

The ground rain rate is taken from Eq. (E-1). During the time t_f, each scavenged particle is transported horizontally according to a horizontal wind velocity that varies linearly from a value $\vec{v}(Z_o)$ at a scavenging altitude Z_o to $0.1\ \vec{v}(Z_o)$ at the ground; the horizontal velocity at any altitude Z between the ground and Z_o is thus given by

$$\vec{v}(Z) = \vec{v}(Z_o)\left(0.1 + 0.9\,\frac{Z}{Z_o}\right) \quad . \tag{E-8}$$

The velocity $\vec{v}(Z_o)$ is another input to SCAWDEN. Scavenged particles are tallied in the proper time intervals, as determined by t_f, and in a Lagrangian set of spatial bins on the ground see (Sec. VIII-A and below).

Typical $\vec{v}(z_o)$ values range from perhaps 10 to 80 km/h. The horizontal displacements of scavenged debris particles before they reach the ground are typically <10-20 km; the more important rainout events, those with higher rain rates, imply horizontal displacements $\lesssim$10 km. Such displacements are worth including in ACRA but do not warrant a more sophisticated treatment than that given here.

IV. EFFECTS-TALLYING GRID*

We assume rainout effects on the ground to be proportional to the intensity of locally deposited debris per unit area. This deposition intensity is determined by means of a Lagrangian tally-cell grid system erected at each time step in the calculation. This tally grid is formed by a set of annular rings centered on the ground-particle centroid, plus a set of K equally spaced angular divisions, as shown in Fig. E-2. The numbers of radial and angular

*Also, see Appendix B and Sec. VIII-A.

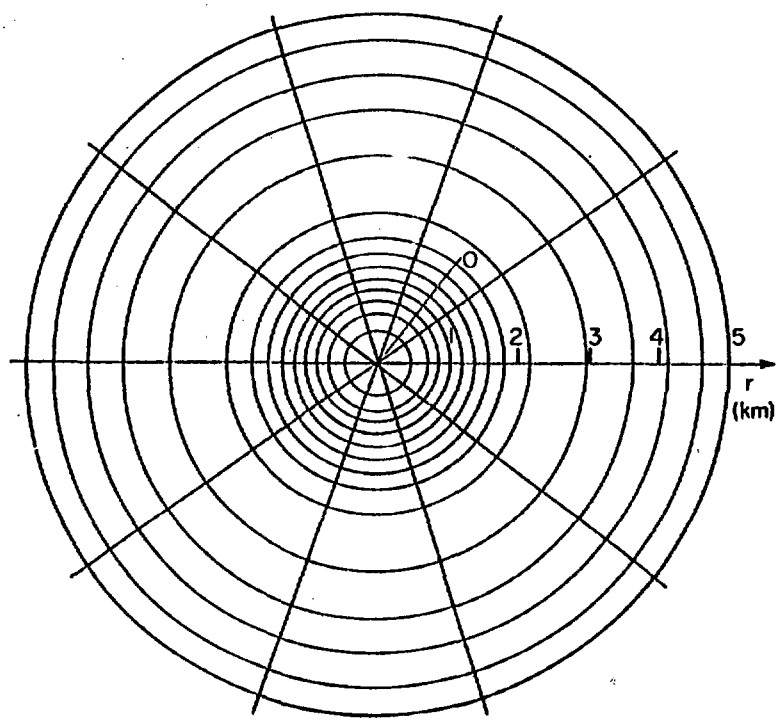

Fig. E-2.
Effects-tallying grid.

bins are inputs to SCAWUEN and are fixed throughout the calculation. Radial dimensions of the tally bins vary with time and are based on statistical properties of the ground distribution of debris.

To describe the radial binning for a given time step j, we define

ΔW_{jm} = weight deposited at step j from SPOOR particle m,

(x_{jm}, y_{jm}) = ground location of ΔW_{jm},

M = total number of SPOOR particles.

The centroid of the ΔW_{jm} at j is (x_{jc}, y_{jc}), where, if

W_j = total weight deposited during step j

$$W_j = \sum_{m=1}^{M} \Delta W_{jm} \quad , \tag{E-9}$$

then

$$x_{jc} = \frac{1}{W_j} \sum_{m=1}^{M} \Delta W_{jm} x_{jm} \quad ,$$

$$y_{jc} = \frac{1}{W_j} \sum_{m=1}^{M} \Delta W_{jm} y_{jm} \quad . \tag{E-10}$$

The radial positions of the ΔW_{jm}, as measured from the centroid, are given by

$$r_{jm} = \left[\left(x_{jm} - x_{jc} \right)^2 + \left(y_{jm} - y_{jc} \right)^2 \right]^{1/2} \quad , \tag{E-11}$$

and the first and second moments of r_{jm} about the centroid are, respectively,

$$\overline{r}_j = \frac{1}{W_j} \sum_{m=1}^{M} \Delta W_{jm} r_{jm} \quad , \tag{E-12}$$

and

$$\sigma_{r_j}^2 = \frac{1}{W_j} \sum_{m=1}^{M} \Delta W_{jm} r_{jm}^2 - \overline{r}_j^2 \quad . \tag{E-13}$$

To get a radial binning structure at step j, SCAWUEN uses Eqs. (E-9)-(E-13) and the following recipe to set up the first N - 1 bin radii.

r_n = radius of the nth annular ring from the center

$$= \left\{ 2\sigma_{r_j}^2 \ln \left[\frac{N}{N - n(1 - d)} \right] \right\}^{1/2}, \quad n = 1, 2, \ldots, N-1 \quad , \tag{E-14}$$

where

$$d = e^{-r_N^2/2\sigma_{r_j}^2} ,$$

N = an input integer,

r_N = largest of the r_{jm} values.

The remaining area, between r_{N-1} and r_N, is further subdivided into F additional annuli, each of equal area, where F is another input integer.

This radial binning scheme is designed to give roughly equal numbers of deposited particles in each bin, a desirable feature from the standpoint of statistical-sampling efficiency; Eq. (E-14) is derived to give approximately equal areas in each radial bin by assuming a Gaussian distribution of deposited particles with variance $\sigma_{r_j}^2$.

The intensity of ground-deposited debris (particles/km^2) in tally bin k at time step j is

$$I_{jk} = \frac{\sum_{m=1}^{M} \Delta W_{jmk}}{A_{jk}} , \qquad \text{(E-15)}$$

where

ΔW_{jmk} = weight deposited in bin k at time j by particle m,

A_{jk} = area of bin k at time j (km^2).

All tally-bin locations, dimensions, and debris intensities for all time steps are outputs to SHASTA, for final effects tallies.

APPENDIX F

SPECIFIC MODELS IN THE RAIN CODE

The RAIN code uses a standard TEMPEST output and executes a modified SCAWUEN simulation to tally rain rates and rain-frequency distributions at a fixed ground point. For a given time step Δt and a given rain cell passing over the fixed point during Δt, RAIN assumes the distribution of rain intensity on the ground to be given by the SCAWUEN intensity distribution for that cell over the given time interval (Eq. E-1). RAIN then time-integrates this intensity over Δt, along the path traced out by the point across the (x,y) projections of the cell on the ground. This integration is performed for every cell passing over the point during each Δt in a TEMPEST-SCAWUEN calculation, and contributions from all cells are added together for each Δt to get total rain at the point during each Δt. These data can be binned and averaged over any other time interval (greater than Δt) to get appropriate rates and frequency distributions to compare with measurements.

Figure F-1 shows the geometry for a given integration. We use SCAWUEN coordinates, consider a given time step j, and define the following for that time step:

(x,y) = SCAWUEN coordinates,

$(x-x_c, y-y_c)$ = translated SCAWUEN coordinates (as indicated in Fig. F-1),

(x_c, y_c) = location of the cell center at the given time step (from SCAWUEN),

(x_p, y_p) = location of the fixed ground point,

$\vec{v} = (v_x, v_y)$ = (constant) cell velocity,

a = semimajor axis of the cell (from SCAWUEN),

$b = \beta a$ = semiminor axis of the cell (from SCAWUEN),

P_1, P_2 = intersections of the cell boundary and the extrapolated path of the point across the cell,

(x', y') = coordinate system defined along the cell axes (Fig. F-1),

$R(x', y')$ = rain intensity distribution for the cell (Eq. E-1).

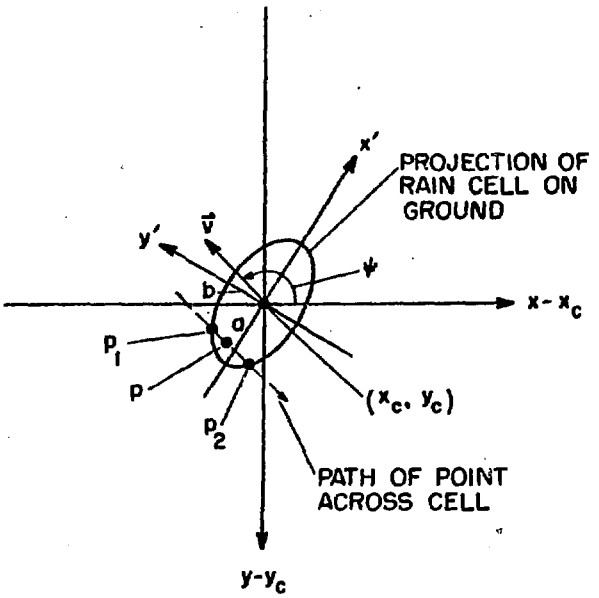

Fig. F-1.
RAIN integration geometry.

The desired integration is then

R = total rain during Δt at the fixed point from the given cell

$$= \int_{t_1}^{t_2} h(x',y')\, dt, \qquad \text{(F-1)}$$

where the integration is along the path of the point across the cell during Δt. The path of the point across the cell is a straight line with the equation

$$y = y_o + mx = y_p + \left(\frac{v_y}{v_x}\right)(x - x_p) \quad , \qquad \text{(F-2)}$$

or, in the (x',y') coordinate system,

$$y' = A + Bx' \quad , \qquad \text{(F-3)}$$

where

$$m = \frac{v_x}{v_y} \quad , \tag{F-4}$$

$$y_o = y_p - mx_p \quad , \tag{F-5}$$

$$A = \frac{y_o}{\cos \Psi - m \sin \Psi} \quad , \tag{F-6}$$

$$B = \frac{m + \tan \Psi}{1 - m \tan \Psi} \quad . \tag{F-7}$$

The intersections p_1 and p_2 are given by the above equations, and

$$x'_{1,2} = - \frac{AB}{B^2 + \beta^2} \pm \sqrt{\left(\frac{AB}{B^2 + \beta^2}\right)^2 - \frac{A^2 - b^2}{B^2 + \beta^2}} \quad . \tag{F-8}$$

We also need the location of the point p and the velocity, $-\vec{v}$, of p across the cell in (x',y') coordinates:

$$x'_p = x_p \cos \psi - y_p \sin \psi \quad , \tag{F-9}$$

$$y'_p = x_p \sin \psi + y_p \cos \psi \quad , \tag{F-10}$$

$$v_{x'_p} = -v_x \cos \psi + v_y \sin \psi \quad , \tag{F-11}$$

$$v_{y'_p} = -v_x \sin \psi - v_y \cos \psi \quad . \tag{F-12}$$

To effect the integration in Eq. (F-1), we note that the point travels across the cell at constant velocity ($v_{x'_p}$, $v_{y'_p}$), and we assume it to be at point p (see Fig. F-1) midway during the interval Δt. The times required to travel from p_1 to p and from p to p_2 are then

$$\delta t_1 = \left| \frac{x_1 - x'_p}{v_{x'_p}} \right| ,$$

$$\delta t_2 = \left| \frac{x'_2 - x'_p}{v_{x'_p}} \right| . \qquad \text{(F-13)}$$

This establishes the integration limits for the interval Δt; namely, the integration is from $t_1 = \delta t_1$ or $\Delta t/2$ (whichever is smaller) to $t_2 = \delta t_2$ or $\Delta t/2$ (whichever is smaller).

Because of the form of $R(x',y')$, Eq. (F-1) cannot be integrated in closed form. It can be conveniently integrated, however, in terms of an approximation given by Hastings:[31]

$$\frac{2}{\sqrt{\pi}} \int_0^x e^{-t^2} dt \approx 1 - \frac{1}{\left(\sum_{i=0}^{4} a_i x^i \right)^4} , \qquad \text{(F-14)}$$

where the a_i are constants given in Ref. 31. The result is

$$R = \frac{R(0,0)\ F}{2|v_x|} \sqrt{\frac{\pi}{c}} \left| \left[1 - \frac{1}{\left(\sum_{i=0}^{4} a_i |Z_A|^i \right)^4} \right] \pm \left[1 - \frac{1}{\left(\sum_{i=0}^{4} a_i |Z_B|^i \right)^4} \right] \right| , \qquad \text{(F-15)}$$

where

$$F = e^{C\left(\frac{D^2}{4} - E\right)} , \qquad \text{(F-16)}$$

$$C = \frac{\gamma_y^2 \beta^2 + \gamma_x^2 B^2}{2\gamma_x^2 \gamma_y^2 \beta^2 a^2} , \qquad \text{(F-17)}$$

$$D = \frac{2\gamma_x^2 AB}{\gamma_y^2\beta^2 + \gamma_x^2 B^2} , \tag{F-18}$$

$$E = \frac{\gamma_x^2 A^2}{\gamma_y^2\beta^2 + \gamma_x^2 B^2} , \tag{F-19}$$

$$Z_A = \sqrt{C}\left(x_1' + \frac{D}{2}\right) , \tag{F-20}$$

$$Z_B = \sqrt{C}\left(x_2' + \frac{D}{2}\right) . \tag{F-21}$$

The parameters A, B, γ_x, γ_y, β, and a are defined above and in Appendix E; the a_i are the constants given in Ref. 31; the positive sign in Eq. (F-15) applies when Z_A and Z_B have opposite signs, and the negative sign applies when the signs are the same.

APPENDIX G

ESTIMATING THE SPECTRUM OF RAIN AREA FRACTIONS

The statistics of precipitation accumulation in ACRA depend on several parameters in the code system, including:

1. Rain area fraction (RAF)
2. Cell size distribution (σ_m^2, m)
3. Distribution of cellular peak precipitation intensity (R_o)
4. Cellular-intensity cross section (γ).

Synoptic meteorologists can estimate RAF in real time from weather-map analyses. This ability makes RAF a useful assessment parameter. RAF is also one of the most sensitive parameters for determining the statistics of precipitation accumulations. To minimize the degrees of freedom in modeling rainfall, we have tried to determine the other parameters for a given climate

region and then let RAF be the variable that separates periods of heavy and light rain. This approach assigns the RAF a role of dummy variable within the modeling context; we also feel that its interpretability as a physical quantity is what might be expected subjectively.

Our approach to tuning the model has been to use rain-gauge records on various scales of time resolution, after scoping the range of parameter variation by using rainfall records as described in Appendix A. The model may be used to simulate the precipitation collected in a stationary rain gauge as a storm passes over it. This simulation has been made for several gauges separated spatially, with records of 0.1-, 1- to 3-, and 6-h precipitation accumulations being simulated. The 0.1-h statistics were compared with high-resolution (4-min) rainfall accumulations for two stations in Germany (Koblenz and Freiburg) so we could select reasonable values for all parameters except RAF. We then used 1- and 6-h accumulations to determine the spectrum of RAF values as follows:

Figure G-1 shows the cumulative probability distribution of 6-h rain amounts. Figure G-2, produced by the model, estimates the corresponding accumulations as functions of $\overline{RAF}$. By equating the accumulation statistic in Figs. G-1 and G-2, it becomes a straightforward matter to generate Fig. G-3 (the cumulative density function of $\overline{RAF}$, given the existence of a rainy period) and the family of parameters describing cell size and intensity. Given the currently available data set, we feel Fig. G-3 represents a reasonable spectrum of $\overline{RAF}$ values over the middle 90%-frequency-of-occurrence range.

We have to address the rationale for equating the 6-h accumulations in Figs. G-1 and G-2 to construct Fig. G-3. Figure G-2 represents the rainfall at a number of sites for a given, statistically homogeneous region characterized by a specific $\overline{RAF}$. Figure G-1 is also made up from data for a number of sites. The only criterion for counting an event, however, is that it must have rained at some time during the 6-h period; the properties of a precipitation region have no bearing on the count criterion. The selection of a time scale $\leq$6 h and the consistency between 1- and 6-h results suggest that, in general, equating the statistic with its model counterpart is justified.

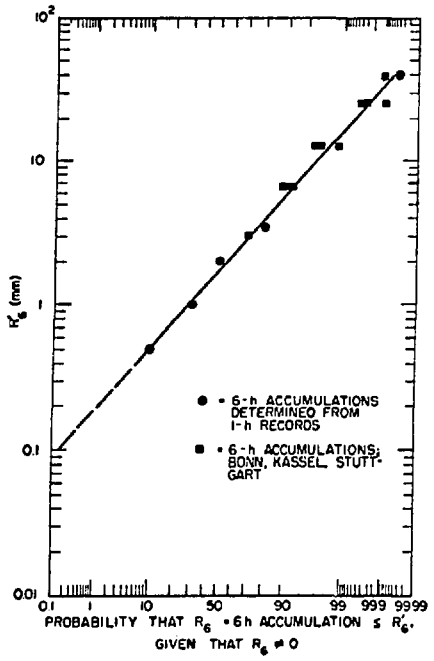

Fig. G-1.
Cumulative conditional probability distribution of 6-h rain amounts; selected West German stations.

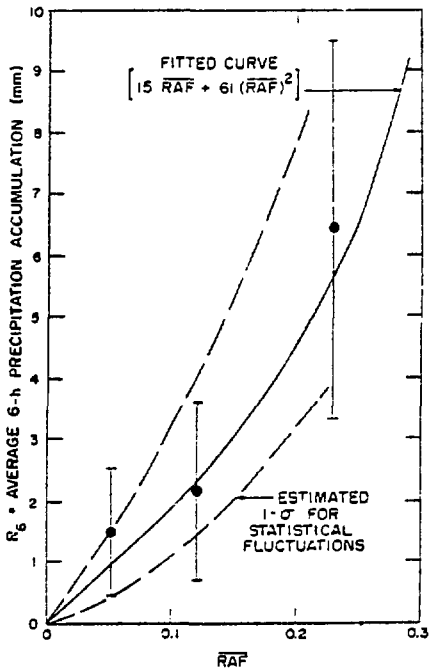

Fig. G-2.
Average 6-h ground accumulations vs $\overline{RAF}$; estimated with rain code for standard TEMPEST-SCAWUEN scenario.

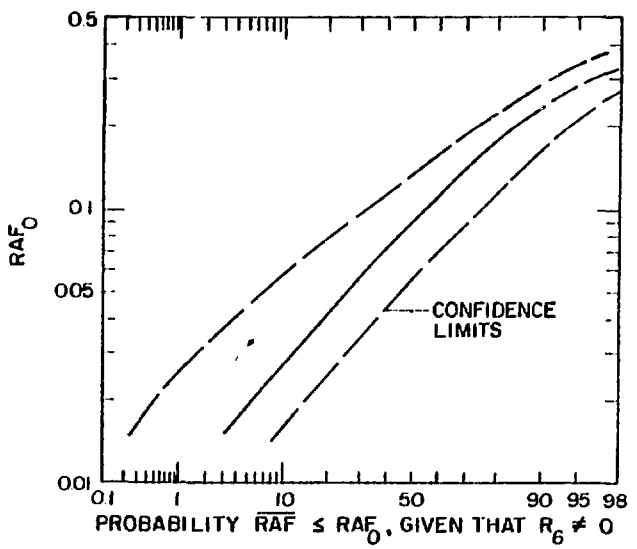

Fig. G-3.
Cumulative conditional probability distribution of $\overline{RAF}$ derived from climate data in Fig. G-1 and rain-case data in Fig. G-2.

APPENDIX H

PRECIPITATION SCAVENGING

J. Klett

Debris particles in clouds become incorporated in the cloud liquid water or ice phases through nucleation and the action of a variety of transport mechanisms, such as convective Brownian diffusion, turbulent diffusion, diffusiophoresis, thermophoresis, electrostatic interactions, and relative gravitational sedimentation leading to hydrodynamic or "inertial" capture. Because only approximate quantitative descriptions exist for most of these processes, even when they occur in isolation and involve only idealized particles (for example, spheres or infinite cylinders with homogeneous physical properties), it is understandable why, as yet, no definitive assessment of the scavenging problem exists.

Nevertheless, an important tentative conclusion may be drawn from the many idealized case studies that have been carried out in recent years.[32-36] These studies imply that in-cloud scavenging by convective, precipitating systems may be regarded basically as a two-stage process. In the first stage, all the scavenging mechanisms, and especially nucleation, Brownian and turbulent diffusion, and diffusio- and thermophoresis, serve typically to transfer a major fraction of the debris particles (assumed here to be characterized by radii $r \lesssim 1$ μm) to the cloud water, predominantly the fraction comprised of small droplets and/or ice crystals which together possess most of the total absorbing surface of the cloud water, in 20 min or less. In the second stage, this polluted cloud water is scavenged primarily through inertial capture by relatively large precipitating cloud particles such as raindrops, snowflakes, and graupel (soft hail) particles. This accretion process can cause a major fraction of the polluted water to fall out of the cloud in a time period similar to, though generally somewhat larger than, that for stage one. Thus, net fractional depletions of debris-particle concentrations of the order of unity may occur within the span of 1 hour, corresponding to an overall scavenging rate $-d \ln n_p dt$ of 10^{-3} to $10^{-4} s^{-1}$ (here n_p and t respectively denote debris particle concentration and time). This overall theoretical conclusion is quite consistent with the observation, based on experiments in

the field, that in-cloud scavenging operates with approximately the same efficiency as the processes which convert water vapor to precipitation.[37]

This description of the nature of in-cloud scavenging, in which the second stage is generally rate-limiting for the entire process, suggests that a reasonable upper bound for the effective scavenging rate is given by the accretion rate of small cloud particles by precipitation, with the former assumed to have already absorbed the debris aerosol through stage-one processes. Clearly, such a formulation will also represent an upper bound for the case of below-cloud scavenging ("washout") as well, because the efficiency of the accretion process increases rapidly with the size of the collected particles. Experimental studies imply washout scavenging rates that are typically at least an order of magnitude smaller than corresponding in-cloud "rainout" rates, for the same precipitation flux.[38,39] We shall also ignore possible evaporation losses between cloud and ground. Although evaporation typically reduces the water flux at the ground to about half of that at cloud base,[40] usually only a small fraction of this water loss is caused by drops that evaporate completely, allowing their captured debris particles to escape again into the environment before being "recycled" through further drop collection and breakup events. Finally, we shall consider only the case of a "warm" cloud with no ice phase, because terminal fall velocities and collision cross sections for most types of cloud ice particles are not well-known.

Consider the collection of droplets of radius r' by raindrops of radius $r \gg r'$. It is apparent that if there were no hydrodynamic deflection of approaching particles, the collection rate would be controlled simply by the relative velocity of approach and the geometric collision cross section. It is customary to describe the effect of hydrodynamic interaction on the collection rate by using the concept of the collision efficiency, $E = E(r',r)$, defined here to be the ratio of the actual collision cross section to the geometric cross section for a pair of interacting drops. Then if $N(r,t)\,dr$ denotes the number of raindrops per unit volume on the interval $(r, r + dr)$ at time t, the local depletion rate of the concentration $n(r',t)$ of droplets may be expressed as

$$\frac{\partial n(r',t)}{\partial t} = -n(r',t) \int_{r_{min}}^{\infty} K(r',r)\, N(r,t)\, dr \quad , \tag{H-1}$$

where r_{min} denotes the minimum raindrop radius, and the "collection kernel" $K(r',r)$ is given by

$$K(r',r) = \pi (r' + r)^2\, E(r',r)[V(r) - V(r')] \, . \tag{H-2}$$

In this expression the quantity in square brackets is the difference between the terminal velocities of the drop and the droplet. We have also made the usual assumption that coalescence inevitably follows a collision event.

Long[41] has evaluated $K(r',r)$ versus r for various radius ratios r'/r, using the collision efficiencies of Shafrir and Gal-Chen[42] and Klett and Davis,[43] and the terminal velocities of Gunn[44] and Beard and Pruppacher.[45] An interesting result of Long's analysis is that K depends only weakly on the size ratio r'/r; for $10 \leq r \leq 500$ μm, K varies over about eight orders of magnitude for fixed r'/r, whereas for fixed r it changes by less than one order of magnitude for $0.2 \leq r'/r \leq 0.9$. This implies that the scavenging rate coefficient, $A(r',t)$, defined by the integral in Eq. (H-1), is only a weak function of r'.

Let us now assume a steady state rain spectrum according to the empirical description of Marshall and Palmer:[46]

$$N(r) = N_o e^{-\alpha r} \quad r \text{ in cm} \quad , \tag{H-3}$$

where $N_o = 1.6 \times 10^5$ m^{-3} cm^{-1} and $\alpha = 82\, R^{-0.21}$ cm^{-1}, and where R is the rain rate in mm h^{-1}. (Subsequent more detailed studies have shown that although rain spectra often have exponential forms as in Eq. (H-3), the constant N_o is itself usually a function of R, and the functional dependence of α on R varies somewhat from the above.[47] However, there appears to be no need for such refinements in the present application.)

In view of the results of Long,[41] we may now combine Eqs. (H-1)-(H-3) to obtain the following simple estimate for the maximum possible scavenging coefficient, which is independent of r' and t:

$$\Lambda \approx \pi N_o \bar{E} \int_0^\infty r^2 V(r)\, e^{-\alpha r} dr \quad . \tag{H-4}$$

To obtain this expression we have made use of the fact that K is well represented by its form for $r'/r \ll 1$; E thus represents a characteristic collision efficiency for drop-droplet interactions, and is approximately unity. The replacement of r_{min} by 0 in the lower limit of the integral is of little consequence, because of the factor $r^2V(r)$ in the integrand.

Also, from the observations of Beard and Pruppacher,[45] and considering the factors r^2 and $e^{-\alpha r}$ in the integrand of Eq. (H-4), we may represent the drop terminal velocity adequately by its variation over the range $50 \leq r \leq 500$ μm, namely,

$$\bar{V}(r) \approx Cr, \quad 50 \lesssim r \lesssim 500 \text{ μm} \quad , \tag{H-5}$$

where C is a function of air pressure and temperature.

We may eliminate reference to the parameters N_o and C by introducing the definition of rain rate. When expressed as a mass flux of rain, the rain rate R' is

$$R' = \frac{4\pi\rho_w}{3} \int_0^\infty r^3 N(r)\, V(r)\, dr \quad , \tag{H-6}$$

where ρ_ω is the density of water, and we have assumed the absence of an appreciable updraft. If R' is given in cgs units (i.e., as g cm^{-2} s^{-1}), then the rain rate in mm h^{-1} is $R = 3.6 \times 10^4\, R'/\rho_\omega$. Therefore, from Eqs. (H-4)-(H-6) we have

$$\frac{\Lambda}{R} \approx \frac{\bar{E}}{4.8 \times 10^4} \frac{\int_0^\infty r^3 e^{-\alpha r} dr}{\int_0^\infty r^4 e^{-\alpha r} dr} = \frac{\bar{E}}{4.8 \times 10^4} \left(\frac{\alpha}{4}\right) \quad , \tag{H-7}$$

which on substituting $\alpha = 82R^{-0.21}$ becomes

$$\Lambda\left(s^{-1}\right) \approx 4.2 \times 10^{-4}\, \bar{E} R^{0.79} \quad R \text{ in mm } h^{-1} \quad . \tag{H-8}$$

It is clear from the derivation that the accuracy of this estimate should not vary with height z, assuming the description $N(r)/N_o = \exp(-8? R^{-0.21} r)$ holds for all z.

A similar dependence of Λ on R for the rain scavenging of large particles is evident from the early numerical calculations of Chamberlain.[48] Furthermore, excellent agreement between Eq. (H-8) and the results of a numerical computation by Crandall et al.[34] of $\Lambda(R,r')$ versus R for $r' \gtrsim 10$ cm can be achieved by choosing $\bar{E} = 0.83$. Adopting this value, our final estimate for Λ is

$$\Lambda = 3.5 \times 10^{-4} R^{0.79}\left(s^{-1}\right) = 1.3 R^{0.79}\left(h^{-1}\right) \quad R \text{ in mm } h^{-1} \quad . \tag{H-9}$$

It is interesting to consider whether there are any conditions under which one might expect a significantly larger scavenging coefficient than Eq. (H-9). The one plausible situation that comes to mind is the thunderstorm environment, where strong turbulence and electrical forces might cause the rapid "self-collection" of drops of similar size, in addition to an enhanced accretion rate of small drops by larger ones. However, the fact that rain spectra similar to the Marshall-Palmer distribution given by Eq. (H-3) are observed in thundershowers implies that a more rapid coagulation of cloud water would tend to be balanced by a larger drop-breakup rate, so that the overall spectral shape would remain largely unchanged.

Nevertheless, there appears to be a significant difference between the thunderstorm and nonthunderstorm cases, in that the stronger drop interactions in the former case imply the debris particles will be more uniformly distributed over the drop spectrum; i.e., the pollutant-to-cloud-water mixing ratio will be a weaker function of drop size. This in turn implies that the scavenging rate in a situation of strong drop interactions may be estimated simply by the rate of total water depletion from the precipitating volume containing the debris. For example, if we suppose this volume is characterized by a vertical extent H and a horizontal cross section A, and that its liquid

water content is w (≡ water mass per unit cloud volume), then it contains a water mass of order AhW. If the rain rate is R', this amount of mass evidently will cross the bottom surface of the volume in a time τ, where AR'τ ≈ AhW. Hence, we estimate the scavenging rate to be $\Lambda_T \approx \tau^{-1} \approx R'/Hw$.

Note that the ratio R'/w is just the mass-weighted average velocity of the precipitation, <V>:

$$\langle V \rangle \equiv \frac{\int_0^\infty m(r)\, V(r)\, N(r)\, dr}{\int_0^\infty m(r)\, N(r)\, dr} = \frac{R'}{w} \qquad \text{(H-10)}$$

where m(r) is the mass of a drop of radius r. This is the relevant effective transport velocity for the debris-laden rain. From Eq. (H-3) we find

$$w\left(gM^{-3}\right) = \frac{4\pi N_0 \rho_w}{3} \int_0^\infty r^3 e^{-\alpha r} dr = \frac{8\pi N_0 \rho_w}{\alpha^4} = 8.9 \times 10^{-2} R^{0.84} \quad , \qquad \text{(H-11)}$$

which along with Eq. (H-10) leads to

$$\langle V \rangle \left(ms^{-1}\right) = 3.1 R^{0.16} \text{ R in mm h}^{-1} \quad . \qquad \text{(H-12)}$$

This expression for the effective velocity of precipitation is consistent with data reported by Fullerton and Wilson.[49] {However, it disagrees considerably--by about 60% for R = 1 mm h^{-1}--with a result obtained by Kessler,[50] who assumed, somewhat arbitrarily, that the velocity of precipitation is nearly the same as the terminal velocity of the median volume diameter particle [the drop with diameter D_o such that half the water is on drops with $D \lesssim D_o$, so that $w/2 = \int_o^{D_o} m(D)\, N(D)\, dD$].}

With Eq. (H-12) we thus arrive at the following estimate of the scavenging rate under conditions of very rapid drop coagulation:

$$\Lambda_T \left(s^{-1}\right) \approx \frac{3R^{0.16}}{H} \quad H \text{ in m} \quad . \qquad \text{(H-13)}$$

For example, if H = 1 km and R = 1 mm h^{-1}, then $\Lambda_T \approx 3 \times 10^{-3}$ s^{-1}, compared to $\Lambda = 3.5 \times 10^{-4}$ s^{-1} from Eq. (H-9); i.e., Λ_T is about one order of magnitude larger than Λ.

It may seem puzzling to note from Eqs. (H-9) and (H-13) that Λ exceeds Λ_T if $R^{0.6} \gtrsim 10^4/H$. This points up the fact that for sufficiently large rain rates, the accretion of contaminated cloud water by rain occurs in a time period which is smaller than the time needed for fallout of the contaminated rain from the debris-containing cloud volume. For such rain rates, Eq. (H-13) provides a better (and smaller) estimate for the scavenging coefficient. As an example, if H = 1 km, then Eq. (H-9) becomes unrealistically large for $R \gtrsim 50$ mm h^{-1}.

APPENDIX I
RAIN-INTENSITY VERTICAL WEIGHTING FUNCTION

The altitude dependence of precipitation intensity, designated by $\alpha(Z)$ where Z is altitude, was derived from O'Reilly,[51] who offers a family of curves for different ground-level intensities. When these are normalized to the surface intensity the various curves group together, so it is reasonable to select a single function to represent

$$\alpha(Z) = \frac{R(Z)}{R(O)} \quad ,$$

where R(Z) = rain intensity at altitude Z. This function is tabulated in Table I-1. It shows a maximum at cloud base and decreases to zero at ~9 km. The intricacies of intensity variation in the subcloud layer, and the cloud-to-cloud variations with altitude are not addressed here.

TABLE I-1

NORMALIZED VERTICAL-INTENSITY WEIGHTING

FUNCTION $\alpha(Z)$ versus Z

Altitude Z (km)	Z
0	1.0
0.5	1.0
1.0	0.97
1.5	0.90
2.5	0.67
3.5	0.39
4.5	0.29
5.5	0.16
6.5	0.09
7.5	0.03
8.5	0.01
9.5	0

REFERENCES

1. J. B. Knox and C. R. Molenkamp, "Investigations of the Dose to Man from the Wet Deposition of Nuclear Aerosols," Lawrence Livermore Laboratory report UCRL-76109 (1974).

2. S. Baum, P. W. Wong, P. J. Dolan, "NUCHOM: A Model of Rainout from Nuclear Clouds," Standard Research Institute report DNA 3389F (1974).

3 J. B. Knox, C. R. Molenkamp, T. F. Harvey, K. R. Peterson, J. F. Barbieri, R. Lange, and M. M. Fulk, "Progress in Rainout Research at Lawrence Livermore Laboratory," Lawrence Livermore Laboratory report UCRL-51625-75 (1975).

4. C. W. Watson and S. Barr, "Monte Carlo Simulation of the Turbulent Transport of Airborne Contaminants," Los Alamos Scientific Laboratory report LA-6103 (January 1976).

5. E. D. Cashwell, J. R. Neergaard, W. M. Taylor, and G. D. Turner, "MCN: A Neutron Monte Carlo Code," Los Alamos Scientific Laboratory report LA-4751 (January 1972).

6. R. C. Woronicz, "Western European Cyclone Climatology for Nuclear Application," USAF, ETAC project No. 6893 (1972).

7. M. G. Weiner and L. H. Wegner, personal communication, 1972.

8. C. W. Watson, Los Alamos Scientific Laboratory internal document, March 1975.

9. One- and six-hour data from USAF Environmental Technical Applications Center (ETAC), personal communication, March 1973.

10. Twenty-four hour data from N. Sissenwine, Air Force Cambridge Research Laboratories, Bedford, Massachusetts, personal communication, November 1972.

11. R. J. Boucher and R. J. Newcomb, "Synoptic Interpretation of Some TIROS Vortex Patterns; A Preliminary Cyclone Model," J. Appl. Met. 1, 127-136 (1962).

12. R. E. Nagle and S. M. Serebreny, "Radar Precipitation Echo and Satellite Cloud Observations of a Maritime Cyclone," J. Appl. Met. 1, 279-286 (1962).

13. P. M. Austin and R. A. Houze, "Analysis of the Structure of Precipitation Patterns in New England," J. Appl. Met. 11, 926-935 (1972).

14. L. J. Battan, Radar Meteorology (Univ. Chicago Press, Chicago, IL, 1973).

15. J. S. Marshall and C. D. Holtz, "Pattern Analysis of One Summer's Multilevel Maps of Montreal Rain," Mon. Weather Rev. 98, 335-345 (1970).

16. I. I. Zawadski, "Statistical Properties of Precipitation Patterns," J. Appl. Met. 12, 459-472 (1973).

17. B. Ackerman, "The Nature of the Meteorological Fluctuations in Clouds," J. Appl. Met. 6, 61-71 (1967).

18. G. B. Foote, "Variance Spectrum Analysis of Doppler Radar Observations in Continuous Precipitation," J. Appl. Met. 1, 459-463 (1968).

19. F. A. Huff and W. L. Shipp, "Spatial Correlations of Storm, Monthly and Seasonal Precipitation," J. Appl. Met. 8, 542-550 (1969).

20. P. M. Hamilton, "Vertical Profiles of Total Precipitation in Shower Situations," Q.J.R.M.S. 346-362 (1967).

21. S. Petterssen, Weather Analysis and Forecasting, Vol II (McGraw-Hill, New York, 1956).

22. C. M. Fullerton and S. K. Wilson, "Analysis of High Intensity Rainfall Data," Water Resources Research Center, University of Hawaii (1976).

23. T. G. Konrad et al., "Radar Derived Spatial Statistics of Summer Rain," Vol. 2, Data Reduction and Analysis, Applied Phys. Lab, Johns-Hopkins Univ. (1975).

24. D. M. A. Jones and A. L. Sims, "Climatology of Instantaneous Precipitation Rates," Illinois State Water Survey Final Report under Contract No. F19628-69-C-0070 with AFCAL, USAF, Bedford, MA, 01730 (1971).

25. J. B. Knox, T. V. Crawford, and W. K. Crandall, "Potential Exposures from Low-Yield Free Air Bursts," Lawrence Livermore Laboratory report UCRL-51164 (1971).

26. D. H. Joseph, National Center for Atmospheric Research, personal communication, October 1972.

27. R. L. Jenne, "The NMC Octagonal Grid," National Center for Atmospheric Research informal report, Boulder, CO (1970).

28. K. Fong and L. Rathmann, Los Alamos Scientific Laboratory, unpublished work (1973).

29. C. J. Everett and E. D. Cashwell, "A Monte Carlo Sampler," Los Alamos Scientific Laboratory report LA-5061-MS (October 1972).

30. L. L. Carter and E. D. Cashwell, "Particle-Transport Simulation with the Monte Carlo Method," ERDA critical review series, National Technical Information Service report TID-26607, Springfield, VA (1975).

31. C. Hastings, Jr., Approximations for Digital Computers (Princeton Univ. Press, Princeton, NJ, 1955).

32. A. L. Williams, "An Analysis of In-Cloud Scavenging Efficiencies," Lawrence Livermore Laboratory report UCRL-75897 (1974).

33. K. C. Young, "The Role of Contact Nucleation in Ice Phase Initiation in Clouds," J. Atmos. Sci. 31, 768-776 (1974).

34. W. V. Crandall, C. R. Molenkamp, A. L. Williams, M. M. Fulk, R. Lange, and J. B. Knox, "An Investigation of Scavenging of Radioactivity from Nuclear Debris Clouds: Research in Progress," Lawrence Livermore Laboratory report UCRL-75896 (1973).

35. A. N. Dingle and Y. Lee, "An Analysis of In-Cloud Scavenging," J. Appl. Meteor. 12, 1295-1302 (1973).

36. W. G. N. Slinn and J. M. Hales, "A Reevaluation of the Role of Thermophoresis as a Mechanism of In- and Below-Cloud Scavenging," J. Atmos. Sci. 28, 1465-1471 (1971).

37. A. N. Dingle, "Rain Scavenging Studies," Progress Report No. 11, Univ. Michigan Report COO-1407-58 (1975).

38. M. Kerker and V. Hampl, "Scavenging of Aerosol Particles by a Falling Water Drop and Calculation of Washout Coefficients," J. Atmos. Sci. 31, 1368-1376 (1974).

39. V. Hampl, M. Kerker, D. D. Cooke, and E. Matijevic, "Scavenging of Aerosol Particles by a Falling Water Droplet," J. Atmos. Sci. 28, 1211-1221 (1971).

40. G. B. Foote and J. C. Fankhauser, "Airflow and Moisture Budget Beneath a Northeast Colorado Hailstorm," J. Appl. Meteor. 12, 1330-1353 (1973).

41. A. B. Long, "Solutions to the Droplet Collection Equation for Polynomial Kernels," J. Atmos. Sci. 31, 1040-1052 (1974).

42. U. Shafrir and T. Gal-Chen, "A Numerical Study of Collision Efficiencies and Coalescence Parameters for Droplet Pairs with Radii up to 300 Microns," J. Atmos. Sci. 28, 741-751 (1971).

43. J. D. Klett and M. H. Davis, "Theoretical Collision Efficiencies of Cloud Droplets at Small Reynolds Numbers," J. Atmos. Sci. 30, 107-117 (1973).

44. R. Gunn and G. D. Kinzer, "The Terminal Velocity of Fall for Water Drops in Stagnant Air," J. Meteor. 6, 243-248 (1949).

45. K. V. Beard and H. R. Pruppacher, "A Determination of the Terminal Velocity and Drag of Small Water Drops by Means of a Wind Tunnel," J. Atmos. Sci. 26, 1066-1072 (1969).

46. J. S. Marshall and W. McK. Palmer, "The Distribution of Raindrops with Size," J. Meteor. 5, 165-166 (1948).

47. A. Waldvogel, "The N_0 Jump of Raindrop Spectra," J. Atmos. Sci. 31, 1067-1078 (1974).

48. A. C. Chamberlain, "Aspects of Travel and Deposition of Aerosol and Vapor Clouds," British Report AERE-HP/R-1261 (1953).

49. C. M. Fullerton and S. K. Wilson, "Some Characteristics of Hawaiian High-Intensity Rainfall." Univ. Hawaii tech. report UHMET 74-01, No. 78 (1974).

50. E. Kessler, "On the Distribution and Continuity of Water Substance in Atmospheric Circulations," Meteorological Monographs, 10 (1969).

51. P. J. O'Reilly, "Adverse Weather Models," USAF ETAC report No. 6467, USAF Environmental Applications Center, Navy Yard Annex, Wash., DC (1970).

☆ U.S. GOVERNMENT PRINTING OFFICE: 1977—777-089/130